



NAVAL POSTGRADUATE SCHOOL

MONTEREY, CALIFORNIA

DISSERTATION

**INTEGRATED RANGE-DOPPLER MAP AND EXTENDED
TARGET CLASSIFICATION WITH ADAPTIVE
WAVEFORM FOR COGNITIVE RADAR**

by

Jo-Yen Nieh

December 2014

Dissertation Supervisor

Ric Romero

Approved for public release; distribution is unlimited

THIS PAGE INTENTIONALLY LEFT BLANK

REPORT DOCUMENTATION PAGE			<i>Form Approved OMB No. 0704-0188</i>	
Public reporting burden for this collection of information is estimated to average 1 hour per response, including the time for reviewing instruction, searching existing data sources, gathering and maintaining the data needed, and completing and reviewing the collection of information. Send comments regarding this burden estimate or any other aspect of this collection of information, including suggestions for reducing this burden, to Washington headquarters Services, Directorate for Information Operations and Reports, 1215 Jefferson Davis Highway, Suite 1204, Arlington, VA 22202-4302, and to the Office of Management and Budget, Paperwork Reduction Project (0704-0188) Washington, DC 20503.				
1. AGENCY USE ONLY (Leave blank)		2. REPORT DATE December 2014	3. REPORT TYPE AND DATES COVERED Dissertation	
4. TITLE AND SUBTITLE INTEGRATED RANGE-DOPPLER MAP AND EXTENDED TARGET CLASSIFICATION WITH ADAPTIVE WAVEFORM FOR COGNITIVE RADAR			5. FUNDING NUMBERS	
6. AUTHOR(S) Jo-Yen Nieh				
7. PERFORMING ORGANIZATION NAME(S) AND ADDRESS(ES) Naval Postgraduate School Monterey, CA 93943-5000			8. PERFORMING ORGANIZATION REPORT NUMBER	
9. SPONSORING /MONITORING AGENCY NAME(S) AND ADDRESS(ES) N/A			10. SPONSORING/MONITORING AGENCY REPORT NUMBER	
11. SUPPLEMENTARY NOTES The views expressed in this dissertation are those of the author and do not reflect the official policy or position of the Department of Defense or the U.S. Government. IRB Protocol number ____N/A____.				
12a. DISTRIBUTION / AVAILABILITY STATEMENT Approved for public release; distribution is unlimited			12b. DISTRIBUTION CODE	
13. ABSTRACT (maximum 200 words) We set out to design an extended target classification scheme while determining the target's range-and-Doppler location with the use of adaptive waveform for a closed-loop cognitive radar platform. To that end, this work is divided into three objectives: 1) in support of determining range-Doppler locations, we investigate the ambiguity function of the matched waveform called eigenwaveform, 2) in support of target classification, we look at an adaptive waveform technique called probability-weighted eigenwaveform (PWE) and introduce two new waveforms, and 3) we design an integrated range-Doppler map and extended target classification scheme. In this work, we show that the fundamental properties of ambiguity function for extended targets are different when compared to classical waveforms for point targets. We improve on the adaptive waveform called maximum a posteriori PWE and introduce two new waveforms called match-filtered PWE and two-stage PWE. We propose an integrated range-Doppler map and identification scheme for multiple moving extended targets. Performance comparisons in terms of joint probability of identification and determining targets' range-Doppler locations with traditional wideband waveform and the three PWE-based waveforms are shown. It is shown that the three PWE-based waveforms perform better than the classical wideband waveform.				
14. SUBJECT TERMS waveform design, eigen waveform, ambiguity function, target identification, target detection, range Doppler map, range Doppler location			15. NUMBER OF PAGES 123	
			16. PRICE CODE	
17. SECURITY CLASSIFICATION OF REPORT Unclassified	18. SECURITY CLASSIFICATION OF THIS PAGE Unclassified	19. SECURITY CLASSIFICATION OF ABSTRACT Unclassified	20. LIMITATION OF ABSTRACT UU	

NSN 7540-01-280-5500

Standard Form 298 (Rev. 2-89)
Prescribed by ANSI Std. Z39-18

THIS PAGE INTENTIONALLY LEFT BLANK

Approved for public release; distribution is unlimited

**INTEGRATED RANGE-DOPPLER MAP AND EXTENDED TARGET
CLASSIFICATION WITH ADAPTIVE WAVEFORM FOR COGNITIVE RADAR**

Jo-Yen Nieh
Major, Taiwan Army
B.S., Chung Cheng Institute of Technology, Taoyuan, Taiwan, 2001
M.S., Naval Postgraduate School, Monterey, 2006

Submitted in partial fulfillment of the
requirements for the degree of

DOCTOR OF PHILOSOPHY IN ELECTRICAL ENGINEERING

from the

**NAVAL POSTGRADUATE SCHOOL
December 2014**

Author: Jo-Yen Nieh

Approved by:	Tri Ha Professor of Electrical and Computer Engineering Dissertation Committee Chair	Roberto Cristi Professor of Electrical and Computer Engineering
	Weilian Su Associate Professor of Electrical and Computer Engineering	Kyle Y Lin Associate Professor of Operation Research
	Ric Romero Assistant Professor of Electrical and Computer Engineering Dissertation Committee Advisor	

Approved by: R. C. Robertson, Chair, Dept. of Electrical and Computer Engineering

Approved by: Douglas Moses, Vice Provost for Academic Affairs

THIS PAGE INTENTIONALLY LEFT BLANK

ABSTRACT

We set out to design an extended target classification scheme while determining the target's range-and-Doppler location with the use of adaptive waveform for a closed-loop cognitive radar platform. To that end, this work is divided into three objectives: 1) in support of determining range-Doppler locations, we investigate the ambiguity function of the matched waveform called eigenwaveform, 2) in support of target classification, we look at an adaptive waveform technique called probability-weighted eigenwaveform (PWE) and introduce two new waveforms, and 3) we design an integrated range-Doppler map and extended target classification scheme.

In this work, we show that the fundamental properties of ambiguity function for extended targets are different when compared to classical waveforms for point targets. We improve on the adaptive waveform called maximum a posteriori PWE and introduce two new waveforms called match-filtered PWE and two-stage PWE. We propose an integrated range-Doppler map and identification scheme for multiple moving extended targets. Performance comparisons in terms of joint probability of identification and determining targets' range-Doppler locations with traditional wideband waveform and the three PWE-based waveforms are shown. It is shown that the three PWE-based waveforms perform better than the classical wideband waveform.

THIS PAGE INTENTIONALLY LEFT BLANK

TABLE OF CONTENTS

I.	INTRODUCTION.....	1
II.	RANGE RESOLUTION FOR EXTENDED TARGET ILLUMINATED BY AN EIGENWAVEFORM	5
A.	RANGE RESOLUTION	5
B.	REVIEW OF EIGENWAVEFORM.....	7
III.	PROPERTIES OF THE AMBIGUITY FUNCTION FOR EXTENDED TARGETS AND THE EIGENWAVEFORM.....	11
A.	DISCRETE OR VECTOR SIGNAL MODELING	12
B.	PROPERTIES OF THE AMBIGUITY FUNCTION.....	14
IV.	AMBIGUITY FUNCTIONS OF ONE-PULSE WAVEFORMS.....	19
A.	EIGENWAVEFORM, WIDEBAND WAVEFORM, AND RECTANGULAR WAVEFORM.....	19
B.	EIGENWAVEFORM VS. WIDEBAND AMBIGUITY FUNCTIONS....	22
C.	RECTANGULAR WAVEFORM AF FOR OSCILLATORY TARGET (TARGET 1)	24
D.	RECTANGULAR WAVEFORM AF FOR NON-OSCILLATORY TARGET (TARGET 2)	26
E.	PRACTICAL TARGET (BOEING 737–500 RANGE PROFILE)	28
F.	AF ZERO-DELAY AND ZERO DOPPLER CUTS FOR EXTENDED TARGETS	31
V.	COHERENT MULTIPLE-PULSE TRANSMISSION	33
A.	ZERO-DOPPLER CUT	37
B.	ZERO-DELAY CUT	40
C.	RANGE AND DOPPLER RESOLUTION TRADE-OFF	43
VI.	DETECTION PROBABILITY AND RANGE-DOPPLER MAP	45
A.	DETECTION PROBABILITY OF BASIC ONE-PULSE WAVEFORMS.....	45
B.	DETECTION PROBABILITY OF COHERENT MULTIPLE-PULSE TRANSMISSION AND RANGE DOPPLER MAP APPLICATION.....	49
VII.	PROBABILITY WEIGHTED EIGENWAVEFORMS (PWE) FOR TARGET RECOGNITION	53
A.	ADAPTIVE WAVEFORMS, LIKELIHOOD UPDATES, AND COGNITIVE RADAR PLATFORM INTRODUCTION.....	53
1.	MAP-PWE	53
2.	MF-PWE.....	59
B.	TWO-STAGE PWE FOR LOW SNR	62
VIII.	MULTIPLE TARGET IDENTIFICATION AND RANGE-DOPPLER LOCATION.....	69

A.	TWO TARGETS OF SAME TYPE SCENARIO.....	69
B.	UNKNOWN NUMBER OF TARGETS (OF THE SAME TYPE)	76
C.	TWO TARGETS OF DIFFERENT TYPES (SCENARIO)	81
D.	UNKNOWN NUMBER OF TARGETS AND DIFFERENT TYPES OF TARGETS.....	85
IX.	CONCLUSION	91
	APPENDIX.....	93
	LIST OF REFERENCES	99
	INITIAL DISTRIBUTION LIST	103

LIST OF FIGURES

Figure 1.	Target range separation setting: (a) target range separation for point targets, and (b) target range separation for extended targets.	5
Figure 2.	Top panel: Target magnitudes in frequency response. Middle panel: Frequency response magnitudes of transmit signal. Bottom panel: Frequency response magnitudes of return signal.	9
Figure 3.	One-pulse transmit waveform for extended target: (a) wideband waveform, (b) rectangular waveform, and (c) eigenwaveform.	19
Figure 4.	Top panel: target frequency response, middle panel: eigenwaveform frequency response, and bottom panel: return signal frequency response.	21
Figure 5.	Example of a range profile of a Boeing 737-500 used as Target 3. The radar range profile is at the bottom. From [33].	22
Figure 6.	Ambiguity function and AF contour plots of Target 1 illuminated by wideband waveform vs eigenwaveform. Top panel: 3-D view, and bottom panel: contour plots.	23
Figure 7.	Ambiguity function analysis of rectangular waveform with Target 1 ($ToTR = 0.64$): (a) ambiguity function, (b) AF contour plot, (c) Target 1 frequency response (magnitude), (d) transmit signal frequency response (magnitude), (e) return signal frequency response (magnitude).	25
Figure 8.	Ambiguity function analysis of rectangular waveform with Target 1 ($ToTR = 0.09$): (a) ambiguity function, (b) AF contour plot, (c) Target 1 frequency response (magnitude), (d) transmit signal frequency response (magnitude), (e) return signal frequency response (magnitude).	26
Figure 9.	Ambiguity function analysis of rectangular transmit waveform with Target 2 (AF peak value = 232.38): (a) ambiguity function, (b) AF contour plot, (c) Target 2 frequency response (magnitude), (d) transmit signal frequency response (magnitude), and (e) return signal frequency response (magnitude).	27
Figure 10.	Ambiguity function analysis of eigenwaveform with Target 2 (AF peak value = 377.45): (a) ambiguity function, (b) AF contour plot, (c) Target 2 frequency response (magnitude), (d) transmit signal frequency response (magnitude), and (e) return signal frequency response (magnitude).	28
Figure 11.	Ambiguity function analysis of eigenwaveform with Boeing 737-500: (a) ambiguity function, (b) AF contour plot, (c) Boeing 737-500 frequency response (magnitude), (d) transmit signal frequency response (magnitude), and (e) return signal frequency response (magnitude).	29
Figure 12.	Ambiguity function analysis of wideband waveform with Boeing 737-500: (a) ambiguity function, (b) AF contour plot, (c) Boeing 737-500 frequency response (magnitude), (d) transmit signal frequency response (magnitude), and (e) return signal frequency response (magnitude).	30
Figure 13.	Multiple-pulse transmission for extended target setting: (a) wideband waveform, (b) rectangular waveform, and (c) eigenwaveform.	35

Figure 14.	Target 1 ambiguity function contour plots comparison ($L = 3$, $T_R = 4T$): (a) wideband waveform, (b) rectangular waveform, and (c) eigenwaveform.....	36
Figure 15.	Target 2 ambiguity function contour plots comparison ($L = 3$, $T_R = 4T$): (a) wideband waveform, (b) rectangular waveform, and (c) eigenwaveform.....	36
Figure 16.	Zero-Doppler cut of Target 1 AF with various waveforms. Upper panel: wideband waveform ($L = 3$, high PRF), middle panel: rectangular waveform ($L = 3$, $T_{oTR}=0.64$, high PRF), and lower panel: eigenwaveform ($L = 3$, high PRF).	37
Figure 17.	Zero-Doppler cut of Target 2 AF with normalized eigenwaveforms and various PRFs. Upper panel: ($L = 3$, high PRF), middle panel: ($L = 3$, medium PRF), and lower panel: ($L = 3$, low PRF).	39
Figure 18.	Zero-Doppler cut of Target 1 AF with un-normalized eigenwaveforms and various L . Upper panel: ($L = 1$, high PRF), middle panel: ($L = 3$, high PRF), and lower panel: ($L = 5$, high PRF).	40
Figure 19.	Zero-delay cut comparison with single, three, and five retransmissions with low PRF using the eigenwaveform.	42
Figure 20.	Zero-delay cut comparison with single, three, and five retransmissions with high PRF using the eigenwaveform.	42
Figure 21.	PRF and pulses number comparison with eigenwaveform: (a) zero-Doppler cut ($L = 30$, high PRF), (b) zero-delay cut ($L = 30$, high PRF), (c) zero-Doppler cut ($L = 3$, low PRF), and (d) zero-delay cut ($L = 3$, low PRF).	44
Figure 22.	Target 1 detection probability comparison of wideband waveform, rectangular waveform ($T_{oTR} = 0.64$) and eigenwaveform ($TNR = 0dB$).	48
Figure 23.	Target 2 detection probability comparison of wideband waveform, rectangular waveform ($T_{oTR} = 0.64$) and eigenwaveform ($TNR = 0dB$).	48
Figure 24.	Performance comparison: wideband waveform, rectangular waveform and eigenwaveform with various multiple-pulses transmission ($L = 3, 5, 10$).	51
Figure 25.	Target 1 3-D view RDM comparison for $SNR = (0 \text{ dB}, 3 \text{ dB}, 10 \text{ dB})$, and $TNR = 0 \text{ dB}$. The target is located at range (delay) = 560 with Doppler shift of $f_d = 0.0968$. Left panels: wideband waveform, middle panels: rectangular waveform, and right panels: eigenwaveform.	51
Figure 26.	Target 1 RDM comparison for $SNR = (0 \text{ dB}, 3 \text{ dB}, 10 \text{ dB})$, and $TNR = 0 \text{ dB}$. The targets are located at range (delay) = 450 with Doppler shift of $f_{d1} = 0.1613$ and range (delay) = 750 with Doppler shift of $f_{d2} = 0.1290$. Left panels: wideband waveform, middle panels: rectangular waveform, and right panels: eigenwaveform.	52
Figure 27.	Mean of target probability updates versus transmission energy under noise only scenario assuming unity noise energy. (a)MAP-PWE. (b)MF-PWE.	58
Figure 28.	Performance comparison: MAP-PWE and MF-PWE with multiple transmissions assuming unity noise energy.	61

Figure 29.	Average or mean number of transmit (probability threshold = 0.95) comparison assuming unity noise energy.	62
Figure 30.	Operational flow diagram for the TS-PWE scheme with a closed-loop radar.	65
Figure 31.	Mean number of illuminations as a function of (received) transmit energy for various adaptive waveforms assuming unity noise energy.	66
Figure 32.	TS-PWE vs MF-PWE identification performance comparison as parameterized by the number of updates (or number of transmissions) assuming unity noise energy.	66
Figure 33.	Range Doppler map of two targets of the same type (some noise added).	71
Figure 34.	Four candidate RDMs for four possible target types (where two targets of the same type are present) with PWE after one transmission (no update).	71
Figure 35.	Four candidate RDMs for four possible target types (where two targets of the same type are present) with PWE after three transmissions (two updates).	72
Figure 36.	Four candidate RDMs for four possible target types (where two targets of the same type are present) with PWE after six transmissions (five updates).	72
Figure 37.	Probability of correctly determining target type, probability of correctly determining the range-Doppler location, and the overall performance of correctly determining target type and range-Doppler location using MF-PWE with two targets of same type.	74
Figure 38.	Identification probability comparison of six updates and ten updates of various PWE schemes assuming unity noise energy for two targets of same type scenario.	75
Figure 39.	Probability comparison of correctly determining targets type and range-Doppler location of no update, one update, two updates, and five updates vs MF-PWE and TS-PWE schemes assuming unity noise energy with two targets of same type.	75
Figure 40.	Probability of locating correct range and Doppler given target type identification and probability of false alarm ($P_{FA} = 0.1$) assuming unity noise energy where type 1 is the correct hypothesis.	79
Figure 41.	Probability of locating correct range and Doppler given correct/incorrect target type identification and various probability of false alarm assuming unity noise energy.	79
Figure 42.	Joint probability of locating correct ranges, Doppler and target types vs various MF-PWE updates numbers given probability of false alarm assuming unity noise energy.	81
Figure 43.	Flow diagram/procedural steps for two different target types (scenario).	83
Figure 44.	No update: RDMs of two targets from different types after M matched filters ($M = 4$).	84
Figure 45.	Six updates: RDMs of two targets from different types after M matched filters ($M = 4$).	84
Figure 46.	Overall probability of identification and location for two targets of different types assuming unity noise energy.	85

Figure 47.	Overall probability of identification and location for multiple targets of unknown types assuming unity noise energy ($\psi = 10$ percent and $P_{FA} = 0.1$).	89
Figure 48.	Flow diagram/procedural steps of multiple targets identification and range-Doppler location algorithm.....	90

LIST OF ACRONYMS AND ABBREVIATIONS

AF	ambiguity function
AWGN	additive white Gaussian noise
CR	cognitive radar
ESD	energy spectral density
FFT	fast-Fourier transform
MAP-PWE	maximum a posteriori probability weighted eigenwaveform
MF-PWE	match-filtered probability weighted eigenwaveform
MHT	multiple hypothesis testing
PFA	probability of false alarms
PRF	pulse repetition frequency
PRI	pulse repetition interval
PWE	probability weighted eigenwaveform
RDM	range-Doppler map
SNR	signal-to-noise energy ratio
TNR	target-to-noise energy ratio
ToT	time-on-target
ToTR	time-on-target ratio
TS-PWE	two-stage probability weighted eigenwaveform

THIS PAGE INTENTIONALLY LEFT BLANK

EXECUTIVE SUMMARY

In this dissertation, we apply the optimum waveform design for a deterministic extended target (also known as eigenwaveform [1]) to ambiguity function analysis. Interestingly, the fundamental properties (peak and volume) of ambiguity function for a known extended target are different when compared to ambiguity functions of classical waveforms for a point target [2]. Extended target responses vary greatly from target to target, from one aspect angle to another, etc. For the purposes of illustration in this work, we form two distinct target types (oscillatory and less or non-oscillatory) and analyze the ambiguity function of these two types with the use of eigenwaveforms. Ambiguity function depends also if the transmit waveform is one pulse as in continuous wave (CW) or multiple pulses as in pulse-Doppler radar systems. For multiple pulse eigenwaveforms, increasing pulse repetition frequency results in increasing Doppler sinc-lobes separation but increasing pulse repetition frequency results in the reduction of the unambiguous range just as in traditional pulse-Doppler systems. However, due to the increased time interval of the return (with the use of eigenwaveform) Doppler resolution improves at the expense of range resolution.

Based on optimum waveform design for a deterministic extended target, we investigate and expand the notion of the adaptive waveform called probability weighted eigenwaveform (PWE) that is used for target recognition with a cognitive radar platform [3]. PWE is designed and implemented for non-moving target identification problem in a cognitive fashion where the waveform weights of eigenwaveforms corresponding to an ensemble of targets to form the transmit waveform is updated via previous return (received measurement) and likelihood calculations under the constraint of transmit energy or number of transmissions. We propose two new PWE-based adaptive waveforms in addition to an existing one. The three adaptive waveforms are: maximum a posteriori PWE (MAP-PWE), match-filtered PWE (MF-PWE) and two-stage PWE (TS-PWE), which adaptively uses likelihood information from previous and present stage to form next waveform in a specific way. It is shown that the three PWE-based

waveforms perform better than the classical wideband waveform. It is also shown that MF-PWE and TS-PWE seem to perform better than MAP-PWE.

Our ultimate goal in this dissertation is to design an integrated algorithm that addresses the combined problem of multiple moving target identification while determining accurate range and Doppler locations. Combining range-Doppler map (RDM) technique with the PWE-based adaptive waveform techniques, we propose an integrated range-Doppler map and target identification scheme for multiple moving extended targets. The overall probability of correctly locating an extended target in range-and-Doppler and identifying target type is clearly a function of received signal-to-noise ratio, number of transmissions L , PWE schemes and the target responses themselves via maximum target eigenvalues. In practice, a priori assumption may come from other sensors or some intelligence information. At the end of this work, various performance comparisons in terms of overall probability of identification and probability of correctly determining range-Doppler locations for the three PWE-based waveforms are evaluated against a classical wideband pulse waveform. All the waveforms are used in a closed-loop radar system. It is noted the MAP-PWE, MF-PWE, and TS-PWE perform better than the wideband waveform.

LIST OF REFERENCES

- [1] M. R. Bell, "Information theory and radar waveform design," *IEEE Trans. Information Theory.*, vol. 39, no. 5, pp. 1578–1597, Sep. 1993.
- [2] N. Levanon and E. Mozeson, *Radar Signals*. Hoboken, NJ: John Wiley and Sons, 2004.
- [3] R. A. Romero, and N. A. Goodman, "Information-theoretic matched waveform in signal dependent interference," *IEEE Radar Conference.*, Rome, Italy, pp. 1–6, May 2008.

ACKNOWLEDGMENTS

I would like to sincerely thank my wife, Nicole. It was her enduring support and love that has sustained me through this challenging dissertation process.

I would also like to express my sincere gratitude to my advisor, Professor Ric Romero. It was the foundation you helped me build that allowed me to weather the storm that is the PhD program, and without your mentorship, I would simply be lost in a virtual forest of my own design.

To my committee members: Professor Tri Ha, Professor Roberto Cristi, Professor Weilian Su, and Professor Kyle Lin, your insights and guidance for this dissertation were invaluable, and for that I am very grateful.

THIS PAGE INTENTIONALLY LEFT BLANK

I. INTRODUCTION

There are three main related objectives in this work. The first is to investigate the application of matched waveform design (also called eigenwaveform) [1] to ambiguity function. In other words, we are interested in the target range and Doppler implications of the eigenwaveform. The second objective is to extend the adaptive waveform called the probability weighted eigenwaveform (PWE) first proposed in [2] and investigate its classification performance. As such, we are also interested in identification of extended targets. And finally, the third objective (which utilizes the results of the first two) is to design an integrated scheme for the combined problem of range-Doppler location/detection with extended target type identification with the use of a closed-loop radar system employing adaptive waveforms. Such a system is an example of a cognitive radar (CR).

In this work, we utilize adaptive waveforms based on eigenwaveform which is also known as SNR-based illumination waveform design [1]. Thus, there is a need to evaluate ambiguity functions of radar systems employing eigenwaveforms and their properties. We investigated eigenwaveform-based ambiguity functions with the use of three types of targets (oscillatory, non-oscillatory, and one based on an actual Boeing aircraft). We found that the AF properties (peak and volume) for eigenwaveforms to be much larger than that of traditional waveforms for point targets. Unlike traditional transmit waveforms whose responses totally dictate the shape of the ambiguity function, both matched illumination waveform and extended target response contribute to the shape of the ambiguity function. In other words, range and Doppler resolutions are not just functions of the transmit waveform but of the target response itself, which makes for interesting ambiguity functions. Various range-Doppler trade-offs are made with the use of pulsed eigenwaveforms.

For a traditional radar system where targets of interest are very far in range, a good and common model is to assume that the targets are point targets. In additive white Gaussian channel, the received waveform is therefore the scaled transmit waveform plus noise. The probability of detection is then a function of the received waveform energy

regardless of its shape [2]. Moreover, the ambiguity function is dictated by the shape of the transmit waveform. Waveform designs in consideration of the ambiguity function for point target model has a rich literature [3]–[5] and these waveforms have well known properties in terms of range resolution, Doppler resolution, and probability of detection. Our interest however is extended targets, i.e., targets that have certain impulse responses (i.e., have finite time support) and therefore the returns do not just depend on the transmit waveform but rather depend on both the transmit signal and the target’s response via their convolution. Given constraint in energy, it is shown in [6] that the eigenwaveform is the waveform that maximizes the signal-to-noise ratio in additive white Gaussian or colored noise. In signal-dependent interference however, the energy spectral density (ESD) of the optimal waveform is derived in [1]. In [1] and [6], the emphasis is to derive optimum waveforms for extended targets while in [7]–[9], the emphasis is to apply the adaptive waveforms in a target recognition or classification using cognitive radar (CR) [10]. The traditional targets in radar field are assumed to be point targets and have a rich literature of waveform design and detection theory in [11]–[14]. However, for an extended target of our interests, the range resolution, ambiguity function and probability of detection are clearly affected by the target’s impulse response. We investigate and evaluate the range resolution, ambiguity function, and probability of detection of radar that employs eigenwaveform.

Moreover, we evaluate the target identification performance of PWE-based waveforms in target identification problems. To this end, we propose improvements to the maximum a posteriori probability weighted eigenwaveform (MAP-PWE) adaptive waveform design used in target recognition with a cognitive radar platform. The two improvements are called match-filtered PWE (MF-PWE) and two-stage PWE (TS-PWE).

Various target detection and classification schemes are reported in many articles and a few are referenced here for the interested reader [15]–[21]. But our research is to investigate the properties of ambiguity function with extended targets and develop an integrated detection and classification schemes in a cognitive manner [1], [2], and [7]. Some other works use likelihood or correlation characteristic [22]–[26]. However, our method is to look at the detection probability improvement with PWE-based

transmissions. As had been shown before [1], [7], [8], and [18], the detection and classification performance of the adaptive waveforms are better than just employing a traditional wideband pulse waveform.

Recall that our ultimate goal in this dissertation is to design an integrated algorithm that addresses the combined problem of multiple moving target identification while determining accurate range and Doppler locations. Combining range-Doppler map (RDM) technique with the PWE-based adaptive waveform techniques, we propose an integrated range-Doppler location and target identification scheme for multiple moving extended targets. Various performance comparisons in terms of overall probability of identification and probability of correctly determining range-Doppler locations for the three PWE-based waveforms are evaluated against a classical wideband pulse waveform. All the waveforms are used in a closed-loop radar system. It is noted the MAP-PWE, MF-PWE, and TS-PWE perform better than the wideband waveform.

THIS PAGE INTENTIONALLY LEFT BLANK

II. RANGE RESOLUTION FOR EXTENDED TARGET ILLUMINATED BY AN EIGENWAVEFORM

For a point target illuminated by a basic pulse (one that is not compressed), the range resolution is easily derived. Since our target of interest is extended (one that has finite extent) then the range resolution provided by a basic pulse including the eigenwaveform has to be analyzed.

A. RANGE RESOLUTION

For point targets with the use of basic one-pulse waveforms, the minimum (range or time delay) separation of two targets is dictated by the length of transmit waveform. It is defined as the minimum time separation needed so that the return pulses do not overlap each other, i.e., it is the minimum corresponding range separation required such that two point targets can be resolved in range. This is easily illustrated in Fig1.a.

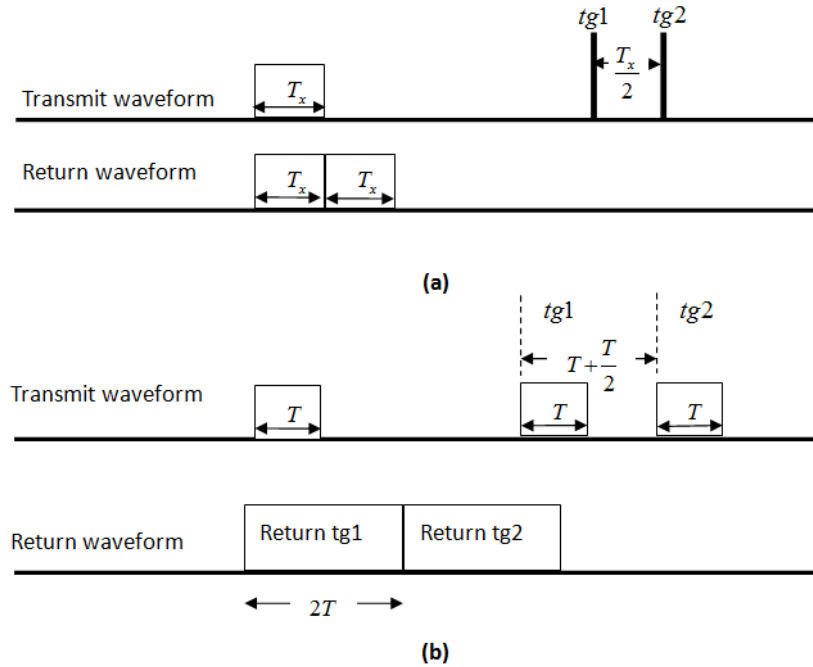


Figure 1. Target range separation setting: (a) target range separation for point targets, and (b) target range separation for extended targets.

Let T_x be the time duration of the transmit waveform. For the return waveforms not to overlap each other, two point targets need to be separated by $T_\rho = T_x / 2$ as shown in Fig. 1a. For basic pulsed waveform (not chirp or waveforms employing compression), the corresponding minimum range in which two target can be resolved is given by

$$R_\rho = cT_\rho = cT_x / 2, \quad (1)$$

where c is the speed of light (in free space). For basic one-pulsed waveforms, minimum range separation is usually referred to as range resolution.

In practice, range resolution can be improved by waveform design (using compression techniques) that can potentially increase the bandwidth (B) of the waveform. As such, range resolution is usually given by

$$R_\rho = cT_\rho = c / 2B. \quad (2)$$

Using minimum separation requirement, if the target has a response with duration T and that the eigenwaveform has same time duration ($T_x = T$), the falling edge of one target return has to be separated by $T / 2$ from the leading edge of another target return as illustrated in Fig. 1b. Thus, the minimum time needed in order for two extended targets to be resolved is given by $T_\rho = 1.5T$. Thus, the minimum range separation such that two targets can be resolved with the use of the eigenwaveform is given by

$$R_\rho = cT_\rho = 1.5cT. \quad (3)$$

For an extended target, both the eigenwaveform and the target response dictate the effective bandwidth of the return signal. As such a simple equation corresponding to (2) in terms of bandwidth does not easily apply. This is also the big difference between point target and extended target where waveform bandwidth is easily manipulated if a target is truly a point target. It is clear that for traditional waveforms (with large bandwidths) the resolution promised by (2) will not be realized if used for extended targets (especially if a target has a narrowband frequency response). This is because the frequency response of the return signal is the result of multiplication of the frequency responses of the transmit waveform and target response. Since a practical extended target

doesn't have an idealized flat frequency response like a point target, the frequency response of the return signal will surely be different from the frequency response of the transmit waveform. As such large bandwidths may be decreased.

For traditional waveforms with time duration T_x with the point target assumption, the minimum Doppler separation such that two targets of different speeds can be resolved is usually taken to be the reciprocal of the time duration, i.e., $\Delta f_d = 1/T_x$. If we use the same definition for an extended target with finite extent T , it follows that the Doppler resolution is $\Delta f_d = 1/(T_x + T)$. For an eigenwaveform, it is therefore $\Delta f_d = 1/2T$. In other words, while the eigenwaveform range resolution suffers due to the increased echo return, its Doppler resolution improves due to the length of the return, which accentuates the time-frequency resolution trade-off.

B. REVIEW OF EIGENWAVEFORM

In Bell's work [6], he derived the optimum transmit waveform matched to an extended target in continuous-time, which is later named eigenwaveform. For transmit signal $x(t)$ and target response $h(t)$, let $s(t)$ be the convolution of transmit signal and target response. Assume a matched filter in the receiver for signal detection. The output of matched filter is

$$\chi(\tau) = \int_{-\infty}^{\infty} s(t)s^*(t-\tau)e^{j2\pi f_d t} dt, \quad (4)$$

where τ is the time-delay (location) and f_d is the Doppler shift of a certain return. The $s(t)$ is the convolution result of transmit signal and target response.

For now, we may assume zero-Doppler since the energy in (4) is not affected by the Doppler shift. We may assume unit energy for the extended target in our signal models. Any other energy value (point target or otherwise) can be accommodated by scaling the energy of target response E_h . The eigenfunction $q_{\max}(t)$ corresponding to the maximum eigenvalue λ_{\max} is used as the transmit waveform, aka eigenwaveform [1].

Therefore

$$x(t) = q_{\max}(t), \quad (5)$$

and

$$\lambda_{\max} q_{\max}(t) = \int_{-\infty}^{\infty} q_{\max}(t) L(\rho - \tau) d\rho d\tau, \quad (6)$$

where ρ is a “dummy” variable and $L(\tau)$ is the autocorrelation function given by

$$L(\tau) = \int_{-\infty}^{\infty} |H(f)|^2 e^{j2\pi f\tau} df. \quad (7)$$

By substituting (6) and (7) into (4), E_s which is the energy of convolution of transmit signal and target response becomes

$$\begin{aligned} E_s &= \int_{-\infty}^{\infty} q_{\max}(\tau) \lambda_{\max} q_{\max}^*(\tau) d\tau \\ &= \lambda_{\max} \int_{-\infty}^{\infty} q_{\max}(\tau) q_{\max}^*(\tau) d\tau = \lambda_{\max} E_{q_{\max}}, \end{aligned} \quad (8)$$

where $E_{q_{\max}}$ is clearly the transmit energy of the eigenwaveform. That is, $E_x = E_{q_{\max}}$.

Compared to traditional point target whose E_s is merely E_x due to convolution with delta function regardless any target waveform, E_s for an eigenwaveform illuminating an extended target is amplified by λ_{\max} . Maximum eigenvalues from various target types are different, which means that the energy received is different from target to target.

To gain an insight into eigenwaveforms, we consider two complex-valued extended targets illustrated in Fig. 2, which are arbitrarily generated for the purposes of illustration. In the top panel, the magnitudes of the target frequency responses (normalized) are shown. Both targets are of unit energy. The magnitudes of the frequency responses of eigenwaveform are shown in the middle panel. The bottom panel shows the magnitudes of the frequency responses of the return signals.

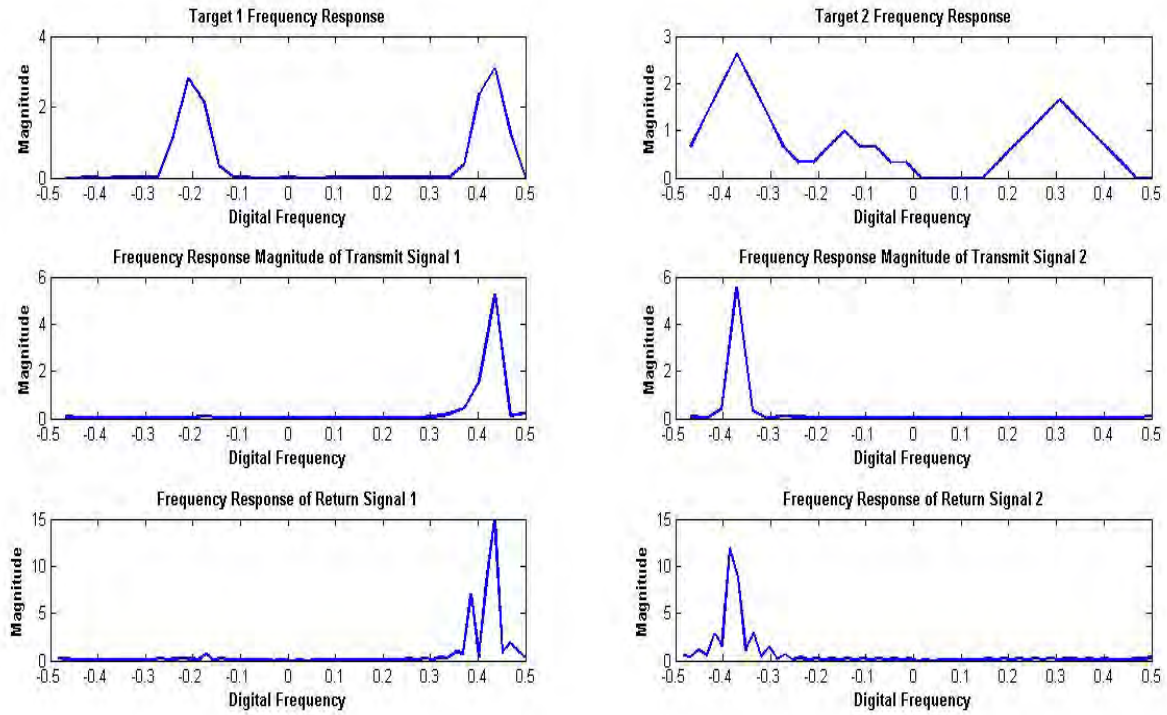


Figure 2. Top panel: Target magnitudes in frequency response. Middle panel: Frequency response magnitudes of transmit signal. Bottom panel: Frequency response magnitudes of return signal.

It is clear from Fig. 2 that, the eigenwaveform distributes most of its energy to the target's most resonant frequency band. We may think of this as the transmit waveform capturing the most of the energy of the target signal via the frequency domain.

THIS PAGE INTENTIONALLY LEFT BLANK

III. PROPERTIES OF THE AMBIGUITY FUNCTION FOR EXTENDED TARGETS AND THE EIGENWAVEFORM

In this section, we apply extended target and eigenwaveform method to the study of ambiguity function (AF). In classical ambiguity function studies, the received signal is assumed to be a replica of the transmit waveform. In other words, targets are assumed to be point targets. Again, AF analysis of various popular waveforms such as pulsed, phase-coded, and chirp waveforms assuming a point target is mature. Aside from the excellent texts cited above, we point out a few select ones such as [27]–[31]. Our interest however is extended targets and how various transmit waveforms affect ambiguity functions. More specifically, our interest is how both an extended target and its corresponding eigenwaveform design affect the ambiguity function.

In radar application, the ambiguity function features the output of the matched filter as a function of Doppler shift and time delay and is given by

$$|\chi(\tau, f_d)|^2 = \left| \int_{-\infty}^{\infty} x(t)x^*(t-\tau)e^{j2\pi f_d t} dt \right|^2 \quad (9)$$

where $x(t)$ is the transmit waveform, f_d is the Doppler shift, and τ is the time delay. Notice that this definition where squared-magnitude of the matched filter response is used is from [5]. Sometimes the magnitude of the matched filter response is used as in [4]. To avoid confusion, we will choose one and use the squared-magnitude definition of the ambiguity function. Again, it is clear from (9) that the received signal is the exact replica of the transmit waveform (assuming no noise or interference) where the target is assumed to be a point target. Unfortunately (9) does not work when the target has a finite extent. In the case of an extended target, the ambiguity function is not only a function of transmit waveform but is also a function of the target response. If the target response is given by $h(t)$ then the ambiguity function is given by

$$\begin{aligned}
& |\chi(\tau, f_d)|^2 \\
&= \left| \int_{-\infty}^{\infty} [x(t) * h(t)] \times [x(t - \tau) * h(t - \tau)]^* e^{j2\pi f_d t} dt \right|^2 \\
&= \left| \int_{-\infty}^{\infty} s(t) s^*(t - \tau) e^{j2\pi f_d t} dt \right|^2,
\end{aligned} \tag{10}$$

where $s(t)$ is the convolution return of transmit signal $x(t)$ and target response $h(t)$.

It is clear in (10) that for extended targets both transmit waveform and target responses dictate the ambiguity function. Our interest is to form the ambiguity function of the eigenwaveform given an extended target response and compare that function with AFs produced by traditional waveform such as wideband pulse and rectangular pulse waveforms.

A. DISCRETE OR VECTOR SIGNAL MODELING

Due to the advent of arbitrary waveform generators, modern waveforms are designed in discrete-time. Moreover, modern waveform design are usually simulated by modern computing that utilizes discrete-frequency techniques. Proper digital-to-analog conversion (DAC) easily converts the waveform into practical continuous-time waveform. Assuming proper sampling rate through Nyquist theory, we can utilize discrete-time and discrete-frequency models to form a discrete-time discrete-frequency version of the ambiguity function for extended target, which is given by

$$\begin{aligned}
|\chi[\tau_n; f_{dn}]|^2 &= \left| \sum_{i=0}^{N-1} s[i] \times s^*[i - \tau_n] \times W_N^{f_{dn} i} \right|^2 \\
&= \left| \sum_{i=0}^{N-1} (x[i] * h[i]) \times (x[i - \tau_n] * h[i - \tau_n])^* \times W_N^{f_{dn} i} \right|^2
\end{aligned} \tag{11}$$

where τ_n is the discrete delay and f_{dn} is the Doppler spread, x , h and s are the discrete transmit, target response, and return signals. N is the length of return vector s , $f_{dn} = 0, 1, \dots, N-1$, and

$$W_N^{f_{dn}} = e^{j2\pi \frac{f_{dn}}{N}}. \quad (12)$$

In general the length of f_{dn} may be desired to be different from N . That extension is easily incorporated into (11).

The peak of the ambiguity function is located at zero-delay and zero-Doppler ($f_{dn} = 0; \tau_n = 0$). That is,

$$\begin{aligned} |\chi[\lambda_n; f_{dn}]|_{peak}^2 &= |\chi[0; 0]|^2 = \left| \sum_{i=1}^N s[i] \times s^*[i] \right|^2 \\ &= E_s^2 = \left| \sum_{i=1}^N (x[i] * h[i]) \times (x[i] * h[i])^* \right|^2. \end{aligned} \quad (13)$$

It turns out that this peak is not constant given an extended target considering various transmit waveforms (in which the proof is discussed later). Before going into the extended target case, let us examine the classical point target case. If the target is a (non-fluctuating) point target then h has an impulse response (i.e., no extent) and thus the peak is given by

$$|\chi[\lambda_n; f_{dn}]|_{peak, point}^2 = E_s^2 = E_h^2 \left| \sum_{i=1}^N x[i] \times x[i]^* \right|^2 = E_h^2 E_x^2, \quad (14)$$

where E_h is the energy associated with the point target and it is clear from (14) that the AF peak is always a constant no matter what kind of waveform is used. In fact for point targets (non-fluctuating), the volume under the ambiguity function for all possible transmit waveforms is also constant and is given by $E_x^2 E_h^2$. If the received point target energy and transmit energy are normalized ($E_x^2 = 1; E_h^2 = 1$) then the peak is 1. The properties that AF peak and volume are constant regardless of transmit waveform are the basis of designing waveforms on how to manipulate ambiguity sidelobes in AF. We will show in this work that for an extended target, various AFs arise depending on the transmit waveform and the point-target properties do not hold for extended targets. Moreover, we discuss how we accurately implemented our own ambiguity function (in MATLAB) and how we verified our results in the Appendix.

B. PROPERTIES OF THE AMBIGUITY FUNCTION

1. Property 1: Given an extended target, the peak of the ambiguity function is different for different transmit waveforms.

In other words, the AF peak is not constant for all waveforms i.e., E_s^2 in (13) is not constant unlike in the point target case whose peak is constant as given by (14). We will now prove Property 1.

For compact representation, let \mathbf{h} be the complex-valued discrete-time target vector of length n , then we can easily form $\mathbf{h} = \sqrt{E_h} \bar{\mathbf{h}}$ where E_h is the energy of the target response and the normalized target response $\bar{\mathbf{h}}$ clearly has an energy of 1. Let \mathbf{x} be an arbitrary transmit signal vector of length n . From [7], we can form a normalized target convolution matrix given by

$$\bar{\mathbf{H}} = \begin{bmatrix} \bar{\mathbf{h}} & 0 & 0 & 0 \\ \cdot & \bar{\mathbf{h}} & 0 & 0 \\ \cdot & \cdot & \cdot & \cdot \\ \cdot & & & \bar{\mathbf{h}} \end{bmatrix}, \quad (15)$$

where $\bar{\mathbf{H}}$ is a $(2n-1)$ by n matrix. Thus, any arbitrary transmit waveform \mathbf{x} yields a corresponding ambiguity function whose peak is given by

$$\begin{aligned} |\chi[\lambda_n; f_{dn}]|_{peak}^2 &= \left| \sum_{i=1}^N (x[i] * h[i]) \times (x[i] * h[i])^* \right|^2 \\ &= \left| (\mathbf{x} * \mathbf{h})^H \times (\mathbf{x} * \mathbf{h}) \right|^2 = \left| (\mathbf{x} * \sqrt{E_h} \bar{\mathbf{h}})^H \times (\mathbf{x} * \sqrt{E_h} \bar{\mathbf{h}}) \right|^2 \\ &= E_h^2 \left| (\bar{\mathbf{H}} \mathbf{x})^H \times (\bar{\mathbf{H}} \mathbf{x}) \right|^2 = E_h^2 \left| \mathbf{x}^H \bar{\mathbf{H}}^H \bar{\mathbf{H}} \mathbf{x} \right|^2. \end{aligned} \quad (16)$$

It is clear in (16) that various peaks are possible depending on what \mathbf{x} is. In fact, it should be clear that the value of the peak depends on the how \mathbf{x} correlates with the target response (represented by $\sqrt{E_h} \bar{\mathbf{h}}$). If various peaks are possible, then it is our goal to find the ambiguity function (from all possible \mathbf{x}) which yields the maximum peak among all possible peaks.

The largest peak can be found by maximizing the AF peak for all possible transmit waveforms \mathbf{x} given \mathbf{H} via

$$\begin{aligned} & \max_{\forall \mathbf{x} | \mathbf{H}} |\chi[\lambda_n; f_{dn}]|_{peak}^2 \\ &= \max_{\forall \mathbf{x} | \mathbf{H}} |\chi[0; 0]|^2 = \max_{\forall \mathbf{x} | \mathbf{H}} E_h^2 |\mathbf{x}^H \bar{\mathbf{H}}^H \bar{\mathbf{H}} \mathbf{x}|^2, \end{aligned} \quad (17)$$

where we let

$$\bar{\mathbf{R}}_h = \bar{\mathbf{H}}^H \bar{\mathbf{H}}. \quad (18)$$

Based on the structure of $\bar{\mathbf{H}}$, $\bar{\mathbf{R}}_h$ will have the form

$$\bar{\mathbf{R}}_h = \frac{1}{E_h} \begin{bmatrix} \sum_i |h_i|^2 & \sum_i h_i h_{i+1}^* & \cdots & \sum_i h_i h_{i+N-1}^* \\ \sum_i h_{i+1} h_i^* & \sum_i |h_i|^2 & & \\ \cdots & & \cdots & \\ \sum_i h_{i+N-1} h_i^* & & & \sum_i |h_i|^2 \end{bmatrix}, \quad (19)$$

where all the diagonal components have the same energy as $\bar{\mathbf{h}}$ (which is 1). It can be shown with some effort that the matrix $\bar{\mathbf{R}}_h$ is conjugate symmetric, Toeplitz and positive definite. That is,

$$\bar{\mathbf{R}}_h = \bar{\mathbf{H}}^H \bar{\mathbf{H}} = (\bar{\mathbf{H}}^H \bar{\mathbf{H}})^H = \bar{\mathbf{R}}_h^H. \quad (20)$$

The $\bar{\mathbf{R}}_h$ matches exactly the definition of sample correlation function from [32] but without the normalization. We may refer to $\bar{\mathbf{R}}_h$ as the normalized target response autocorrelation matrix.

Notice that the only design parameter in (16) is the transmit waveform \mathbf{x} . In other words, maximizing the peak in (16) is equivalent to maximizing the argument $\mathbf{x}^H \bar{\mathbf{R}}_h \mathbf{x}$, which is given by

$$\max_{\forall \mathbf{x} | \mathbf{H}} E_h^2 |\mathbf{x}^H \bar{\mathbf{R}}_h \mathbf{x}|^2. \quad (21)$$

Notice the argument inside the squared magnitude in (21) is an eigenvalue problem [11] where the eigenvalue and eigenvector relation is given by

$$\overline{\mathbf{R}}_h \mathbf{q}_i = \lambda_i \mathbf{q}_i \quad (22)$$

and

$$\lambda_i = \frac{\mathbf{q}_i^H \overline{\mathbf{R}}_h \mathbf{q}_i}{\mathbf{q}_i^H \mathbf{q}_i} = \mathbf{q}_i^H \overline{\mathbf{R}}_h \mathbf{q}_i, \quad (23)$$

where λ_i is any eigenvalue of the autocorrelation matrix $\overline{\mathbf{R}}_h$ and \mathbf{q}_i is the corresponding unit-energy eigenvector of length n .

Thus, the largest peak of the ambiguity function is achieved by taking the eigenvector \mathbf{q}_{\max} corresponding to the largest eigenvalue λ_{\max} as the transmit waveform. In other words, the AF that produces the largest peak is the return that convolves the eigenwaveform with the target response. Since \mathbf{q}_{\max} is unit-energy, we need to incorporate any transmit energy constraint E_x , i.e., the transmit waveform is $\mathbf{x} = \sqrt{E_x} \mathbf{q}_{\max}$. Thus, the maximum AF peak given a target response correlation matrix is

$$\begin{aligned} \max_{\forall \mathbf{x} | \mathbf{H}} |\chi[\lambda_n; f_{dn}]|_{peak}^2 &= \max_{\forall \mathbf{x} | \mathbf{H}} E_h^2 \left| \mathbf{x}^H \overline{\mathbf{R}}_h \mathbf{x} \right|^2 \\ &= E_h^2 E_x^2 \left| \mathbf{q}_{\max}^H \overline{\mathbf{R}}_h \mathbf{q}_{\max} \right|^2 = \lambda_{\max}^2 E_h^2 E_x^2, \end{aligned} \quad (24)$$

which says that the maximum peak is given by the squared-product of maximum eigenvalue, target energy and transmit energy. Moreover, this maximum peak comes from the ambiguity function produced by using the eigenwaveform.

In conclusion, given any specific target response, the maximum peak value of the ambiguity function is attained by taking the eigenwaveform corresponding to maximum eigenvalue as transmit signal instead of any arbitrary waveform (and this includes traditional pulsed or wideband waveform). The maximum peak value is $\lambda_{\max}^2 E_h^2 E_x^2$ as opposed to E_s^2 in (14) whose value depends on both how well the transmit waveform matches with the target. Notice that a peak of $E_h^2 E_x^2$ can be attained by a special

waveform. This AF peak is attained by an idealized impulse waveform [7]. In our research, we implement the wideband waveform as practical implementation of the impulse waveform.

2. Property 2: Given an extended target, the volume of the ambiguity function is different for different transmit waveforms.

In other words, the AF volume is not constant for all transmit waveforms. We will now prove Property 2. The volume of the extended target ambiguity function is given by

$$V_{AF} = |\Delta \tau_n| \left| \frac{\Delta f_{dn}}{N} \right| \sum_{\tau_n} \sum_{f_{dn}} |\chi[\tau_n; f_{dn}]|^2. \quad (25)$$

It can be shown by Parsavel's theorem for discrete Fourier transform that

$$\sum_{i=0}^{N-1} |s[i] \times s^*[i - \tau_n]|^2 = \frac{1}{N} \sum_{f_{dn}=0}^{N-1} |\chi[\lambda_n; f_{dn}]|^2. \quad (26)$$

Thus, the AF volume becomes

$$\begin{aligned} V_{AF} &= \frac{1}{N} \sum_{\tau_n=-(N-1)}^{N-1} N \sum_{i=0}^{N-1} |s[i] \times s^*[i - \tau_n]|^2 \\ &= \sum_{\tau_n=-(N-1)}^{N-1} \sum_{i=0}^{N-1} |s[i] \times s^*[i - \tau_n]|^2. \end{aligned} \quad (27)$$

By substituting i_1 for i and substituting i_2 for $(i - \tau_n)$ where i_1 and i_2 cover the range from 0 to $(N - 1)$, the total volume of the ambiguity function is given by

$$\begin{aligned} V_{AF} &= \sum_{i_2=0}^{N-1} \sum_{i_1=0}^{N-1} |s[i_1] \times s^*[i_2]|^2 \\ &= \left(\sum_{i_1=0}^{N-1} |s[i_1]|^2 \right) \times \left(\sum_{i_2=0}^{N-1} |s^*[i_2]|^2 \right) = E_s^2 \\ &= E_h^2 \left| \mathbf{x}^H \overline{\mathbf{R}}_h \mathbf{x} \right|^2, \end{aligned} \quad (28)$$

where we use (22) and (24) complete the last line of the proof. It is clear that the AF volume for extended target is not constant and various waveforms can produce various volumes depending on the extended target response as well as the transmit waveform.

One of the waveforms we'll use in our work is the wideband (impulse) waveform. An extended target illuminated by the wideband waveform has a volume that is given by

$$V_{AF} = |\Delta \tau_n| \left| \frac{\Delta f_{dn}}{N} \right| \sum_{\tau_n} \sum_{f_{dn}} |\chi[\tau_n; f_{dn}]|^2 = E_h^2 E_x^2. \quad (29)$$

This is very interesting since this is the same volume produced if we illuminate a point target with any transmit waveform. In other words, for extended targets, only the wideband waveform can produce this volume. With the use of the eigenwaveform, the largest AF volume possible is given by

$$V_{AF} = |\Delta \tau_n| \left| \frac{\Delta f_{dn}}{N} \right| \sum_{\tau_n} \sum_{f_{dn}} |\chi[\tau_n; f_{dn}]|^2 = \lambda_{\max}^2 E_h^2 E_x^2. \quad (30)$$

In other words, the volume is the same value as the largest peak. This volume is amplified by λ_{\max}^2 compared to that of the volume produced by the wideband waveform.

IV. AMBIGUITY FUNCTIONS OF ONE-PULSE WAVEFORMS

A. EIGENWAVEFORM, WIDEBAND WAVEFORM, AND RECTANGULAR WAVEFORM

Traditionally for point targets, a basic pulse (usually shaped) is a common choice for transmit signal. For extended targets in this work, we will choose two pulse-type waveforms and compare that to the eigenwaveform. The waveforms are: wideband waveform (i.e., a very narrow pulse compared to the length of the extended target) and rectangular waveform (i.e., a rectangular pulse with duration less or equal to that of the extended target). Given a target response, we derive and illustrate ambiguity functions for these two waveforms and compare them to the ambiguity function of the eigenwaveform. In Fig. 3, we illustrate the finite-length of the three waveforms (wideband, rectangular, and eigenwaveform) as they interact with an extended target whose response has finite support T .

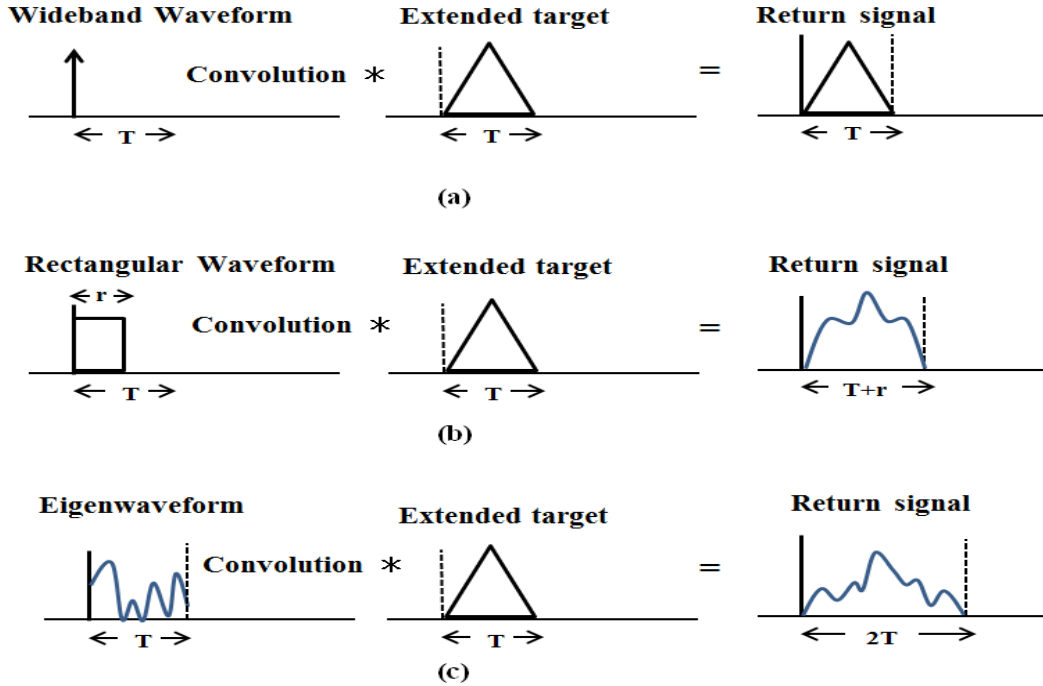


Figure 3. One-pulse transmit waveform for extended target: (a) wideband waveform, (b) rectangular waveform, and (c) eigenwaveform.

Let T_x be the time duration of any transmit waveform. As mentioned earlier, we assume the extent of the wideband pulse is much less than the target response duration. As such, in Fig. 2a we may idealize the wideband pulse to be an impulse ($T_x \sim 0$). For rectangular waveform, the pulse width is $T_x = r$ as shown in Fig. 2b. The length r may be thought of as time-on-target (ToT) and the ratio of T_x to T is defined as the time-on-target ratio (ToTR) and is given by

$$\text{ToTR} = \frac{r}{T}. \quad (31)$$

In Fig. 2c, the eigenwaveform is shown to have the same length as the target duration and thus the ToTR is equal to 1. For a wideband waveform, $\text{ToTR} = T_x / T$ where $T_x \ll T$. In the example simulations (in this work) using the wideband waveform, T_x / T is 1/31. For this section, we concentrate on one-pulse waveforms to gain insight into the ambiguity functions of these three waveforms as they convolve with target responses. For illustration in this work, we form two targets with very different frequency responses and set both the transmit energy and the target energy to be unit-energy ($E_x = 1$ and $E_h = 1$). We will keep using these two targets for comparison to illustrate the fact that unlike in the case of point targets, the target responses play important roles in the formation of ambiguity functions. In Fig. 4, we present the magnitudes of frequency responses of two different targets (top panel), the corresponding frequency responses of the eigenwaveforms (middle panel), and the frequency responses of their return echoes (bottom panel). From Fig. 4, we can conclude that choosing the eigenvector with the maximum eigenvalue of target autocorrelation matrix as the transmit signal is tantamount to choosing a band of frequencies (Fig. 4 middle panel) where the echoes (Fig. 4 bottom panel) guarantee the largest returns in terms of magnitudes [1], [7]. Interestingly, the magnitudes of the return frequency responses exhibit suppression of the less dominant frequency bands of the target response. This turns out to be important since this suppression effect will translate to sidelobe suppression in the ambiguity function of target returns illuminated by eigenwaveforms. For the purposes of illustration in this

work, we form two target types where each represents something practically meaningful. Target 1 (a name that we will now use for consistency throughout the work) illustrated in Fig. 4 (left top panel) with two dominant bands represents targets with oscillatory tendencies in time domain while Target 2 (also to be used consistently herein) in Fig. 4 (right top panel) with a low-pass shape represents targets exhibiting less or non-oscillatory tendencies in the time domain. Target 2 is actually a low-pass shaped pulse in time domain, which represents a set of target responses that have a strong initial return but decays off in time. In other words, we have two target responses that represent potential practical target responses and thus we can illustrate how each extended target type will respond to the three waveforms we are to investigate.

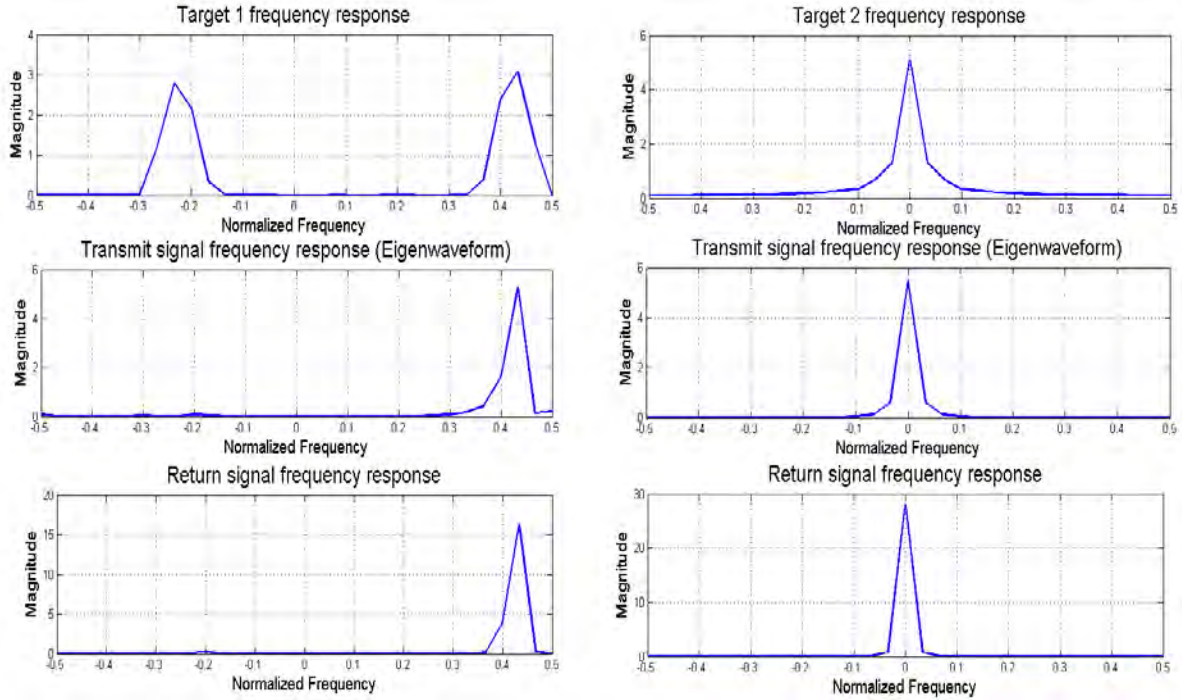


Figure 4. Top panel: target frequency response, middle panel: eigenwaveform frequency response, and bottom panel: return signal frequency response.

Moreover, the actual radar range profile of a Boeing 737–500 [33] is converted to a practical target response and used an example to generate a practical eigenwaveform and corresponding AF. This response is shown in Fig. 5.

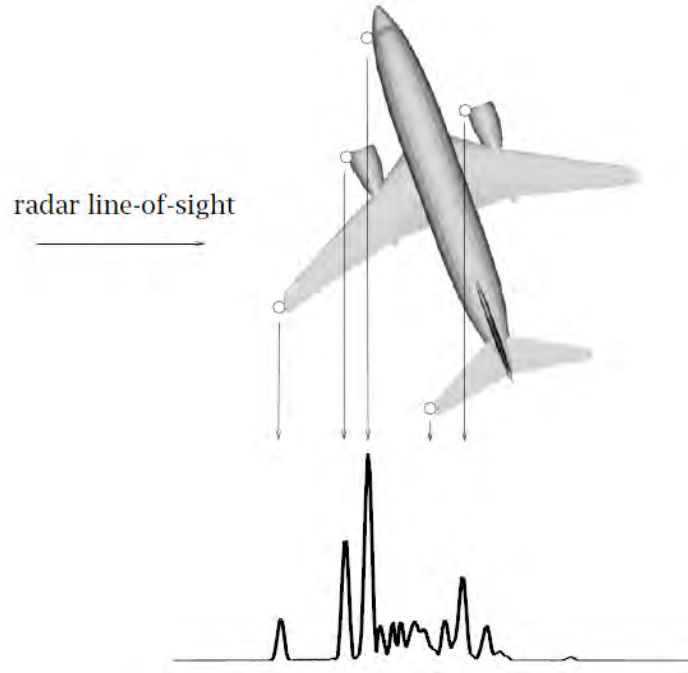


Figure 5. Example of a range profile of a Boeing 737-500 used as Target 3. The radar range profile is at the bottom. From [33].

B. EIGENWAVEFORM VS. WIDEBAND AMBIGUITY FUNCTIONS

A quick and very insightful trade-off comparison is to use an eigenwaveform and the wideband waveform as transmit waveforms. In this scenario, we utilize Target 1 ($n = 31$ samples). In Fig. 6, the ambiguity functions (3D and contour plots) of wideband transmit waveform and eigenwaveform are calculated and illustrated.

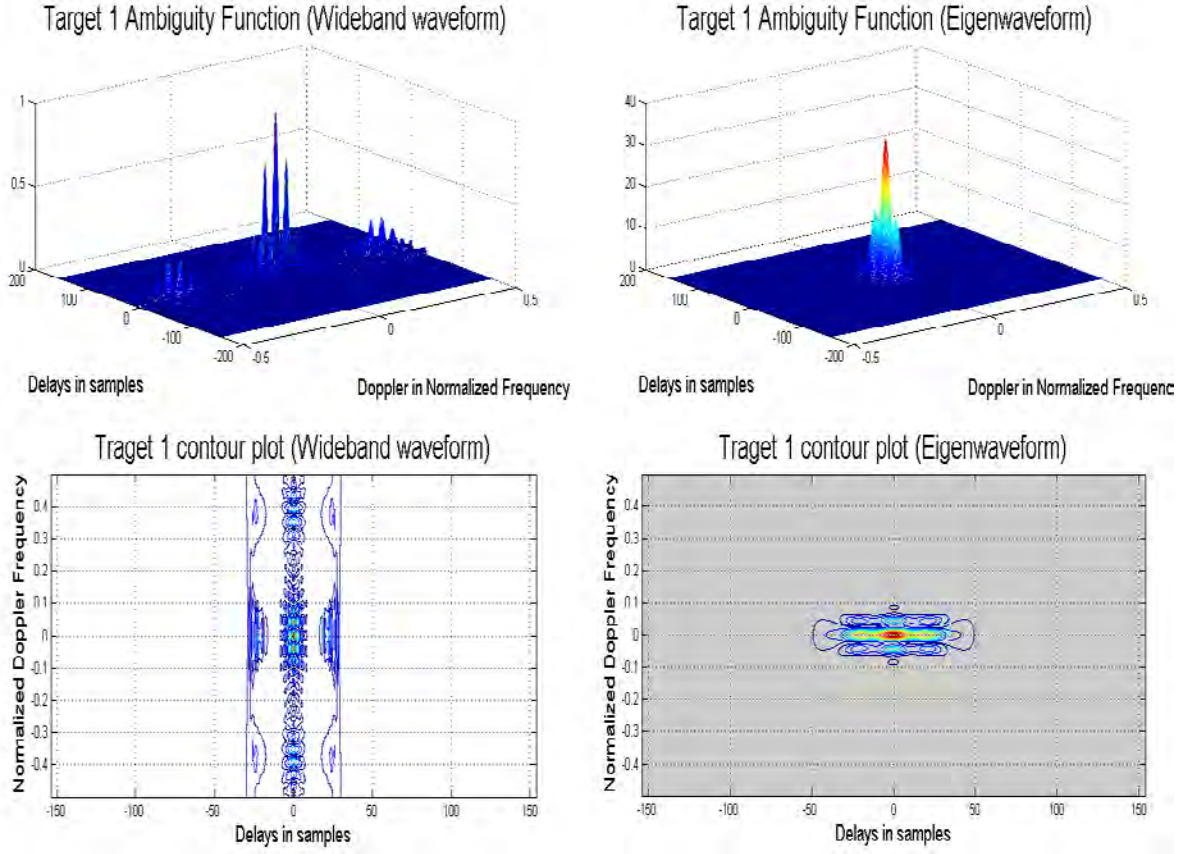


Figure 6. Ambiguity function and AF contour plots of Target 1 illuminated by wideband waveform vs eigenwaveform. Top panel: 3-D view, and bottom panel: contour plots.

It is clear that the ambiguity function of eigenwaveform is more compact in terms of Doppler (frequency) response compared the wideband waveform. The cleaner Doppler response is the result of two factors. The major factor is the fact that eigenwaveform exhibits narrowband characteristics that suppresses the less dominant target frequencies. The minor factor is the fact the length of the return echo for the eigenwaveform is about twice that of the wideband waveform. Increasing length of transmission results in the increase of Doppler resolution. While Doppler resolution was defined earlier in terms of time of return echo, a related concept defines Doppler resolution to be half the effective mainlobe width in the Doppler domain given a fixed delay (usually when delay is zero). This is also true in range resolution where delay (or range) resolution is usually taken to be half the effective mainlobe width in the time-delay domain given a fixed Doppler

frequency (usually $f_d = 0$). Sidelobe suppression in the ambiguity function is usually a desired design characteristic for traditional waveforms for point targets. Here, the eigenwaveform has an inherent feature of being able to suppress sidelobes in the Doppler domain of the ambiguity function. Since the length of the return for the eigenwaveform is approximately twice of that of the wideband waveform (recall Fig. 3 and Fig. 6 bottom panel) the mainlobe length (when looking at the delay spread) of the eigenwaveform AF is larger compared to the mainlobe length of the wideband AF. In other words, the range resolution of the wideband waveform is slightly better than the eigenwaveform. However, the eigenwaveform AF contour is clearly much cleaner (due to suppression effect and the Doppler resolution effect of longer return) than the wideband waveform. Concentrated energy in the origin of the AF is desired in radar waveform design for avoiding ambiguities. Also bigger sidelobes can cause a threshold to be crossed, which can cause increase in probability of false alarms (PFA). Compared to the wideband waveform, the reduction in range resolution is a small price to pay considering better Doppler resolution and the qualitative sidelobe reduction. Indeed, it is a small price to pay when we consider the peak value of eigenwaveform AF compared to wideband AF (since peak value translates to improved detection performance). In Fig. 6 where Target 1 is used ($E_x = 1$, $E_h = 1$), the peak of the eigenwaveform AF is 33.52 ($\lambda_{\max} = 5.79$) while the peak of the wideband AF is 1.

C. RECTANGULAR WAVEFORM AF FOR OSCILLATORY TARGET (TARGET 1)

The ambiguity function from the use of rectangular transmit waveform depends on r relative to T (i.e., ToTR) in Fig. 3. In this section, we consider two rectangular waveforms: a low-ToTR and a high-ToTR. Using a high-ToTR of 0.64, we illustrate in Fig. 7: a. AF, b. AF contour, c. Target 1 frequency response (magnitude), d. transmit signal frequency response (magnitude), and e) return signal frequency response (magnitude). Using a low-ToTR of 0.09, we illustrate in Fig. 8: a. AF, b. AF contour, c. Target 1 frequency response (magnitude), d. transmit signal frequency response (magnitude), and e. return signal frequency response (magnitude). The AF peak of high-ToTR in Fig 7 is lower (0.0298) compared to the AF peak (0.2482) of the low-ToTR

rectangular waveform. This is because transmit spectrum's main lobe (sinc-function in frequency domain) shown in Fig. 7d barely overlaps the two dominant frequency bands of Target 1 (in Fig. 7c) thereby reducing the energy return as shown in Fig. 7e. Notice that there are also some subpeaks and sidelobes in AF for the high-ToTR rectangular pulse. On the other hand, low ToTR has a better peak value in the ambiguity function but a qualitatively worse Doppler response. This is because the low-ToTR rectangular waveform has a wider response (in frequency domain) than the high-ToTR rectangular waveform and therefore allows for more frequencies to appear. To conclude, given unit-transmit energy ($E_x = 1$) and unit-target energy ($E_h = 1$), we note that the AF peak values for both rectangular waveforms are both lower than 1. Recall that the wideband waveform AF has a peak value of 1 while the eigenwaveform has a peak value of λ_{\max}^2 , which is 33.52 for Target 1. In other words, rectangular waveforms (low-pass shape in frequency domain) are not good waveforms for Target 1 when it comes to AF peaks.

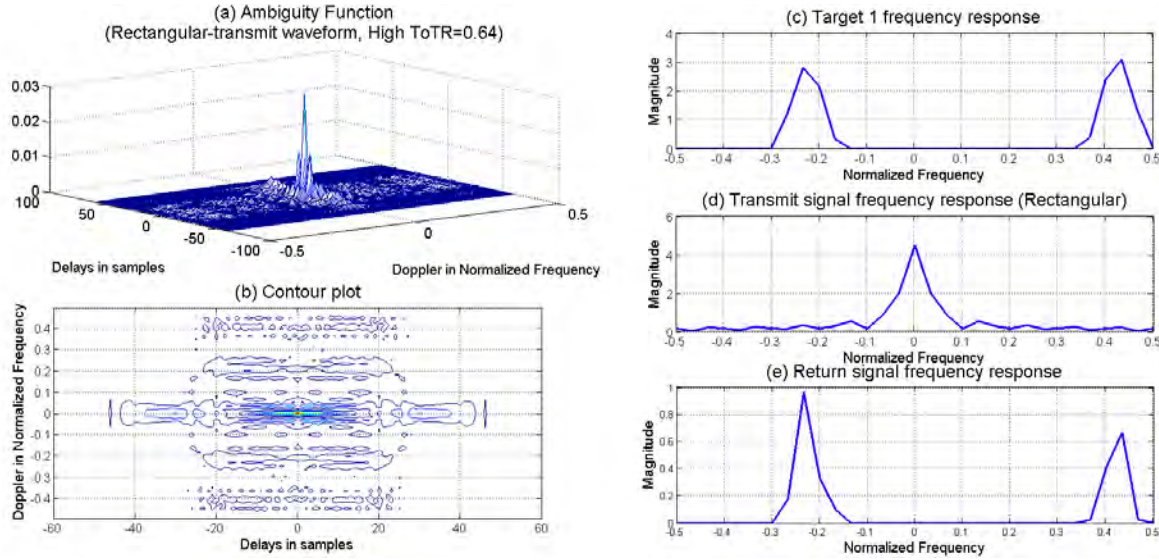


Figure 7. Ambiguity function analysis of rectangular waveform with Target 1 (ToTR = 0.64): (a) ambiguity function, (b) AF contour plot, (c) Target 1 frequency response (magnitude), (d) transmit signal frequency response (magnitude), (e) return signal frequency response (magnitude).

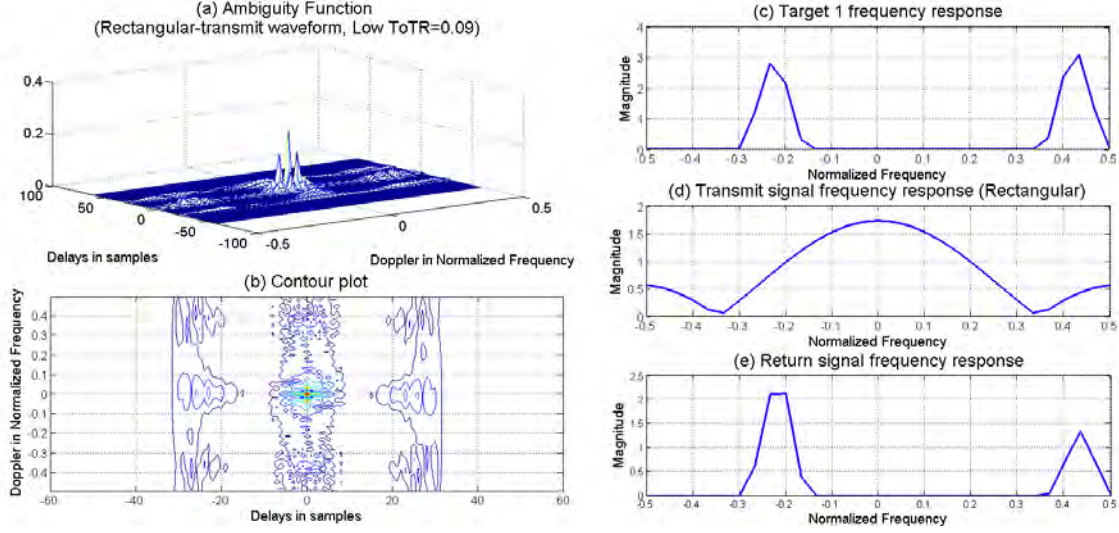


Figure 8. Ambiguity function analysis of rectangular waveform with Target 1 (ToTR = 0.09): (a) ambiguity function, (b) AF contour plot, (c) Target 1 frequency response (magnitude), (d) transmit signal frequency response (magnitude), (e) return signal frequency response (magnitude).

D. RECTANGULAR WAVEFORM AF FOR NON-OSCILLATORY TARGET (TARGET 2)

In this section, we consider a less-oscillatory target or non-oscillatory target in which Target 2 is a good example. Again we let $E_x = 1$ and $E_h = 1$. From previous example, we have already gained the insight that the wideband AF peak is 1 and that it has a slightly better range resolution than the eigenwaveform and rectangular waveform. Thus, we are able to make comparison with rectangular waveform AF without generating the wideband AF. While the rectangular waveforms (low and high ToTR) do not work well for oscillatory targets, the rectangular waveforms actually perform well in terms of AF peaks for the non-oscillatory Target 2 compared the wideband waveform. For this example scenario, it is instructive to just use one of the rectangular waveforms to compare with the eigenwaveform. We choose to look at the high-ToTR rectangular waveform AF and compare that to the eigenwaveform AF for Target 2. Using a high-ToTR of 0.64, we illustrate in Fig. 9: a. AF, b. AF contour, c. Target 2 frequency response (magnitude), d. transmit signal frequency response (magnitude), and e. return

signal frequency response (magnitude). Using the eigenwaveform, we illustrate in Fig. 10: a. AF, b. AF contour, c. Target 2 frequency response (magnitude) of target response, d) transmit signal frequency response (magnitude) of rectangular waveform, and e. return signal frequency response (magnitude). Notice that the high-ToTR rectangular waveform AF has a decent peak (232.38). In hindsight, such a result may not be surprising since Target 2 is a low-pass shaped response and that a rectangular pulse should return a large echo specially if the durations of target and rectangular waveform are comparable. Looking at rectangular waveform AF contour in Fig. 9b, the overall sidelobe level is also low (of course this is very much influenced by the fact that both target and transmit waveform response are concentrated near the zero Herz frequency). Notice however that AF peak resulting from the eigenwaveform is still higher (377.45, which is the square of $\lambda_{\max} = 19.4281$). Looking at the eigenwaveform AF contour in Fig. 10b, the Doppler spread is narrower than that of Fig. 9b. In this case of non-oscillatory target, the rectangular AF peak is clearly much higher than the wideband waveform AF peak (which is 1).

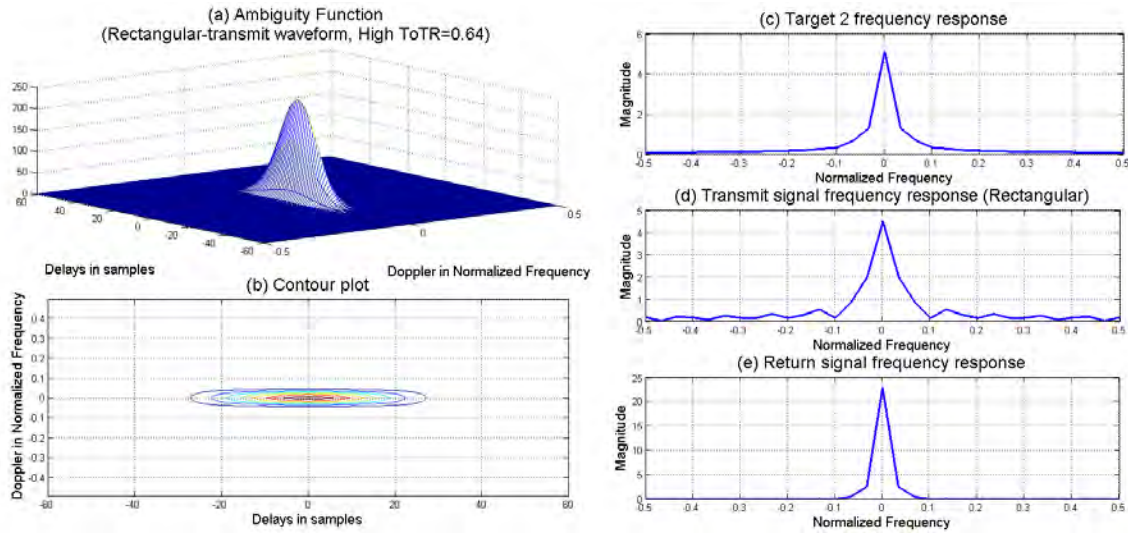


Figure 9. Ambiguity function analysis of rectangular transmit waveform with Target 2 (AF peak value = 232.38): (a) ambiguity function, (b) AF contour plot, (c) Target 2 frequency response (magnitude), (d) transmit signal frequency response (magnitude), and (e) return signal frequency response (magnitude).

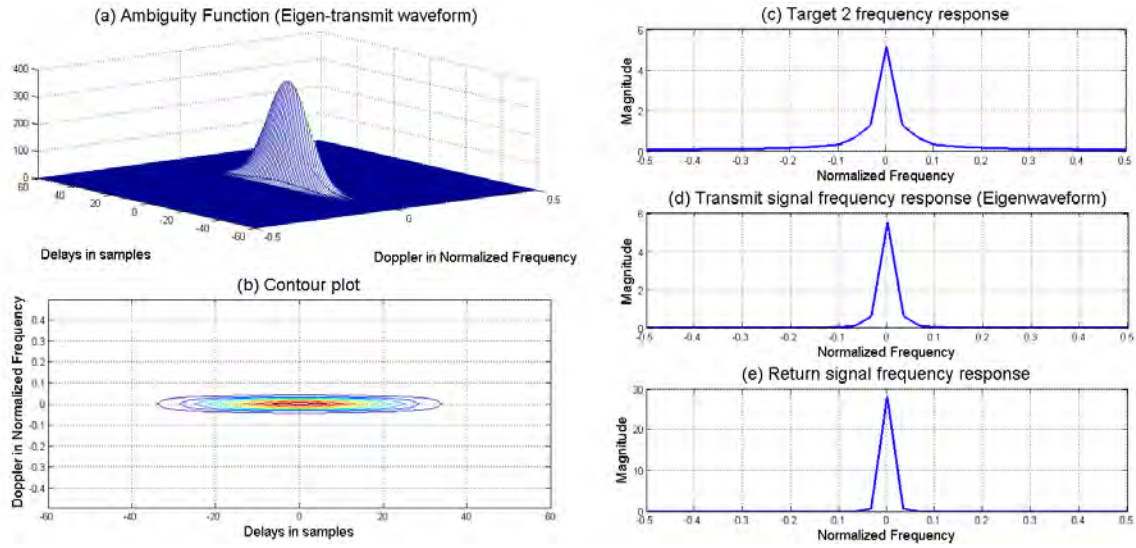


Figure 10. Ambiguity function analysis of eigenwaveform with Target 2 (AF peak value = 377.45): (a) ambiguity function, (b) AF contour plot, (c) Target 2 frequency response (magnitude), (d) transmit signal frequency response (magnitude), and (e) return signal frequency response (magnitude).

E. PRACTICAL TARGET (BOEING 737–500 RANGE PROFILE)

We now consider an actual target response shown in Fig. 5 of a Boeing 737–500 and we generate in Fig. 11 (for eigenwaveform) and Fig. 12 (for wideband waveform) the: a. AF, b. AF contour, c. frequency response (magnitude) of Boeing 737–500 profile, d) transmit signal frequency response (magnitude) and e. Boeing 737–500 return signal frequency response (magnitude). The eigenvalue of Boeing 737–500’s range profile in Fig. 5 is 60.173 which leads to a very high peak value 3620.9 in Fig. 11 while Fig. 12 with wideband waveform can only achieve 1, which is the theoretical result by using wideband waveform. Moreover, the eigenwaveform eliminates most Doppler sidelobes but doubles the length of return signal. In this example, this type of response is more like our Target 2.

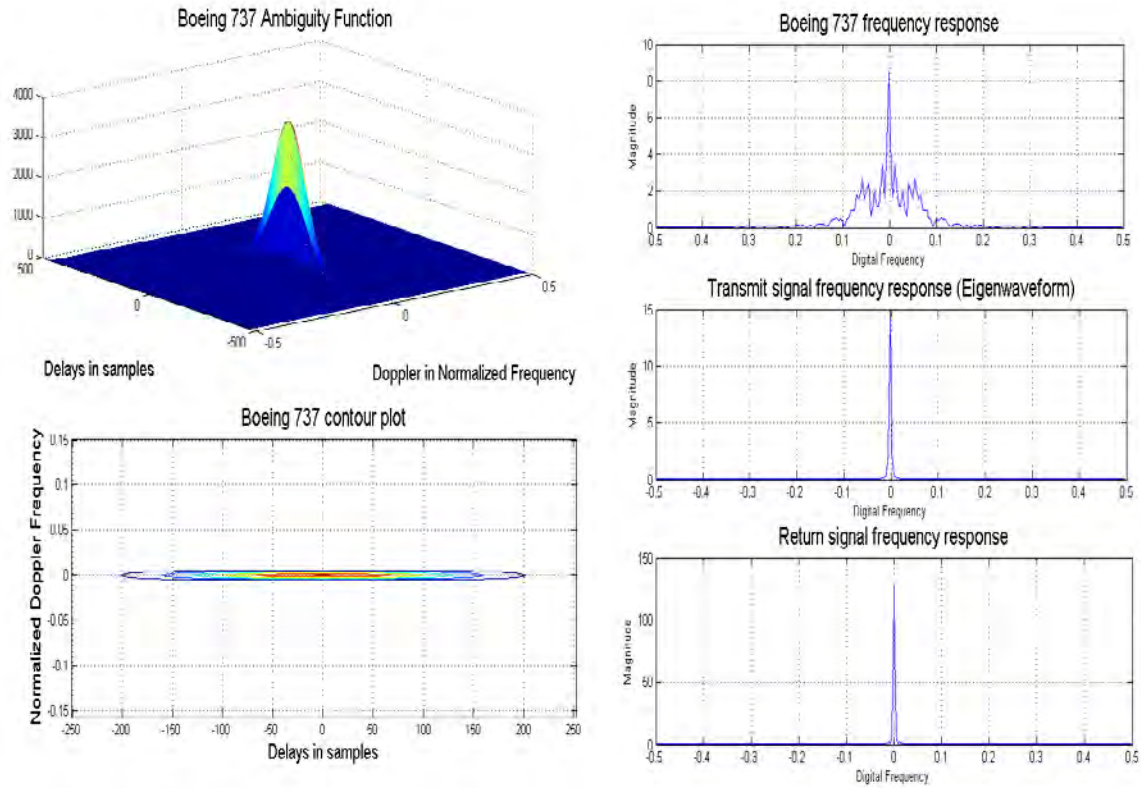


Figure 11. Ambiguity function analysis of eigenwaveform with Boeing 737–500: (a) ambiguity function, (b) AF contour plot, (c) Boeing 737–500 frequency response (magnitude), (d) transmit signal frequency response (magnitude), and (e) return signal frequency response (magnitude).

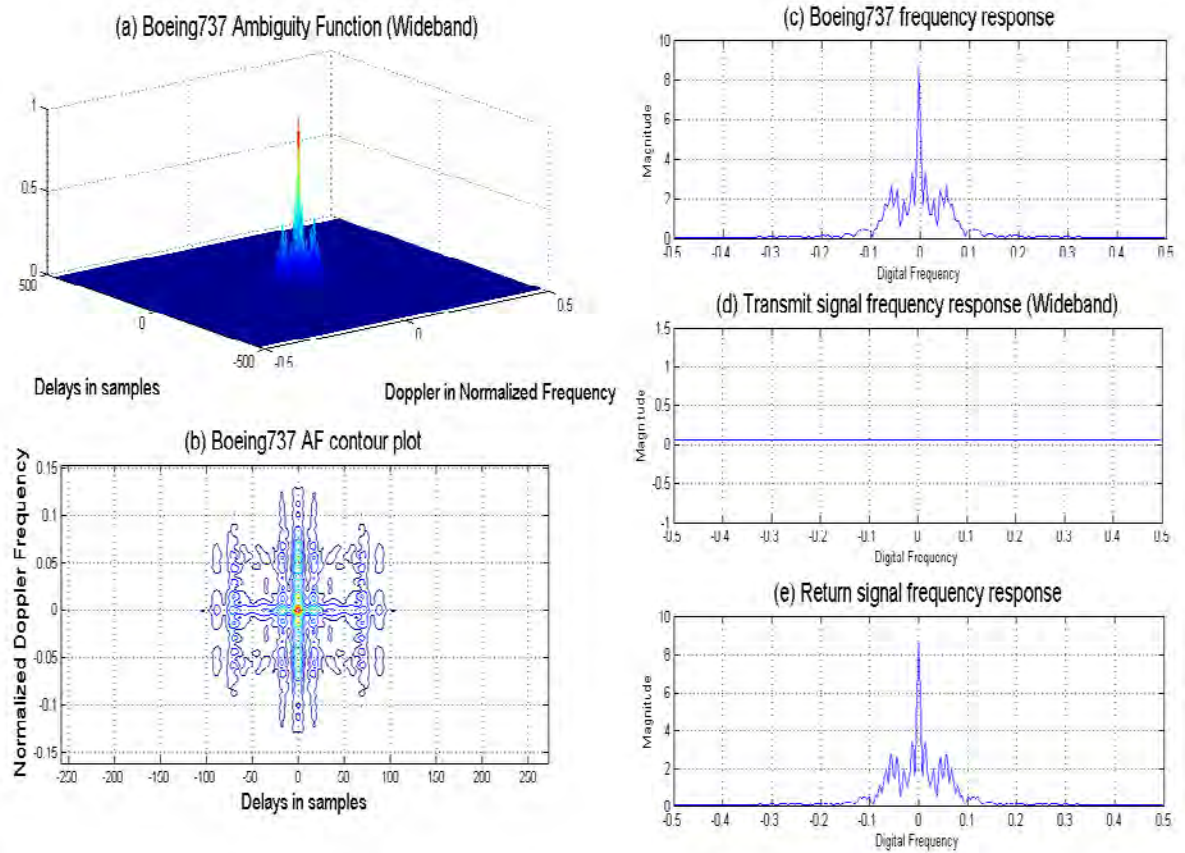


Figure 12. Ambiguity function analysis of wideband waveform with Boeing 737–500: (a) ambiguity function, (b) AF contour plot, (c) Boeing 737–500 frequency response (magnitude), (d) transmit signal frequency response (magnitude), and (e) return signal frequency response (magnitude).

In conclusion we notice that for oscillatory targets (target responses with resonances in particular bands) the wideband waveform tends to result in a larger peak than the rectangular waveform. For less oscillatory targets in which the particular Boeing 737–500 response is an example, the rectangular waveform tends to result in a larger peak than the wideband waveform. However, regardless of the target response, the eigenwaveform provides the largest AF peak compared to both waveforms. Qualitatively, the overall AF sidelobe suppression of the eigenwaveform is clearly superior than both waveforms.

F. AF ZERO-DELAY AND ZERO DOPPLER CUTS FOR EXTENDED TARGETS

In ambiguity function analysis, two cross sections are usually of interest: the AF zero-delay and the zero-Doppler cuts. The zero-delay cut is simply the AF cross-section when $\tau_n = 0$ and zero-Doppler cut is the AF cross section when $f_{dn} = 0$. The cross-sections are important since they usually convey delay (or range) resolution and Doppler (or velocity) resolution. For classical waveforms, the zero-delay cut is given by

$$|X[0; f_{dn}]|^2 = \left| \sum_{n=1}^N x[n] \times x^*[n] \times W_N^{f_{dn}n} \right|^2, \quad (32)$$

where

$$W_N^{f_{dn}} = e^{j2\pi \frac{f_{dn}}{N}}$$

and $x[n]$ is the transmit signal. Unfortunately, this does not work for extended targets. However, recall that we incorporated the fact that the target has finite extent in (16), which simplifies to

$$|X[0; f_{dn}]|^2 = \left| \sum_{n=1}^N s[n] \times s^*[n] \times W_N^{f_{dn}n} \right|^2, \quad (33)$$

where $s[n] = x[n] * h[n]$ is the return echo.

Notice that we can simplify (33) to

$$|\chi[0; f_{dn}]|^2 = \left| \sum_{n=1}^N |s[n]|^2 \times W_n^{f_{dn}n} \right|^2 = \left| IFFT[|s[n]|^2] \right|^2, \quad (34)$$

which states that the AF zero-delay is simply the squared-magnitude of inverse (fast) Fourier transform of the squared-magnitude of the transmit waveform - target response convolution.

The corresponding zero-Doppler cut is then the squared-autocorrelation function of the return echo (rather than just the transmit signal) and is therefore given by

$$|\chi[\tau_n; 0]|^2 = \left| \sum_{n=1}^N s[n] \times s^*[n - \tau_n] \right|^2 \equiv |R_s[\tau_n]|^2. \quad (35)$$

The significance of the AF zero-delay and zero-Doppler cuts are illustrated using transmissions with multiple pulses which is the topic of the next section.

V. COHERENT MULTIPLE-PULSE TRANSMISSION

When multiple-pulse transmission or coherent pulse train is used, the ambiguity function is the superposition of the ambiguity function of a single transmission with some amplitude re-scaling. From [12], the ambiguity function for a pulse train return is given by

$$|\chi(\tau; f_d)|^2 = \frac{1}{L} \sum_{q=-(L-1)}^{L-1} |\chi_1(\tau - qT_R; f_d)|^2 \left| \frac{\sin[\pi f_d (L - |q|) T_R]}{\sin(\pi f_d T_R)} \right|^2, \quad (36)$$

where $|\chi_1|^2$ is the ambiguity function of a single transmit waveform-target response pair. L is the number of pulses in a transmission and T_R is the separation between pulses or pulse repetition interval (PRI). The pulse repetition frequency (PRF) is defined as

$$f_R = \frac{1}{T_R}. \quad (37)$$

In pulsed Doppler radar system, one of the key design elements is PRF. In practice, the definition of low, medium, and high PRF is truly application driven. This is because the PRI (or PRF) dictates the desired or specified unambiguous range. The unambiguous range is given by

$$R_{ua} = \frac{cT_R}{2} = \frac{c}{2\text{PRF}}, \quad (38)$$

or the unambiguous delay is given by

$$T_{ua} = \frac{T_R}{2} = \frac{1}{2\text{PRF}}. \quad (39)$$

When using coherent pulses, the Doppler resolution is basically half the mainlobe of the zero-Doppler cut of (36). It is given by

$$f_{d,\rho} \approx \frac{1}{LT_R}. \quad (40)$$

In practice, a simple rule of thumb is that medium PRF is a decade larger than low PRF and the high PRF is a decade larger than medium PRF but such rule is easily broken depending on application. For the convenient illustration of the PRF concepts in our work when illuminating an extended target, we will simply define the following: a. high PRF is when T_R is four to ten times T (target duration), b. medium PRF is when T_R is forty times T , and c. low PRF is when T_R is a hundred times T . Here our definition of high PRF is pretty high. For example, even with $T_R = 10T$, the unambiguous range is $T_{ua} = T_R / 2 = 10T / 2 = 5T$. In other words, the unambiguous delay for this PRF can accommodate about five target responses. This choice is not motivated by maximizing or minimizing the unambiguous range from some specific application but rather to show what happens when a (very) high PRF is lowered into medium PRF and then lowered again to a low PRF. In other words, we vary the length of T_R to investigate how the different PRFs affect the ambiguity function in terms of how the volume inside the AF changes and how range and Doppler resolution may be affected as the PRI or PRF is changed. As pointed out earlier, the volume of the ambiguity function may be manipulated depending on the waveform choice.

Another parameter of interest in a pulse train is the duty cycle where

$$d_t = \frac{T_x}{T_R} = T_x \times f_R. \quad (41)$$

Multiple-pulse transmissions convolving with finite-duration targets resulting in multiple echoes are illustrated in: Fig. 13a using wideband waveform, Fig. 13b using rectangular waveform, and Fig. 13c using eigenwaveform.

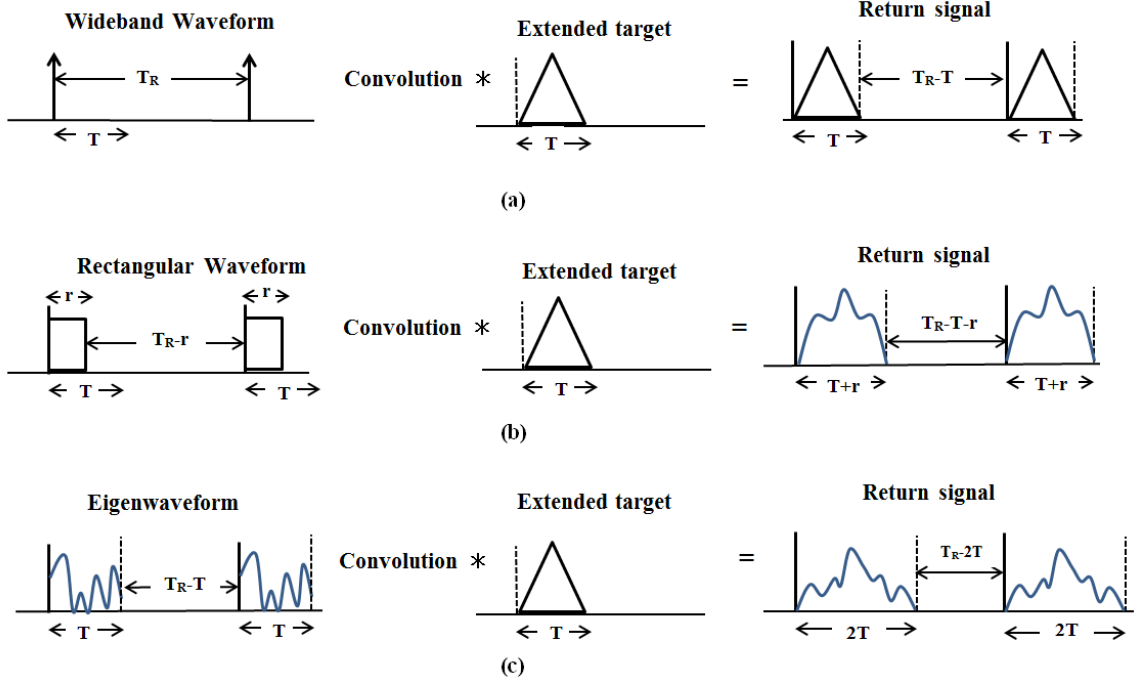


Figure 13. Multiple-pulse transmission for extended target setting: (a) wideband waveform, (b) rectangular waveform, and (c) eigenwaveform.

In Fig. 14 and Fig. 15 using $L = 3$ pulses and $T_R = 124$ delay samples, AF contours are shown using the wideband, high-ToTR rectangular, and eigenwaveform pulse trains for Target 1 and Target 2 respectively. It is clear all the waveforms (rectangular waveform, wideband and eigenwaveform) are very high PRF (AF contours are very close in delay spread since $T_R = 4T$) regardless whether it is Target 1 or 2. In Fig. 14 (with Target 1), we can deduce from the AF contour that the very high-PRF rectangular waveform yields a slightly cleaner sidelobe suppression response compared to the wideband waveform. However, its AF peak (which is 0.0298) is lower than the AF wideband waveform peak (which is 1). We can also deduce that the wideband waveform has the tightest range (delay) response. The eigenwaveform produces the largest peak (which is 33.5), tightest Doppler response, and we can also see that it qualitatively produces the cleanest overall sidelobe suppression level. In Fig. 15 with Target 2, all the waveforms have low overall sidelobe levels with the eigenwaveform having the tightest AF response in Doppler spread. As expected the wideband waveform has the tightest AF response in the range (delay) domain but it also has the lowest peak (which is 1). The

rectangular waveform has a decent peak (which is 232.38) but the eigenwaveform has the largest peak (which is 377.45).

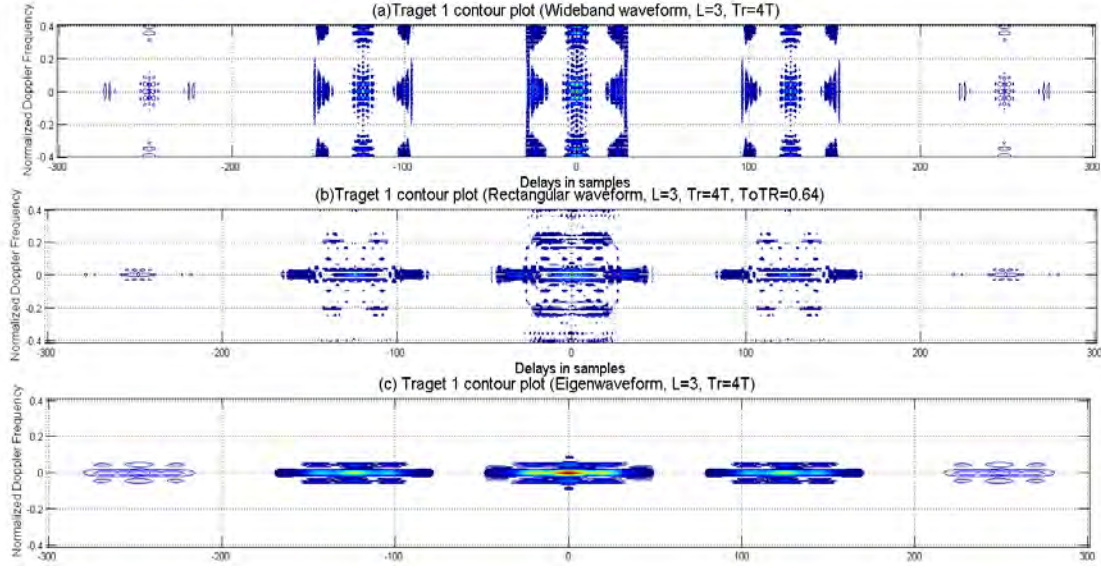


Figure 14. Target 1 ambiguity function contour plots comparison ($L = 3$, $T_r = 4T$): (a) wideband waveform, (b) rectangular waveform, and (c) eigenwaveform.

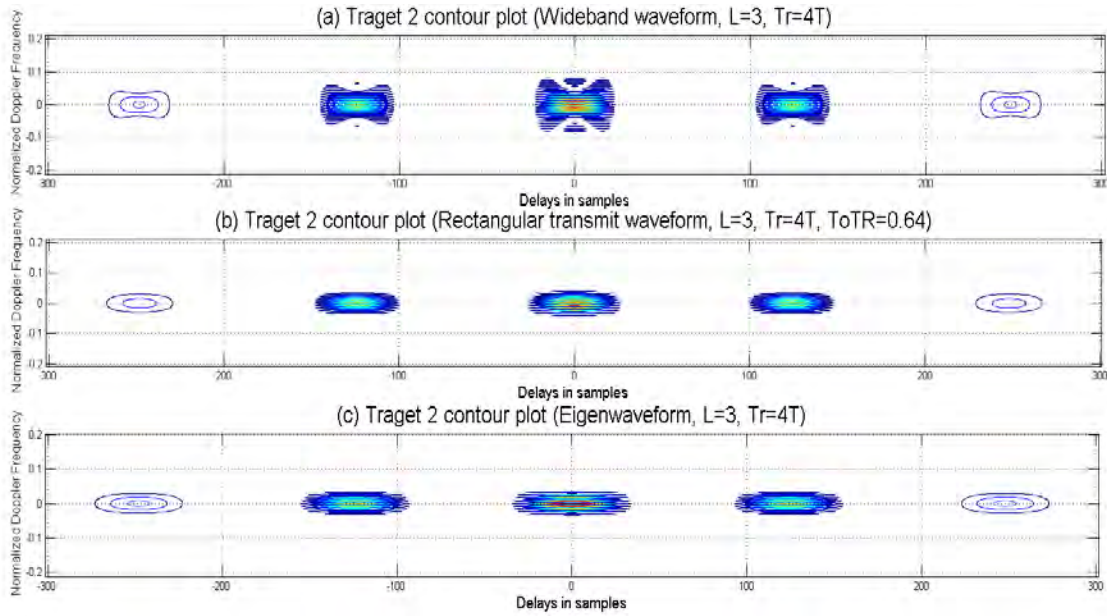


Figure 15. Target 2 ambiguity function contour plots comparison ($L = 3$, $T_r = 4T$): (a) wideband waveform, (b) rectangular waveform, and (c) eigenwaveform.

A. ZERO-DOPPLER CUT

Utilizing our high-PRF definition $T_R = 10T$, 3-pulse transmission, and Target 1, we illustrate the AF zero-Doppler cuts of the wideband waveform, rectangular waveform, and eigenwaveform in Fig. 16. It is clear from Fig. 16 that the range resolution of the wideband waveform is slightly better than the other two waveforms as was already inferred from the AF contours of Fig. 14. The peak is clearly apparent (and is the largest) for the eigenwaveform AF. These are the advantages of looking at another perspective via zero-Doppler cuts that may not be evident from the AF contours.

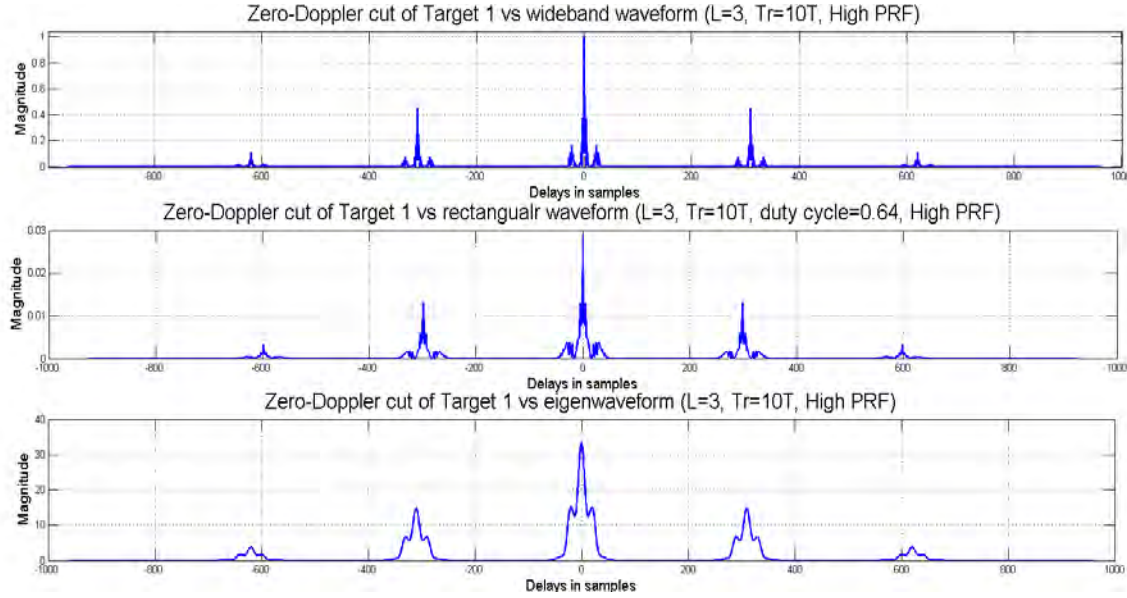


Figure 16. Zero-Doppler cut of Target 1 AF with various waveforms. Upper panel: wideband waveform ($L = 3$, high PRF), middle panel: rectangular waveform ($L = 3$, $T_o T_R = 0.64$, high PRF), and lower panel: eigenwaveform ($L = 3$, high PRF).

Moreover, when eigenwaveform is used, $T_R = 4T$ (in Fig. 14c and Fig. 15c) is the smallest value so that the zero-Doppler cut matched filtered pulse returns do not overlap. Thus, $T_R = 4T$ is the minimum PRI (T_{Rmin}) such that the AF matched-filtered return echoes from the same target do not overlap. If T_R is increased with the use of eigenwaveform, then the matched filtered pulse returns start to overlap. Thus, the

maximum PRF allowable if no overlap in the eigenwaveform AF zero-Doppler cut is desired is given by

$$f_{R\max} = \frac{1}{T_{R\min}} = \frac{1}{4T}. \quad (42)$$

The PRI $T_R = 4T$ translates to the actual pulse returns being separated by $2T$ from the same target. This is not to be confused from $T_p = 1.5T$ (mentioned in an earlier section), which is the minimum time separation required for two targets such that pulse returns from the two targets do not overlap (i.e., such that the two targets can be resolved).

It is interesting to note in Fig. 16 that the ratio of each first sidelobe peak to mainlobe peak for all three zero-Doppler cuts to be 0.44 for $L = 3$ scenario. The ratio 0.44 is the square of $(2/3)$. The ratio of each sidelobe peak to mainlobe peak can be formulated for any L as

$$P_i = \left(\frac{L-i}{L} \right)^2 \quad (43)$$

where P_i is the ratio of i^{th} side peak amplitude to main peak amplitude.

Another useful comparison is to illustrate the AF zero-Doppler cuts for various PRFs given a particular waveform. Utilizing the eigenwaveform and $L = 3$, we show the zero-Doppler cuts for high PRF, medium PRF, and low PRF in Fig. 17. Just like in traditional pulsed-Doppler waveforms, the low PRF yields the best unambiguous range. However, just like in pulsed-Doppler waveforms, the choice between low, medium, and high PRF has an impact in the Doppler domain, which is considered shortly.

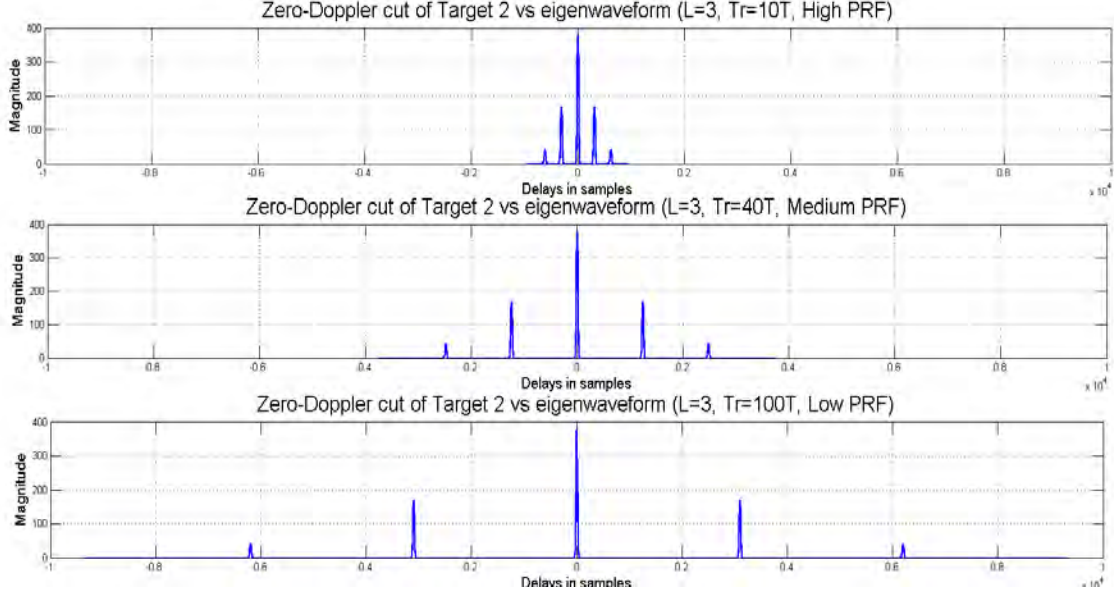


Figure 17. Zero-Doppler cut of Target 2 AF with normalized eigenwaveforms and various PRFs. Upper panel: ($L = 3$, high PRF), middle panel: ($L = 3$, medium PRF), and lower panel: ($L = 3$, low PRF).

Also, we explore the impact of increasing the number of pulses ($L = 1, 3, 5$) given a fixed PRF. Again, utilizing the eigenwaveform, we illustrate the AF zero-Doppler cuts for Target 1 with high PRF. Of course, $L = 1$ is an one-pulse waveform which is shown to illustrate what is gained by coherent pulse integration when using multiple pulses. Since the PRF is fixed, the separation between lobes for $L = 3$ and $L = 5$ are the same. The main gain of coherent integration is clearly the gain, which is L^2 , but at the expense of higher first sidelobe-to-main peak ratio (0.44 for $L = 3$ and 0.64 for $L = 5$) as predicted by (43).

In general (when no compression is used), the range resolution depends on resulting extent of the convolution of the transmit waveform and target response. In our work, the wideband waveform has a slightly better range resolution than the eigenwaveform or rectangular waveform due to its narrow time extent. For eigenwaveform, there is a lower limit of $T_R = 4T$ for matched filtered echoes not to overlap in AF's range (delay) domain. Increasing L increases coherent integration gain while sacrificing sidelobe peak to main peak ratio. Increasing T_R (which translates to

lowering of PRF) increases unambiguous range and its impact on Doppler domain is covered in next section.

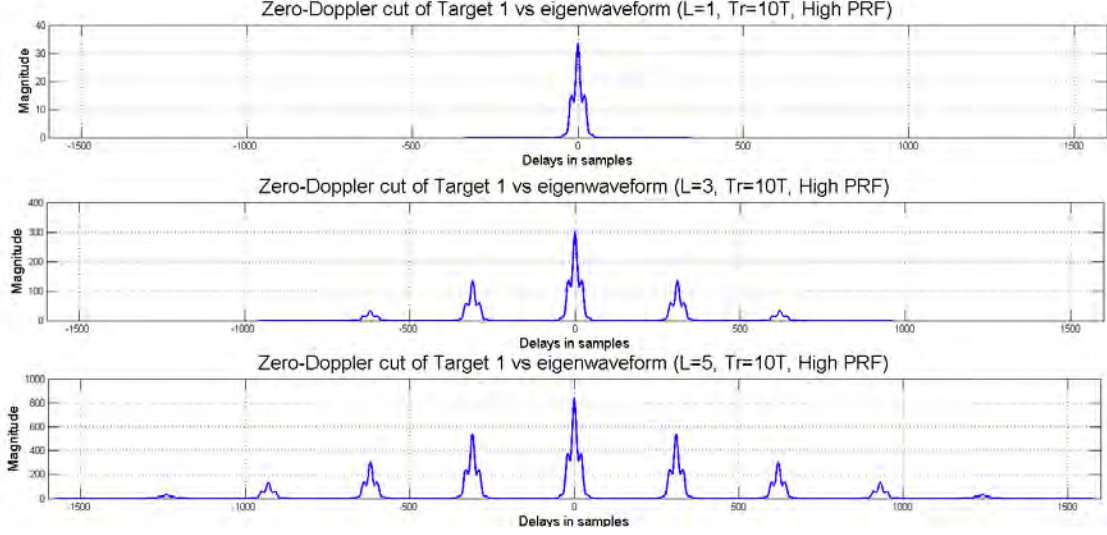


Figure 18. Zero-Doppler cut of Target 1 AF with un-normalized eigenwaveforms and various L . Upper panel: ($L = 1$, high PRF), middle panel: ($L = 3$, high PRF), and lower panel: ($L = 5$, high PRF).

B. ZERO-DELAY CUT

The zero-delay cut shows the AF Doppler spread when the delay is zero. At times, the zero-delay cut offers a perspective that is not quite apparent from an AF contour. From [5] and [12], we realize that the width of the main lobe is decreased (i.e., Doppler resolution improvement) by increasing the number of pulses in a transmission by observing the AF zero-delay cut, which is given by

$$|\chi[0; f_d]|^2 = \left[\frac{1}{L} |\chi_1(0; f_d)| \left| \frac{\sin[\pi f_d L T_R]}{\sin[\pi f_d T_R]} \right| \right]^2. \quad (44)$$

Employing the eigenwaveform, we illustrate in Fig. 19 the AF zero-delay cuts for Target 1 and Target 2 with $L = 1, 3, 5$ using medium PRF with $T_R = 40T$. We include $L = 1$ to remind us the AF ($|\chi[0; f_{dn}]|^2$) corresponding to $L = 1$ serves as the envelope as dictated by (33). For traditional waveforms for point targets, the zero-delay cut is purely a

function of the transmit waveform. From Fig. 19, it is clear that extended target AF zero-delay cuts differ from target to target. Notice that the zero-Doppler cut is the squared multiplication of $L=1$ zero-Doppler cut with a sinc-train. The frequency separation of the sinc-lobes is dictated by $1/T_R$ and the half width of the main lobe is given by

$$BW_L = \frac{1}{LT_R} = f_{d,\rho} \quad (45)$$

which is also considered as the Doppler resolution. However, in (44) notice that the separation of the sinc-lobes is also a function of T_R and L . In other words, Doppler separation (to avoid ambiguity) is also a function of T_R and L . Thus, by varying T_R and L , we can improve (or degrade) Doppler resolution and change the frequency separation of the sinc-lobes. For example, we illustrate in Fig. 20 the eigenwaveform AF zero-delay cuts for Target 1 and Target 2 with $L=1, 3$, and 5 but now using high PRF (smaller T_R). It is clear that the higher PRF (which is lower T_R) has wider separation but poorer resolution since the bandwidth (45) is increased by decreasing T_R . Thus, to maintain the same bandwidth or Doppler resolution in (45) while decreasing T_R (increasing sinc-lobe separation), it is necessary to increase L . In other words, Doppler resolution is dictated by the length of total transmission $T_x = LT_R$ as observed earlier.

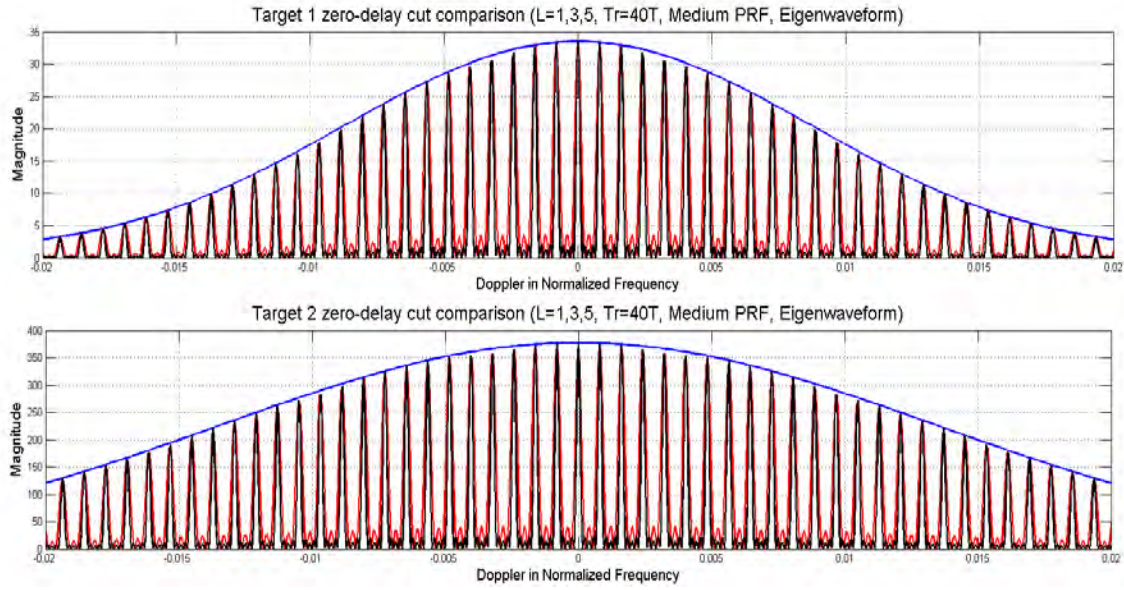


Figure 19. Zero-delay cut comparison with single, three, and five retransmissions with low PRF using the eigenwaveform.

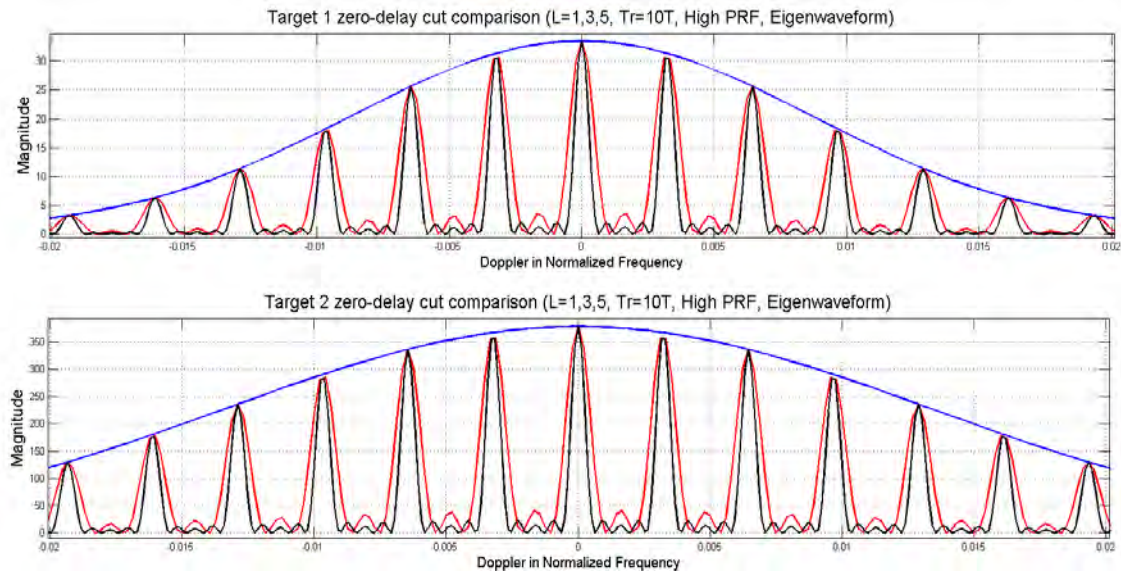


Figure 20. Zero-delay cut comparison with single, three, and five retransmissions with high PRF using the eigenwaveform.

C. RANGE AND DOPPLER RESOLUTION TRADE-OFF

It is now clear there is an inherent trade-off between range and Doppler resolution by varying the PRF (and L) of multiple pulse transmission of eigenwaveforms (or other waveforms for that matter) for extended targets. To illustrate the range and Doppler trade-off that continue to exist even for multiple-pulse waveform for extended targets, we employ a high PRF and a low PRF eigenwaveform on Target 1 and show the corresponding zero-Doppler cuts in Fig. 21a and Fig. 21c, respectively, and zero-delay cuts in Fig. 21b and Fig. 21d with various L given a constant transmit energy constraint and a constant total length constraint (i.e., E_x and LT_R is constant). From Fig. 21a and Fig. 21c, it is clear that the range resolution is the same since the pulse width remains the same; the unambiguous range is worse for the high PRF than low PRF. From Fig. 21b and Fig. 21d, the Doppler resolution is the same since LT_R is constant but the sinc-lobe separation is larger for the high PRF than low PRF.

In summary, range resolution and Doppler resolution depend on the type of transmit waveform and transmit signal length. For multiple pulse eigenwaveforms, increasing PRF (decreasing T_R) results in increasing Doppler sinc-lobes separation but increasing PRF results reducing the unambiguous range. When larger L is used, Doppler resolution may improve but larger L results in more sidelobes, which results in sacrificing sidelobe peak to mainlobe peak ratio. It is a classical trade-off where a specific application dictates the right choice for a system. But we should mention the fact that the narrowband nature of the eigenwaveform (as opposed to the wideband waveform) helps in the reduction of the sinc-lobe peaks.

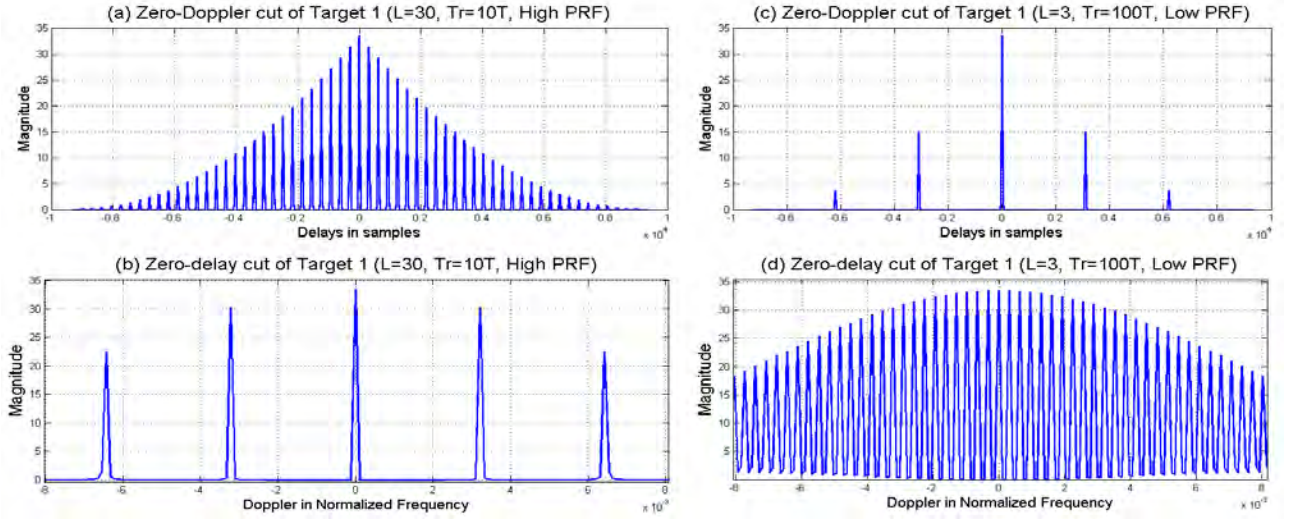


Figure 21. PRF and pulses number comparison with eigenwaveform: (a) zero-Doppler cut ($L = 30$, high PRF), (b) zero-delay cut ($L = 30$, high PRF), (c) zero-Doppler cut ($L = 3$, low PRF), and (d) zero-delay cut ($L = 3$, low PRF).

VI. DETECTION PROBABILITY AND RANGE-DOPPLER MAP

In this section we investigate the probability of detection of various waveforms such eigenwaveform, rectangular waveform and wideband waveform. We can assume the target to have zero Doppler and its extension to the generalized case is straightforward.

A. DETECTION PROBABILITY OF BASIC ONE-PULSE WAVEFORMS

Let \mathbf{h} be the complex-valued target response and \mathbf{w} be the complex valued white Gaussian noise in the receiver with a sample variance of σ^2 . Let \mathbf{s} be the convolution of transmit waveform \mathbf{x} and \mathbf{h} . Then the detection hypotheses are given by

$$\begin{aligned} H_0 : \mathbf{y} &= \mathbf{w} \\ H_1 : \mathbf{y} &= \mathbf{s} + \mathbf{w} = \mathbf{H}\mathbf{x} + \mathbf{w} \end{aligned} \quad (46)$$

where \mathbf{H} is the target convolution matrix corresponding to \mathbf{h} . The decision statistic using matched filter theory for a fixed threshold γ is

$$T(\mathbf{y}) = \text{Re}\{\mathbf{y}^H \mathbf{s}\} = \text{Re}\{\mathbf{y}^H \mathbf{H}\mathbf{x}\}. \quad (47)$$

When the wideband waveform is used, the detection probability [18] given a fixed false alarm probability (PFA) is given by

$$P_D = Q(Q^{-1}(P_{FA}) - \sqrt{\frac{2E_x E_h}{\sigma^2}}) \quad (48)$$

$$= Q(Q^{-1}(P_{FA}) - \sqrt{2E_x \text{TNR}}), \quad (49)$$

where $\text{TNR} = E_h / \sigma^2$ (received target-to-noise ratio) and Q function is the tail probability of the standard normal distribution. Alternatively, (22) can be given as

$$P_D = Q(Q^{-1}(P_{FA}) - \sqrt{2E_h \text{SNR}}), \quad (50)$$

where $\text{SNR} = E_x / \sigma^2$ (transmit signal-to-noise ratio). In other words, P_D is a function of both transmit energy and received target energy along with the noise variance. A more

compact version of (48), which resembles detection probability of traditional matched filter analysis [19] is

$$P_D = Q(Q^{-1}(P_{FA}) - \sqrt{2E_s NR}), \quad (51)$$

where $E_s NR = E_x E_h / \sigma^2$ where E_s specifically means return (echo) energy using the wideband waveform. It can be shown [7] that the detection probability with the use of eigenwaveform is given by

$$\begin{aligned} P_D &= \Pr(T \geq \gamma; H_1) \\ &= Q\left(\frac{\gamma' - E_s}{\sqrt{\frac{\sigma^2 E_s}{2}}}\right) = Q\left(\frac{\gamma' - \lambda_{\max} E_h E_x}{\sqrt{\frac{\sigma^2 \lambda_{\max} E_h E_x}{2}}}\right) \\ &= Q(Q^{-1}(P_{FA}) - \sqrt{\frac{2\lambda_{\max} E_h E_x}{\sigma^2}}) \\ &= Q(Q^{-1}(P_{FA}) - \sqrt{2\lambda_{\max} E_s NR}). \end{aligned} \quad (52)$$

Notice that performance improvement with the use of eigenwaveform compared to the wideband (impulse) waveform given a fixed PFA by comparing (25) and (26) where λ_{\max} effectively amplifies the $E_s NR$ in (51).

For any arbitrary waveform (rectangular waveform included), it can be shown that the generalized detection probability is given by

$$\begin{aligned} P_D &= \Pr(T \geq \gamma'; H_1) \\ &= Q\left(\frac{\gamma' - E_s}{\sqrt{\frac{\sigma^2 E_s}{2}}}\right) = Q\left(Q^{-1}(P_{FA}) - \sqrt{\frac{2E_h E_x \left| \bar{\mathbf{x}}^H \bar{\mathbf{R}}_h \bar{\mathbf{x}} \right|}{\sigma^2}}\right), \end{aligned} \quad (53)$$

where $\bar{\mathbf{x}}$ and $\bar{\mathbf{R}}_h$ are normalized transmit waveform and target response autocorrelation matrix. It is intuitive to conclude that the value of $\left(\bar{\mathbf{x}}^H \bar{\mathbf{R}}_h \bar{\mathbf{x}} \right)$ may vary from close to zero (since $\bar{\mathbf{R}}_h$ is positive definite) to λ_{\max} . As a consequence, the detection performance

pretty much depends on the how good/bad the transmit waveform matches target response's autocorrelation matrix. Thus, if we want to compare detection probabilities of arbitrary waveforms, they have to be calculated via (53) and only then we can tell if it is greater or less than the detection probability of the wideband impulse waveform that is given in (48). In other words, stating what the transmit energy is not enough to know the detection probability of an arbitrary waveform. Its correlation with the target dictates the total return energy. The eigenwaveform ensures the maximum detection probability since the term $\mathbf{x}^H \mathbf{R}_t \mathbf{x}$ inside the square root in (53) is maximized which yields the detection probability in (52). The detection performance curves for various waveforms illuminating Target 1 and Target 2 are shown in Fig. 22 and Fig. 23 given a fixed TNR (target-to-noise energy ratio) for various false alarm probabilities (P_{FA}). Considering Fig. 22, the performance of the eigenwaveform is superior to rectangular and wideband waveforms (given a fixed P_{FA}) as expected. For example, $P_{FA}=0.01$ and $P_D=0.9$, the eigenwaveform advantage over the wideband waveform is about 7.6 dB (which makes sense since this is about equal to $10\log(\lambda_{\max})$). What's more incredible however (for oscillatory Target 1) is that the eigenwaveform with a stringent requirement of $P_{FA}=10^{-4}$ still outperforms both the wideband waveform and the rectangular waveform with a looser requirement of 10^{-2} (for $P_D > 0.1$)! In Fig. 23 where Target 2 is considered, the performance curve for eigenwaveform still is the best compared to rectangular waveform and wideband waveform given a fixed P_{FA} . However, as can be inferred from the ambiguity functions previously studied, the detection performance of the rectangular waveform is much better than the wideband waveform (for the non-oscillatory Target 2). This reinforces the notion that was stated earlier. We know that the eigenwaveform yields the best detection performance but detection performance of other waveforms have to be calculated via (53) such that performance comparison (in terms of detection) between waveforms can be made. Finally, the detection performance comparison adds the needed final dimension to the range-Doppler trade-off when considering various waveforms. In other words, systems which are noise-limited may opt for the eigenwaveform with a slight hit on range resolution. Other systems which may not be noise-limited may opt for other waveforms if

range resolution takes precedence (but with possibly substantial cost in detection performance).

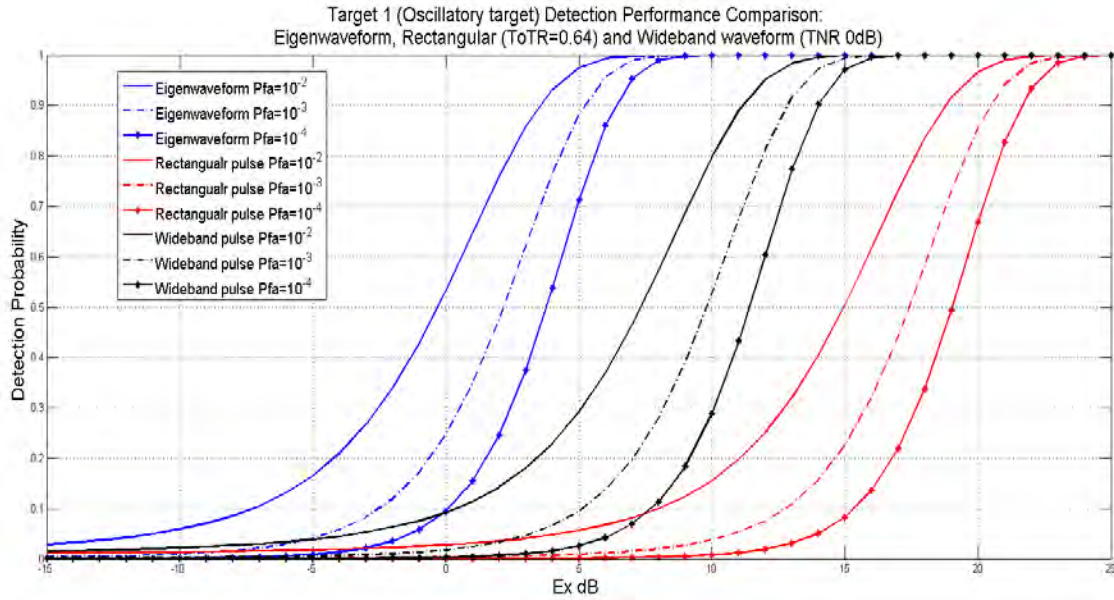


Figure 22. Target 1 detection probability comparison of wideband waveform, rectangular waveform (ToTR = 0.64) and eigenwaveform (TNR = 0dB).

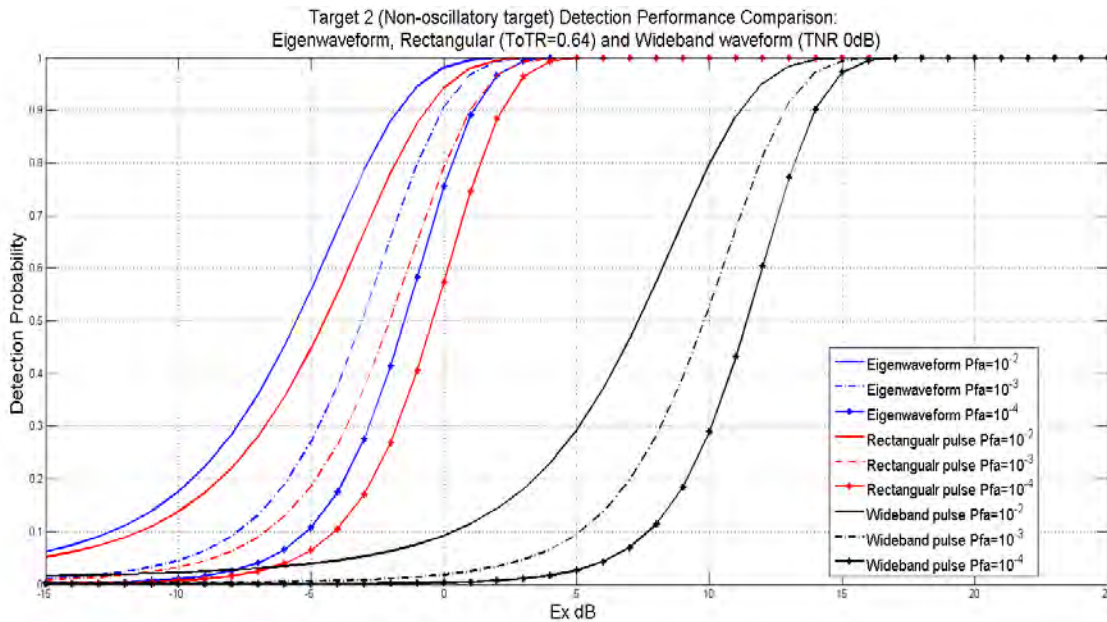


Figure 23. Target 2 detection probability comparison of wideband waveform, rectangular waveform (ToTR = 0.64) and eigenwaveform (TNR = 0dB).

B. DETECTION PROBABILITY OF COHERENT MULTIPLE-PULSE TRANSMISSION AND RANGE DOPPLER MAP APPLICATION

When moving targets are present, one of the ambiguity function application is the range-Doppler map (RDM) which significantly demonstrates the benefit of using eigenwaveform for extended targets. Assume L pulses are sent and that the return echo is received. Any target detected may be moving such that a Doppler component is possible. After receiving the return, the long sequence is carefully re-arranged so that each return from every pulse is aligned according to same delay and stored in a measurement matrix. By taking fast-Fourier transform (FFT) in Doppler direction, signal energy converges into corresponding Doppler bins (indices) due to FFT's circular shift property. The magnitude of the measurement matrix after the FFT operation is considered the range Doppler map since it reveals the characteristic of moving target's delay (which corresponds to range) and Doppler shift (which corresponds to velocity). The multiple-pulse wideband waveform, rectangular waveform, and eigenwaveform are utilized as the transmit waveforms here. A peak value may be used to detect a target's position (delay) and Doppler spread. Of course, the RDM can detect multiple targets with different speeds and distances and ambiguities can be avoided via discussion from earlier sections.

Moreover, when multiple pulses are used, it can be shown that the detection probability is also a function of the number pulses (L). The detection probability with L pulses with the use of eigenwaveform is be shown to be

$$\begin{aligned} P_d &= \Pr(T \geq \gamma'; H_1) \\ &= Q\left(\frac{\gamma' - E_s}{\sqrt{\frac{\sigma^2 E_s}{2}}}\right) = Q\left(\frac{\gamma' - \lambda_{\max} L E_h E_x}{\sqrt{\frac{\sigma^2 \lambda_{\max} E_h E_x}{2}}}\right) = Q\left(Q^{-1}(P_{FA}) - \sqrt{\frac{2\lambda_{\max} L E_h E_x}{\sigma^2}}\right). \end{aligned} \quad (54)$$

The gain due to L ($10 \log L$ in dB) is also true for other waveforms as shown in Fig. 24. In Fig. 24, we illustrate the Target 1 detection performance curves for the three waveforms as a function of increasing L . As expected, increasing L increases detection probability.

Now, we generate the RDM (3-D maps) where we utilize Target 1 and illuminate it with the wideband, rectangular ($\text{ToTR} = 0.64$), and eigenwaveform (duty cycle $d_t = 10^{-3}$) where $L = 31$ as a function of increasing SNR (0, 3, 10 dB) given a fixed TNR = 0 dB. We illustrate in Fig. 25 the 3-D RDMs of these various waveforms as a function of increasing E_sNR (return energy to noise ratio). In this scenario, the target is located at range (delay) = 560 with normalized Doppler of $f_d = 0.0968$. Notice that the target is not very visible for SNR = 0 dB with the use of rectangular waveform. For the same SNR, there is a small peak corresponding to Target 1 with the use of the wideband waveform. Notice however that the Target 1 is clearly discernable with SNR=0 dB when the eigenwaveform is used. Increasing SNR enhances the peaks for all waveforms with the eigenwaveform clearly yielding the largest peak.

RDMs are usually presented as 2-D maps (magnitude or squared-magnitude). In this scenario, we place two targets (Target 1 type) in two different range-Doppler bins. Again we use the wideband, rectangular ($\text{ToTR} = 0.64$), and eigenwaveform ($d_t = 10^{-3}$) where $L = 31$ as a function of increasing SNR (0, 3, 10 dB) given a fixed TNR = 0dB. The RDMs are illustrated in Fig. 26. In this scenario, the targets are located at range (delay) = 450 with normalized Doppler of ($f_{d1} = 0.1613$) and range (delay) = 750 with normalized Doppler of ($f_{d2} = -0.1290$). Again, notice that the targets are not very discernable for SNR = 0 dB with the use of rectangular waveform. For the same SNR, there is a some faint possibility that one of the targets maybe detected with the use wideband waveform. Both targets are clearly pronounced when the eigenwaveform is used even with SNR = 0 dB. Increasing SNR enhances the target bins in the RDMs for all waveforms with the eigenwaveform clearly yielding the brightest target bins.

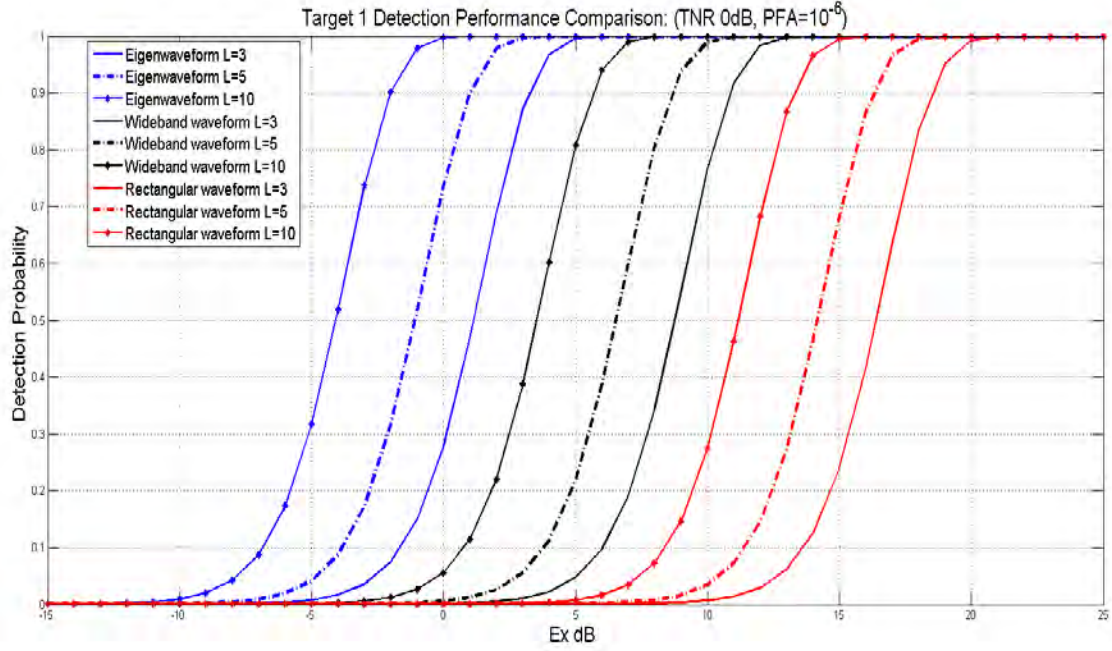


Figure 24. Performance comparison: wideband waveform, rectangular waveform and eigenwaveform with various multiple-pulses transmission ($L = 3, 5, 10$).

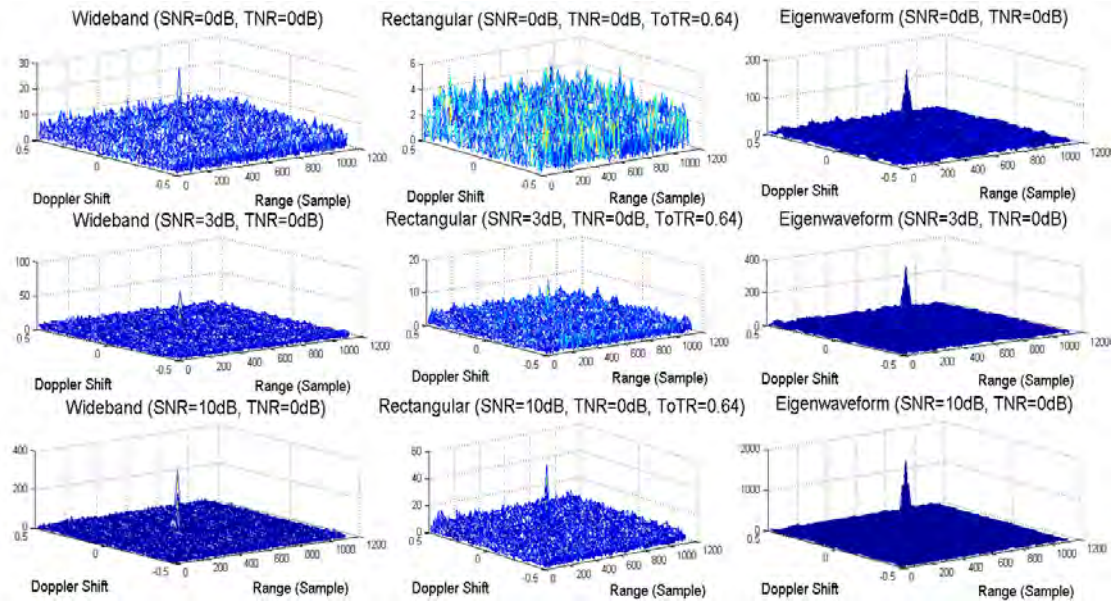


Figure 25. Target 1 3-D view RDM comparison for SNR = (0 dB, 3 dB, 10 dB), and TNR = 0 dB. The target is located at range (delay) = 560 with Doppler shift of $f_d = 0.0968$. Left panels: wideband waveform, middle panels: rectangular waveform, and right panels: eigenwaveform.

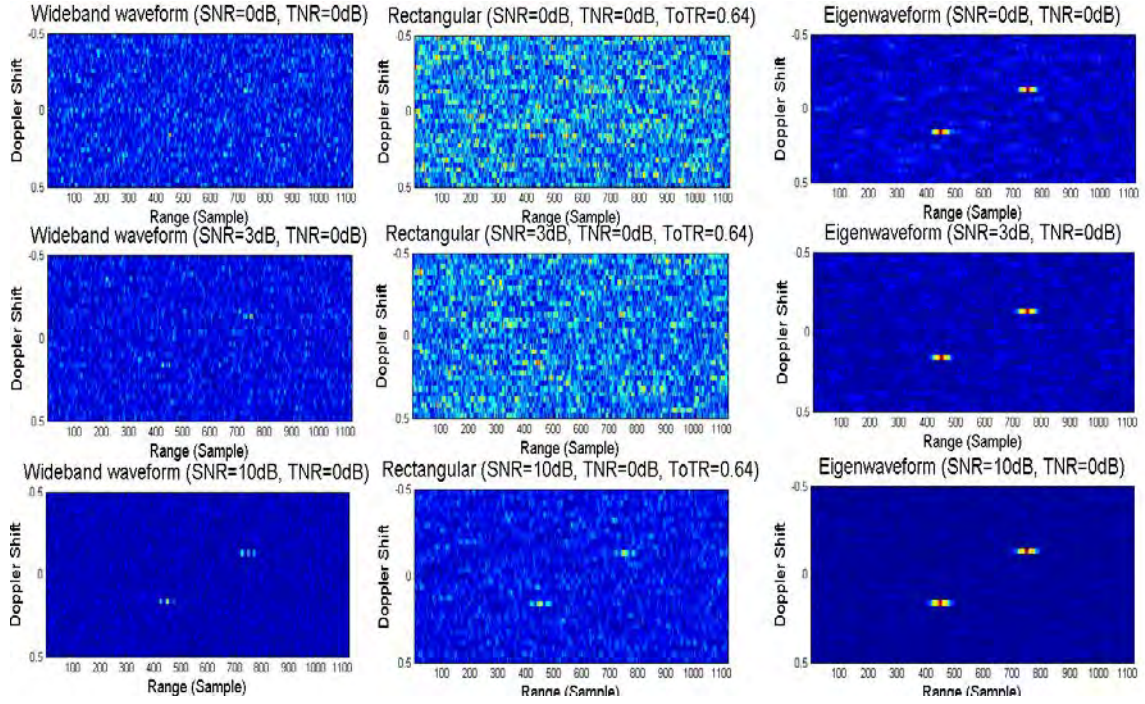


Figure 26. Target 1 RDM comparison for SNR = (0 dB, 3 dB, 10 dB), and TNR = 0 dB. The targets are located at range (delay) = 450 with Doppler shift of $f_{d1} = 0.1613$ and range (delay) = 750 with Doppler shift of $f_{d2} = 0.1290$. Left panels: wideband waveform, middle panels: rectangular waveform, and right panels: eigenwaveform.

VII. PROBABILITY WEIGHTED EIGENWAVEFORMS (PWE) FOR TARGET RECOGNITION

A closed-loop radar which uses adaptive waveforms is used in [2, 8] for target recognition. Among these waveforms, the PWE scheme introduced in [1] has shown the best promise as far as classification performance as well as low mean number of transmissions. Here we investigate maximum a posteriori PWE (MAP-PWE). Based on the decision statistics, we propose an improved un-biased version called match-filtered PWE (MF-PWE). Moreover, we also propose two-stage PWE (TS-PWE) which is based on likelihood and waveform weighting that effectively works well in low SNR. We describe the closed-loop radar operation involving these waveforms and summarize the radar operational steps in a flow diagram. We perform Monte Carlo simulations to show the identification performance comparisons.

A. ADAPTIVE WAVEFORMS, LIKELIHOOD UPDATES, AND COGNITIVE RADAR PLATFORM INTRODUCTION

What makes a radar closed-loop is the use of probability or likelihood updates into forming adaptive waveforms. Here we consider the use of closed loop or cognitive radar platform for target recognition which had been extensively used in [1, 2, and 8]. Since the notion of adaptive waveforms, probability/likelihood updates and waveform weighting are so integrated in the closed-loop radar, we will introduce our first adaptive waveform MAP-PWE and the cognitive radar operations simultaneously in the following section.

1. MAP-PWE

Consider a target identification problem in which one of M possible targets is present. Each target hypothesis is characterized by its impulse response $\mathbf{h}_j, j = 1, 2, \dots, M$ which are assumed a priori.

Assuming all targets are of length n and assuming there is one target present, the detection hypotheses are

$$\begin{aligned}
H_1 : \mathbf{y} &= \mathbf{x} * \mathbf{h}_1 + \mathbf{w} = \mathbf{H}_1 \mathbf{x} + \mathbf{w} \\
H_2 : \mathbf{y} &= \mathbf{x} * \mathbf{h}_2 + \mathbf{w} = \mathbf{H}_2 \mathbf{x} + \mathbf{w} \\
&\dots \\
H_M : \mathbf{y} &= \mathbf{x} * \mathbf{h}_M + \mathbf{w} = \mathbf{H}_M \mathbf{x} + \mathbf{w}
\end{aligned} \tag{55}$$

where the \mathbf{H}_j is the $2n$ -by- n convolution matrix of target j and \mathbf{w} is the complex-valued AWGN vector with a sample variance of σ^2 . The correlation matrix of \mathbf{w} is simply $\sigma^2 \mathbf{I}$ and we assume σ to be one for simplicity. Each time the radar transmits a waveform \mathbf{x} , a noise-corrupted version of the reflected target echo is received as \mathbf{y} .

In PWE, the transmit signal is the linear combination of each unit energy eigenvector \mathbf{q}_j each weighted by $\sqrt{w_j}$ where w_j is the weight distribution for the j^{th} hypothesis calculated from prior received signal. The energy constraint of transmit signal E_x in the end actually dictates the energy weight distribution of each eigenwaveform. However, to simplify the procedure it is best to simply add the weights to sum up to 1 (as an intermediate normalization step). In other words,

$$\sum_{j=1}^M w_j = 1, \tag{56}$$

and

$$\bar{\mathbf{x}} = \left(\sum_{j=1}^M \sqrt{w_j} \mathbf{q}_j \right), \tag{57}$$

where $\bar{\mathbf{x}}$ is the direct combination result of all eigenvector \mathbf{q}_j . However, $\bar{\mathbf{x}}$ may not be unit-energy after summation since the eigenwaveforms themselves come from different targets and may not be orthogonal. Although the energy may be close to 1, it still needs to be normalized such that the energy constraint can easily be factored in i.e.,

$$\mathbf{x} = \sqrt{E_x} \frac{\bar{\mathbf{x}}}{\sqrt{E_{\bar{\mathbf{x}}}}}, \tag{58}$$

where E_x is the energy of transmit signal and $E_{\bar{\mathbf{x}}}$ is the energy of $\bar{\mathbf{x}}$ in (57).

Now, we discuss how the waveform weights are calculated. Let $f_{ji}(\mathbf{y})$ be the probability density or likelihood function of the j^{th} hypothesis given i^{th} target is the present target assuming additive white Gaussian noise. Recalling $\sigma = 1$ for convenience, the probability density or likelihood function is given by

$$\begin{aligned} f_{ji}(\mathbf{y}) &= \beta \exp[-(\mathbf{y} - \mathbf{s}_j)^H (\mathbf{y} - \mathbf{s}_j)] \\ &= \beta \exp[-\mathbf{y}^H \mathbf{y} + \mathbf{s}_j^H \mathbf{y} + \mathbf{y}^H \mathbf{s}_j - \mathbf{s}_j^H \mathbf{s}_j] \\ &= \beta \exp[-\mathbf{y}^H \mathbf{y} + 2 \operatorname{Re}(\mathbf{s}_j^H \mathbf{y}) - \mathbf{s}_j^H \mathbf{s}_j], \end{aligned} \quad (59)$$

where

$$\beta = \frac{1}{\pi^n} \quad (60)$$

is the constant in front of the Gaussian distribution.

Let w_j^1 be the initial waveform weight for each hypothesis as dictated by (57). If there is no a priori information available as to the likelihood of each hypothesis, then initially we can assume them to be equally likely i.e., $w_j^1 = 1/M$. Let $f_j^P(\mathbf{y})$ be the likelihood function from P^{th} return signal, then the waveform weights w_j^{P+1} are updated by the likelihood values from the latest P^{th} return signal. In other words, for multiple illumination the waveform weights are updated as:

$$\begin{aligned} w_i^1 &= \frac{1}{M} \\ w_i^2 &= \alpha^1 w_i^1 f_i^1 \\ w_i^3 &= \alpha^2 w_i^2 f_i^2 \\ &\dots \\ w_i^{P+1} &= \alpha^P w_i^P f_i^P, \end{aligned} \quad (61)$$

where f_j^P is the calculated likelihood value after P^{th} transmission and the weight w_j^{P+1} is the weight distribution corresponding to the j^{th} hypothesis for the $(P+1)^{th}$ transmission (or P updates) while α^P ensures unity weight summation as dictated by (56) in each transmission. In other words, w_j^{P+1} is the waveform weight of j^{th} eigenwaveform in (57).

It can be shown that by substituting $\mathbf{y} = \mathbf{H}_i \mathbf{x} + \mathbf{w}$ and $\mathbf{s}_j = \mathbf{H}_j \mathbf{x}$ into (59), the generalized formula of the likelihood function for j^{th} hypothesis given i^{th} target is

$$f_{ji}(\mathbf{x}) = \beta \exp[-\mathbf{x}^H \mathbf{H}_i^H \mathbf{H}_i \mathbf{x} - \mathbf{x}^H \mathbf{H}_i^H \mathbf{w} - \mathbf{w}^H \mathbf{H}_i \mathbf{x} - \mathbf{w}^H \mathbf{w} + 2 \operatorname{Re}(\mathbf{x}^H \mathbf{H}_j^H \mathbf{H}_i \mathbf{x} + \mathbf{x}^H \mathbf{H}_j^H \mathbf{w}) - \mathbf{x}^H \mathbf{H}_j^H \mathbf{H}_j \mathbf{x}], \quad (62)$$

and the first moment (mean) of incorrect hypotheses (where $i \neq j$) is

$$E[f_{ji}(\mathbf{x})] = \beta \exp[\eta + 2 \operatorname{Re}(\mathbf{x}^H \mathbf{H}_j^H \mathbf{H}_i \mathbf{x}) - \mathbf{x}^H \mathbf{R}_j \mathbf{x}], \quad (63)$$

where \mathbf{R}_j is the discrete autocorrelation function corresponding to j^{th} hypothesis and η is defined as

$$\eta = -\mathbf{x}^H \mathbf{H}_i^H \mathbf{H}_i \mathbf{x} - E[\mathbf{w}^H \mathbf{w}], \quad (64)$$

which is a constant term for all hypotheses.

On the other hand, the first moment (mean) of correct hypothesis where $i = j$ becomes

$$\begin{aligned} E[f_{ii}(\mathbf{x})] &= \beta \exp[\eta + 2 \operatorname{Re}(\mathbf{x}^H \mathbf{H}_i^H \mathbf{H}_i \mathbf{x}) - \mathbf{x}^H \mathbf{H}_i^H \mathbf{H}_i \mathbf{x}] \\ &= \beta \exp[\eta + 2 \operatorname{Re}(\mathbf{x}^H \mathbf{R}_i \mathbf{x}) - \mathbf{x}^H \mathbf{R}_i \mathbf{x}]. \end{aligned} \quad (65)$$

It is clear from (65) that the argument inside the exponential of the correct hypothesis ($i = j$) is greater than all incorrect hypotheses in (63) since the second term in (65) is a fully-correlated match (autocorrelation matrix $\mathbf{H}_i^H \mathbf{H}_i$) while (63) involves cross-target correlation which is clearly drives it to a lower value. Thus, the likelihood of correct hypothesis has higher value which leads to higher weight of w_i in next waveform formation in (61). Here we use w_i since $j = i$ for the correct hypothesis. Therefore, the waveform weight updating procedure leads to likely identification until a desired probability threshold is met or at the end of desired number of transmissions. This is how the MAP-PWE cognitively approaches the correct hypothesis during its operation.

MAP-PWE has been shown to be a very effective adaptive waveform formation scheme for non-moving target identification in this closed-loop radar platform. However, when comparing (63) and (65), the last terms cause undesirable effect of subtracting a higher value in the correct hypothesis than in the incorrect hypotheses. To illustrate this effect, consider the case when the updating procedure finally homes in on the target present (after a few iterations). In other words, when $w_i \approx 1$ and $\mathbf{x} \approx \mathbf{q}_{\max,i}$, the last term of incorrect j^{th} hypothesis in (63) is an insignificant value since $\mathbf{x} = \mathbf{q}_{\max,i}$ is not highly correlated to any target j while correct i^{th} hypothesis subtracts a maximum value of $\lambda_{\max,i} E_x$. The biased subtraction of this term in the most likely hypothesis affects the identification performance.

To illustrate the biased effect in MAP-PWE, consider the noise only scenario where $\mathbf{y} = \mathbf{w}$ and $\mathbf{s}_j = \mathbf{H}_j \mathbf{x}$. It can be shown from (59) that the first moment of likelihood function for all hypotheses $f_j(\mathbf{x})$ is

$$E[f_j(\mathbf{y})] = \beta \exp[-E[\mathbf{w}^H \mathbf{w}] - \mathbf{x}^H \mathbf{H}_j^H \mathbf{H}_j \mathbf{x}] = \beta \exp[-E[\mathbf{w}^H \mathbf{w}] - \mathbf{x}^H \mathbf{R}_j \mathbf{x}]. \quad (66)$$

Since \mathbf{x} is the combination of all eigenwaveforms with different weight $\sqrt{w_j}$, we can further derive (66) in terms of eigenvalues and waveform weights, that is

$$E[f_j(\mathbf{y})] = \beta \exp[-E[\mathbf{w}^H \mathbf{w}] - \frac{E_x}{E_{\bar{x}}} (\sum_{j=1}^M \sqrt{w_j} \mathbf{q}_j)^H \mathbf{R}_j (\sum_{j=1}^M \sqrt{w_j} \mathbf{q}_j)]. \quad (67)$$

Due to the fully-correlated match (autocorrelation \mathbf{R}_j) inside the argument of the exponential and after a few iterations, the waveform weight updating procedure approaches the j^{th} target hypothesis of higher eigenvalue λ_j . The j^{th} maximum eigenvector \mathbf{q}_j dominates the $f_j(\mathbf{x})$, that is

$$\begin{aligned} E[f_j(\mathbf{y})] &\cong \beta \exp[-E[\mathbf{w}^H \mathbf{w}] - \frac{E_x}{E_{\bar{x}}} w_j \mathbf{q}_j^H \mathbf{R}_j \mathbf{q}_j] \\ &= \beta \exp[-E[\mathbf{w}^H \mathbf{w}] - \frac{E_x}{E_{\bar{x}}} w_j \mathbf{q}_j^H \lambda_j \mathbf{q}_j] = \beta \exp[-E[\mathbf{w}^H \mathbf{w}] - \frac{E_x}{E_{\bar{x}}} w_j \lambda_j]. \end{aligned} \quad (68)$$

Since the mean in (68) is different for each hypothesis, the waveform weights dictated by (61) and (68) will have unequal weights after each update. For the noise-only case scenario that we are currently discussing, no eigenwaveform should be favored since a target is not present. Thus, the probability weight updating procedure under noise only scenario is biased (a function of target response matrix's eigenvalue) and the identification performance when a target is truly present suffers from the various eigenvalues in (68). In fact, the biasing effect becomes worse when energy of \mathbf{x} increases (i.e., when the transmit energy of the PWE waveform is increased). To illustrate this point, we perform Monte Carlo (MC) trials where there are four target hypotheses where we assume initial probability of 0.25 for each hypothesis but under the noise only scenario. Since there is not a target present, we only receive noise in the measured signal and calculate the 4 likelihood and waveform weights. We perform 10000 MC trials in which to average over. In Fig. 27a, we show the waveform weight updates as a function of increasing transmission energy using MAP-PWE. At low transmit energy, the average updated waveform weight remains at 0.25 which is obviously desired. Notice however that as transmission energy is increased, the updated weights diverge where one hypothesis seems to be favored than others (which is clearly unwanted).

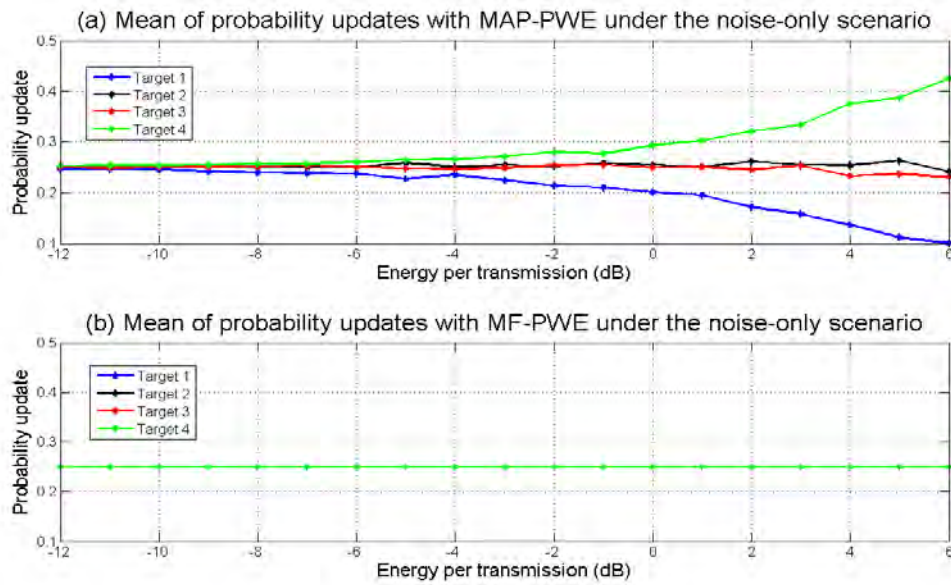


Figure 27. Mean of target probability updates versus transmission energy under noise only scenario assuming unity noise energy. (a)MAP-PWE. (b)MF-PWE.

2. MF-PWE

It is our desire to improve MAP-PWE. Clearly, one way is to remove the unnecessary bias terms in the likelihood functions. In reality, removing bias terms lead to a receiver configuration that is equivalent to using a bank of matched filters. Removing the constant terms in (59) lead to a modified likelihood function given by

$$f_{ji}(\mathbf{y}) = \beta \exp[2 \operatorname{Re}(\mathbf{s}_j^H \mathbf{y})], \quad (69)$$

where β now here is a constant that ensures the waveform weights sum up to 1 as dictated by (56). By substituting $\mathbf{y} = \mathbf{H}_i \mathbf{x} + \mathbf{w}$ and $\mathbf{s}_j = \mathbf{H}_j \mathbf{x}$ into (69) where it is clear why the current technique is to be called matched-filter PWE (MF-PWE), (69) becomes

$$f_{ji}(\mathbf{y}) = \beta \exp[2 \operatorname{Re}(\mathbf{x}^H \mathbf{H}_j^H \mathbf{H}_i \mathbf{x} + \mathbf{x}^H \mathbf{H}_j^H \mathbf{w})].$$

It can be shown the mean of likelihood for the incorrect hypotheses given i^{th} target is given by

$$E[f_{ji}(\mathbf{y})] = \beta \exp[2 \operatorname{Re}(\mathbf{s}^H \mathbf{y})] = \beta \exp\left[\frac{2E_x}{E_x} \operatorname{Re}\left\{\left(\sum_{j=1}^M w_j \mathbf{q}_j\right)^H \mathbf{H}_j^H \mathbf{H}_i \left(\sum_{j=1}^M w_j \mathbf{q}_j\right)\right\}\right], \quad (70)$$

and the mean of the likelihood for the correct hypothesis probability ($j = i$) is

$$E[f_{ii}(\mathbf{y})] = \beta \exp[2 \operatorname{Re}(\mathbf{s}^H \mathbf{y})] = \beta \exp\left[\frac{2E_x}{E_x} \operatorname{Re}\left\{\left(\sum_{j=1}^M w_j \mathbf{q}_j\right)^H \mathbf{R}_i \left(\sum_{j=1}^M w_j \mathbf{q}_j\right)\right\}\right]. \quad (71)$$

Notice that from (71) that the argument of the exponential of correct hypothesis ($i = j$) is ensured to be greater than all incorrect hypotheses in (70) since the fully-correlated match term in (71) surpasses the cross-target correlation matrix $\mathbf{H}_j^H \mathbf{H}_i$ in (70). Thus, the higher value of likelihood for the correct hypothesis leads to higher waveform weight towards the correct target.

Moreover, after few updates, when the weight is mainly distributed to the eigenwaveform corresponding to the correct hypothesis, the expression in (71) is dominated by

$$E[f_{ji}(\mathbf{y})] \approx \beta \exp\left[\frac{2E_x}{E_{\bar{x}}}(\mathbf{q}_i^H \mathbf{R}_i \mathbf{q}_i)\right] = \beta \exp\left[\frac{2E_x}{E_{\bar{x}}} w_i \lambda_i\right], \quad (72)$$

and the means of the likelihoods of the incorrect hypotheses are given by

$$E[f_{ji}(\mathbf{y})] = \beta \exp[2 \operatorname{Re}(\mathbf{s}^H \mathbf{y})] \approx \beta \exp\left[\frac{2E_x}{E_{\bar{x}}} \operatorname{Re}\{\mathbf{q}_i^H \mathbf{H}_j^H \mathbf{H}_i \mathbf{q}_i\}\right],$$

which leads to a much smaller value than (72).

We now compare MAP-PWE and MF-PWE under noise-only scenario. The modified likelihood $f_j(\mathbf{y})$ is

$$f_j(\mathbf{y}) = \beta \exp[2 \operatorname{Re}(\mathbf{s}_j^H \mathbf{y})] = \beta \exp[2 \operatorname{Re}(\mathbf{x}^H \mathbf{H}_j^H \mathbf{w})] \quad (73)$$

and the mean is

$$E[f_j(\mathbf{y})] = \beta \exp[2 \operatorname{Re}(\mathbf{x}^H \mathbf{H}_j^H E[\mathbf{w}])] = \beta. \quad (74)$$

Clearly, the means of the likelihood functions are the same under the noise-only scenario. Since we sum up the likelihoods and normalize to 1 to produce the waveform weights, each eigenwaveform will have equal weights i.e., no target is favored when a target is not present.

Lastly, the waveform weight update rule remains the same, i.e.,

$$\begin{aligned} w_i^1 &= \frac{1}{M} \\ w_i^2 &= \alpha^1 w_i^1 f_i^1 \\ w_i^3 &= \alpha^2 w_i^2 f_i^2 \\ &\dots \\ w_i^{P+1} &= \alpha^P w_i^P f_i^P \end{aligned} \quad (75)$$

where f_i^P is the calculated likelihood weight corresponding to the i^{th} hypothesis for the P^{th} transmission while α^P ensures unity weight summation in each transmission.

Comparing (68) with (74) for noise-only scenario, it is obvious that MF-PWE provides constant means for all hypotheses no matter how large the eigenvalues are. Thus, the MF-PWE is an unbiased target identification scheme for extended targets

where only the correct target can make significant likelihood increase without the degrading bias terms. Also, MF-PWE reduces the complexity of calculation used by MAP-PWE by simply using the matched filter bank in (69).

The performance comparison of MAP-PWE and MF-PWE vs various transmission numbers are shown in Fig. 28 and Fig. 29 via 10^7 Monte Carlo experiments where one true target is present from four hypotheses. When the number of transmissions is fixed, the hypothesis with the largest updated likelihood is decided to be the correct hypothesis (whether true or not). It is clear in Fig. 28 that MF-PWE has the better identification performance than MAP-PWE for various numbers of fixed transmissions. It is also clear in Fig. 29 that MF-PWE has lower required mean number of transmissions to reach a desired probability threshold (for Fig. 29 the threshold is set as 0.95). In conclusion, MF-PWE performs better than MAP-PWE and wideband waveform as a CR adaptive waveform in terms of target identification and required number of transmissions.

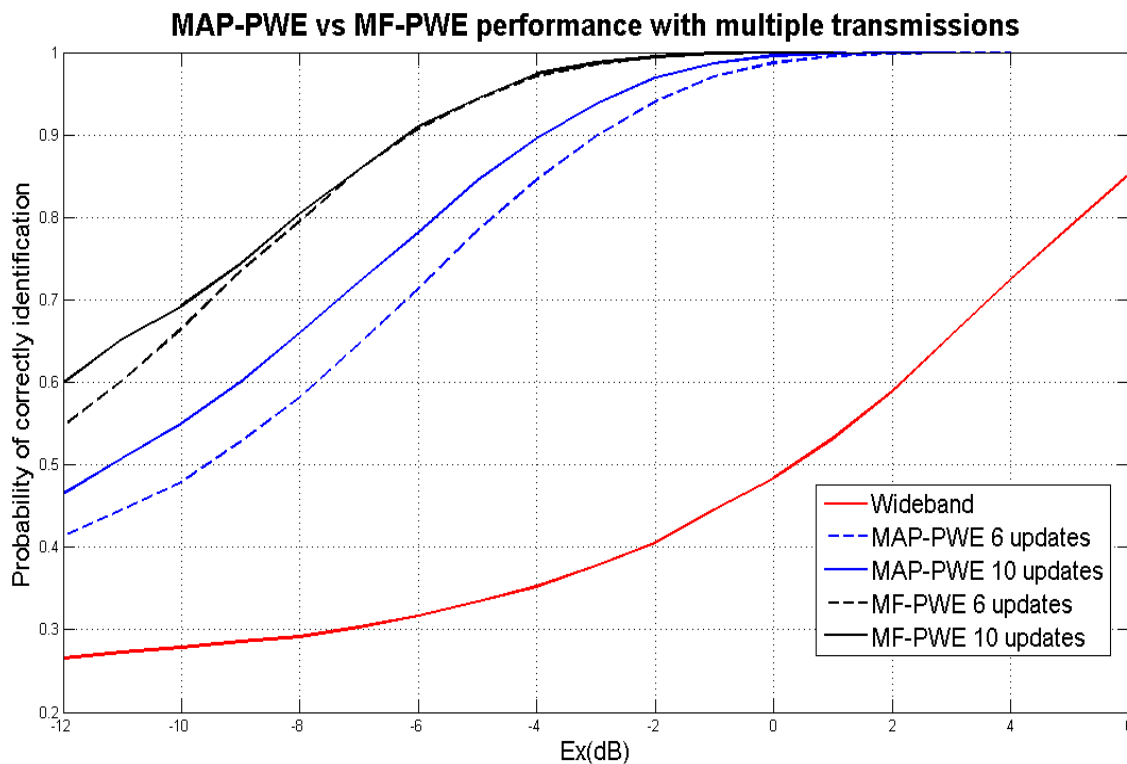


Figure 28. Performance comparison: MAP-PWE and MF-PWE with multiple transmissions assuming unity noise energy.

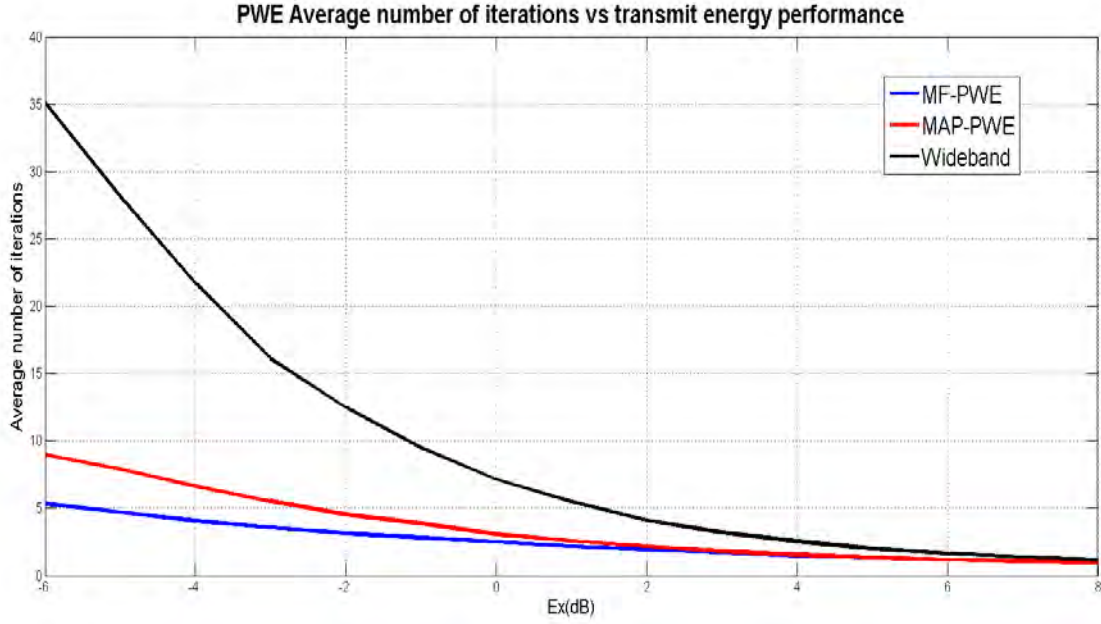


Figure 29. Average or mean number of transmit (probability threshold = 0.95) comparison assuming unity noise energy.

B. TWO-STAGE PWE FOR LOW SNR

The MAP-PWE and MF-PWE closed-loop radar adaptive waveform techniques operates on the previous likelihood and latest likelihood update which is primarily based on Bayes' theorem. We propose a new update process that uses the ratio of the latest calculated likelihood to the previous-to-last calculated likelihood. In low SNR, the noise realizations are large (compared to actual target return) which may cause an incorrect hypothesis to have a large likelihood update. When an incorrect hypothesis takes on a large likelihood update, it is hard to reduce the next waveform weight since the previous update is incorporated into the actual waveform weight. In other words, if a receiver were to stop to make a decision and the incorrect hypothesis happens to have the largest likelihood, then the receiver will choose that incorrect hypothesis. The key idea is to mitigate large swings on the likelihood updates (in the case of low SNRs) where large noise realizations produce volatility to the waveform weights (which can nullify the beneficial improvements of multiple transmissions).

In this section, we propose a heuristic two-stage PWE method (TS-PWE) which is specifically designed to improve the classification performance over the MAP-PWE and MF-PWE in low SNR by using the previous-to-last and latest likelihood ratios in a specific way. To describe the waveform technique, let us briefly go back the closed-loop radar system that we have been using and see how the two-stage PWE is incorporated. The steps are:

1. Assuming M possible extended targets, generate the normalized eigenwaveform for each target hypothesis. Scale each eigenwaveform with the square-root of the initial waveform weight assigned to each hypothesis and then form the first PWE-based waveform.

2. After illumination and reception of target return, calculate the likelihood according to (69). If this is the first transmission, then calculate the second set of waveform weights via the w_i^2 in (75). Our goal is to use the latest and previous weight pairs to generate the next set of waveform weights for the next transmission.

3. For the second and all the rest transmissions, upon the reception of target return, pick the hypothesis with the highest weight (from the latest or last weight set) and calculate the ratio of weight change of this very hypothesis as given by

$$r_1 = \frac{w^{(p)}}{w^{(p-1)}}$$

where p denotes the latest weight and $p-1$ denotes the weight previous to last.

4. Pick the latest and $p-1$ (previous-to-last) likelihoods from the same hypothesis and calculate the likelihood ratio as given by:

$$r_2 = \frac{f^{(p)}}{f^{(p-1)}}$$

where f is from (69).

5. Multiply the latest $f^{(p)}$ by the corrective coefficient which is the ratio of r_2 over r_1 to form the tempered or modified likelihood as given by

$$\overline{f^{(p)}} = f^{(p)} \frac{r_2}{r_1}.$$

6. Calculate the new weight using (61) with the modified likelihood. Since the weights sum up to 1, the weights of the other eigenwaveforms corresponding to other hypotheses set are automatically updated. In other words, the excess weight from the hypothesis with the largest (last) likelihood is re-distributed to the other hypotheses.

The key idea in improving PWE waveform in low SNR is to use the previous and latest weights of the hypothesis with the largest current likelihood update in forming the next waveform weights. The result is the tempering of the updates which swing dynamically due to large noise realizations. The performance gain of this technique in low SNR over MAP-PWE and MF-PWE are significant. The flow diagram of the TS-PWE procedure is summarized in Fig. 30.

Again, we set up a Monte Carlo target recognition experiment using various PWE waveforms. In Fig. 31, mean number of illuminations performance vs transmit energy is shown for various waveforms. It is interesting to note that the TS-PWE is better than other waveforms in low transmit energy (less than -8 dB). In Fig. 32, we show the identification performance results of the MC experiment as a function of transmit energy while varying the number of transmissions (or updates). Since MF-PWE and TS-PWE in Fig. 31, we utilize these two in Fig. 32. Notice that TS-PWE outperforms MF-PWE.

Flow diagram/procedural steps for the TS-PWE

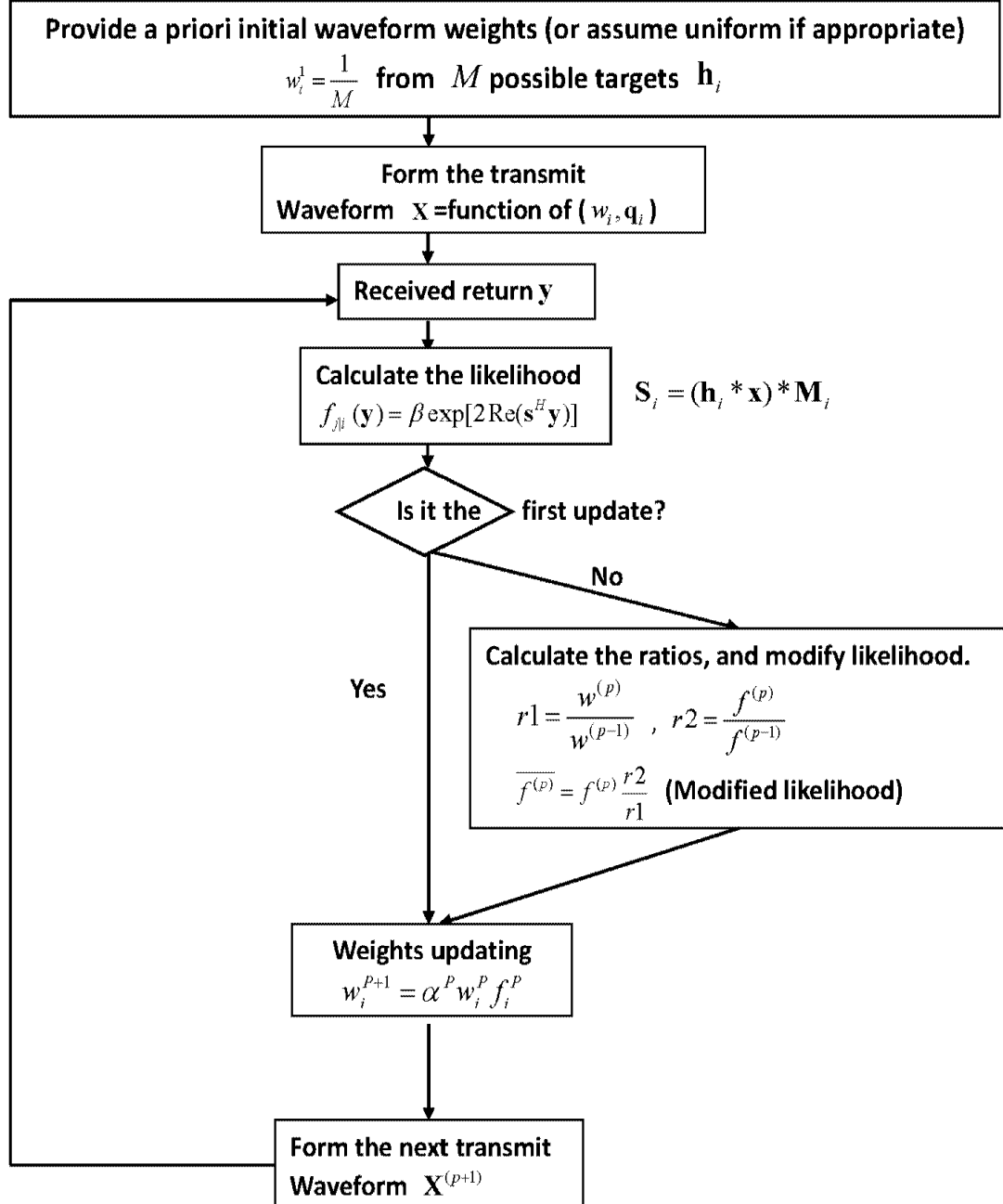


Figure 30. Operational flow diagram for the TS-PWE scheme with a closed-loop radar.

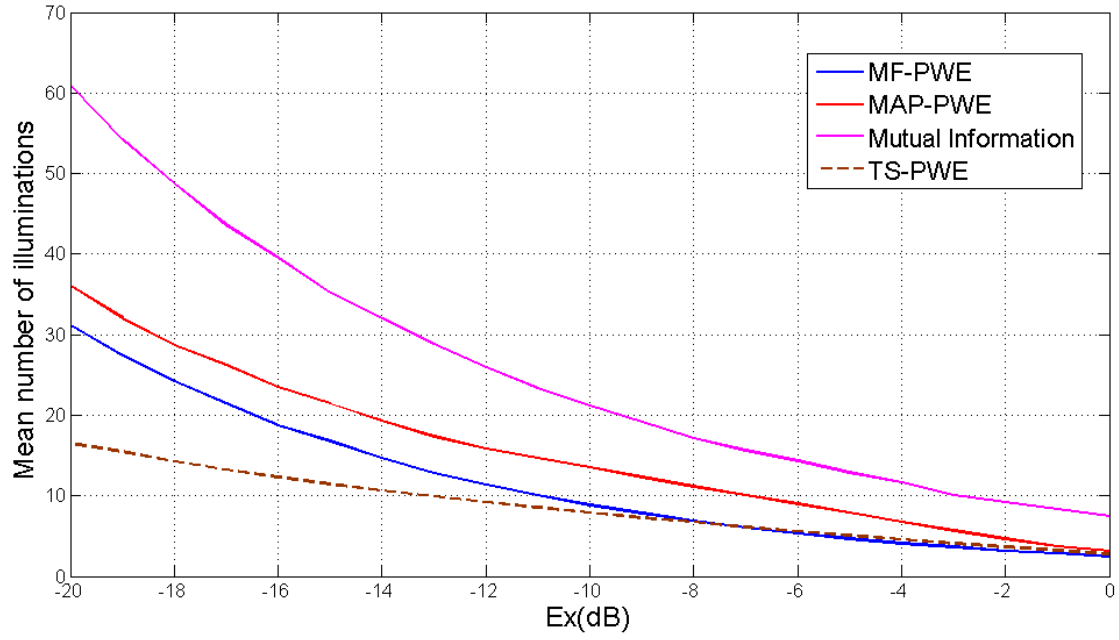


Figure 31. Mean number of illuminations as a function of (received) transmit energy for various adaptive waveforms assuming unity noise energy.

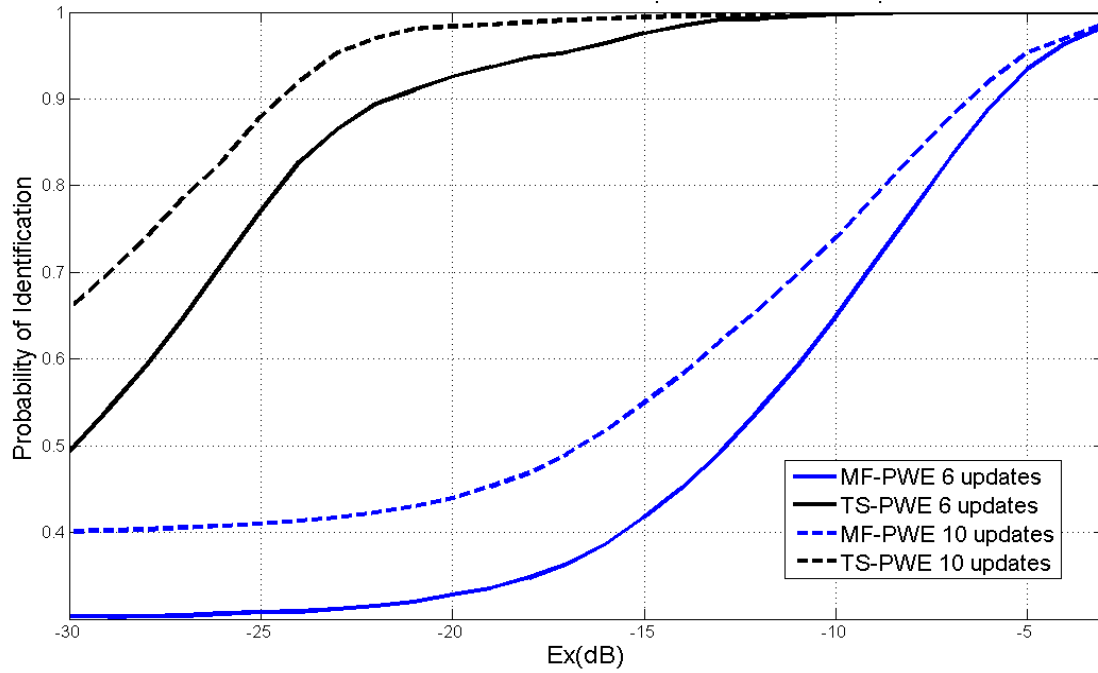


Figure 32. TS-PWE vs MF-PWE identification performance comparison as parameterized by the number of updates (or number of transmissions) assuming unity noise energy.

In summary, the region of low SNR is usually the most interesting in any detection problem whether it is radar, communications, etc. This is because the probability of detection is a function of SNR. The lower the SNR means the lower the probability of detection where there is usually very little can be done except the obvious which is to either increase signal energy or lower noise power. Here, although both MF-PWE and MAP-PWE are superior to various waveforms in improving probability of detection at low SNR, we are still able to produce more gain with TS-PWE at low SNR. The use of both previous-to-last and latest likelihoods allows for the TS-PWE scheme to temper volatile updates due to large noise realizations. As such, TS-PWE performance improvement in the low SNR region is significant.

THIS PAGE INTENTIONALLY LEFT BLANK

VIII. MULTIPLE TARGET IDENTIFICATION AND RANGE-DOPPLER LOCATION

It is our goal to simultaneously identify the target type, determine how many targets in each type and correctly locate the ranges and Doppler for multiple moving targets. Range-Doppler via ambiguity function for point targets is well covered in the literature. A good starting point is [4]. In this section, we utilize range-Doppler map (RDM) to correctly locate an extended target. We integrate RDM in our CR platform to simultaneously identify a target from a set of possibilities with the use of our adaptive PWE waveforms. We investigate different scenarios and finally form our comprehensive scheme.

A. TWO TARGETS OF SAME TYPE SCENARIO

In this section, the goal is to jointly locate (in range and Doppler) and identify two targets of same type with arbitrary speeds and delays (range). Other complicated scenarios will ensue in later sections. In Fig. 33 we illustrate the two present extended targets in RDM where a small amount of noise is added. The top panel is a three-dimensional RDM. The bottom panel is a two-dimensional RDM (which is the conventional way of illustrating RDM). For simplicity and brevity, we choose sample delay (for range) and normalized frequency for Doppler (for velocity). Both parameters can easily be converted to actual range and velocity from the RDM. The overall probability of correctly locating an extended target in range-and-Doppler and identifying target type is clearly a function of received signal-to-noise ratio, number of transmissions L , PWE schemes and the target responses themselves via maximum target eigenvalues. In this scenario, we assume that two present targets are of the same type. Since we already assumed that there are two targets present, our problem therefore is to figure out where these two targets are in range-and-Doppler and identify the target type from various possibilities simultaneously. In practice, a priori assumption may come from other sensors or some intelligence information. To perform integrated range-and-Doppler location and target type identification given they are of same type, we utilize our closed-loop update procedure with the use of PWE waveforms. With the previous identification

problem where transmission number is fixed, the target with the largest weight update is chosen to be the detected hypothesis. Since we know that there are two targets, we choose the hypothesis with the largest weight updates after a fixed number of transmissions.

We now describe the scenario. Assuming $M = 4$ possible extended target types, we form the normalized eigenwaveform for each target hypothesis and scale each eigenwaveform with the square-root of the initial waveform weight assigned to each target and then form the first PWE-based waveform (as previously when we assumed the target to be static). The difference here is that we now send a series of pulses R times (in this work, $R=31$), since we are interested in forming RDMs. For the received return from every set of R pulses (recall that there are L transmissions, where there are R pulses in each transmission), M matched filters from all possible extended targets are applied to form the Doppler filter banks to form M RDMs. For fair comparison, we set unity energy of each transmission (R pulses). Assuming N is the length of target impulse response, the matched filtered sequence takes on a length of $4N-3$ for any target present. If the SNR is sufficient, the two highest magnitudes in the RDM may indicate the range-Doppler locations of the two targets. Due to noise realization, one magnitude is slightly higher than the other. We pick the $4N-3$ sequence corresponding to the larger one to use for our likelihood update calculations. To properly scale the next PWE waveform weights, we normalize the sum of the likelihood to one as usual and form the waveform weights such that the energy constraint is accommodated (58). We continue until we send the fixed number of transmission L . We choose the target type with the largest likelihood value which allows us to pick the RDM out of the four possible RDMs. Since there are two targets, we pick the two range-Doppler cells with the largest magnitudes. Thus, we have jointly decided the target type and located the range-Doppler cells where the two targets may be located. The illustration of RDMs updates for each target type is shown in Fig. 33 to Fig. 36 where the two targets can be easily determined in the “decided” RDM after five updates in Fig. 36. Here, we use MF-PWE as the designated PWE scheme.

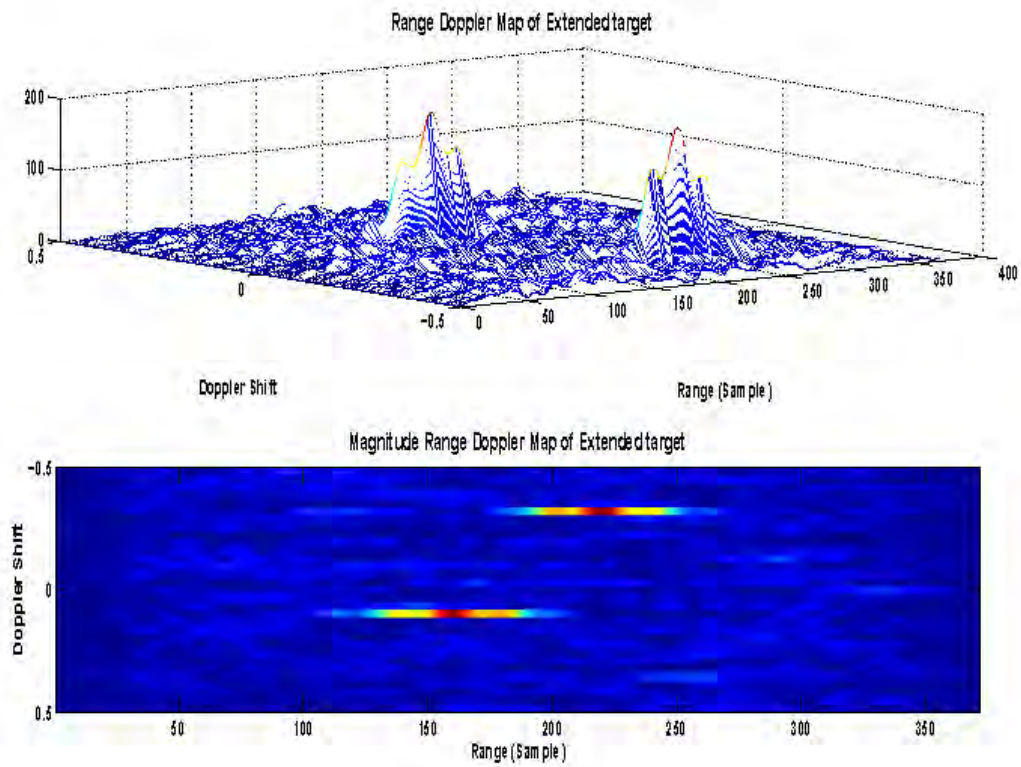


Figure 33. Range Doppler map of two targets of the same type (some noise added).

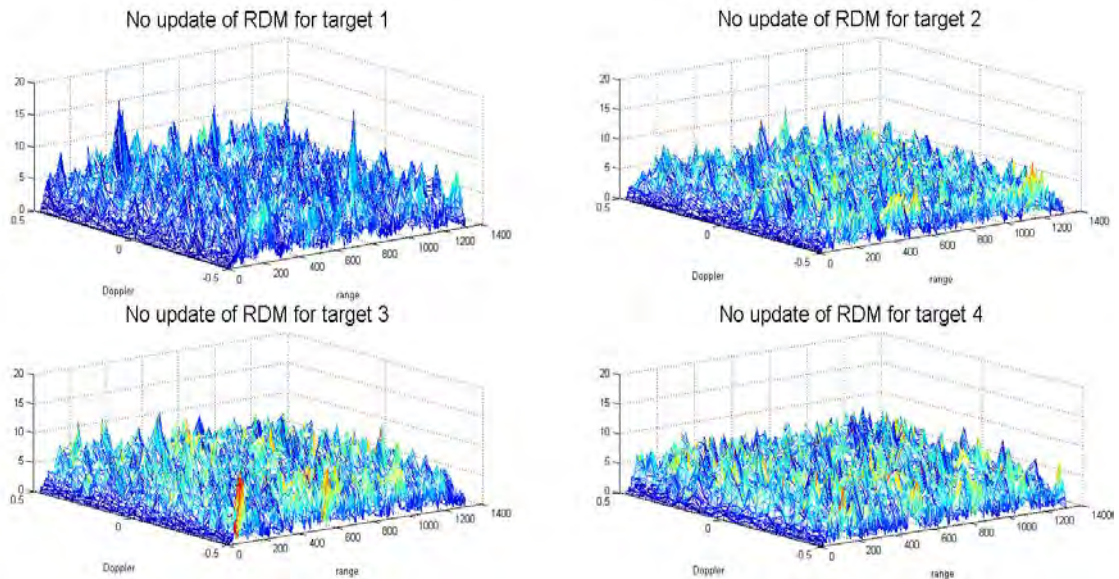


Figure 34. Four candidate RDMs for four possible target types (where two targets of the same type are present) with PWE after one transmission (no update).

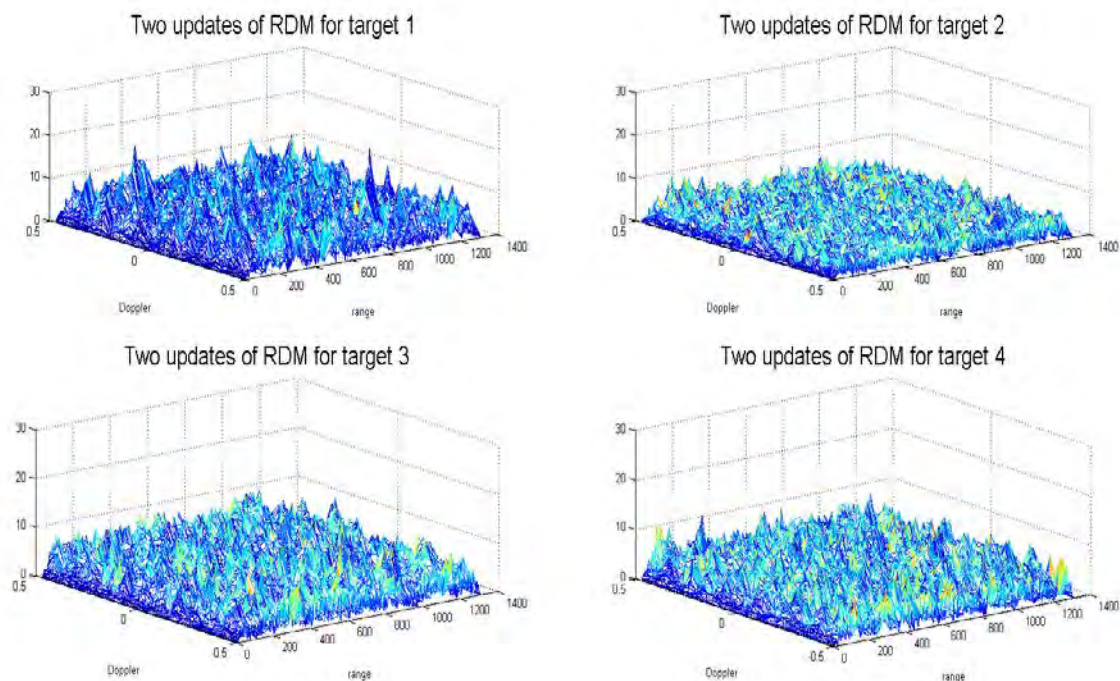


Figure 35. Four candidate RDMs for four possible target types (where two targets of the same type are present) with PWE after three transmissions (two updates).

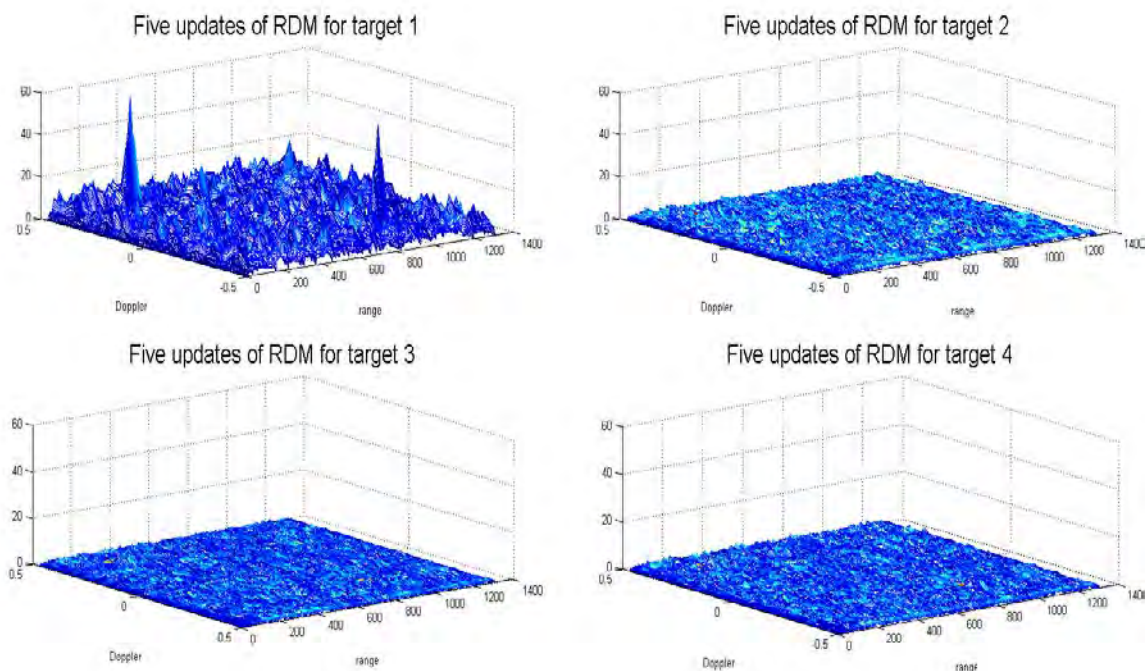


Figure 36. Four candidate RDMs for four possible target types (where two targets of the same type are present) with PWE after six transmissions (five updates).

In Fig. 37, the probability of identification (P_i which is the probability of correctly determining target type), P_d which is the probability of correctly determining the range-Doppler location, and the overall or joint probability (P_g) with one transmission (no update) and six transmissions (five updates) using MF-PWE scheme are shown via MC experiments. The overall probability is the probability that the range-Doppler location and target type are both correct. In other words, if we correctly determined the target type and not correctly determined the correct range-Doppler cell (despite the fact that the actual RDM peak is in an adjacent cell), we still count this against the overall probability. Notice also that the probability of correct identification is better than the probability of correctly determining the range-Doppler locations. This is because in our experiment, there are only four possible target types while there are numerous range-Doppler cells. We can improve P_g by increasing the range-Doppler area (number of cells) in which to decide where the target may be located. For the moment, this is outside the scope of our study but definitely is an interesting one to tackle at a later time.

It is also clear from Fig. 37 that the overall performance (bottom panel) is jointly affected by probability of identification and probability of correctly determining the range and Doppler location (upper and middle panels). From transmit energy of -4 to 0 dB energy units which lead to almost perfect identification percentage ($P_i = 1$), P_g is almost exactly the same as P_d . Recall that, we put a very strict definition on P_d , i.e., we only declare range-Doppler detection when the matched filtered peak is truly located where the true target peak would be (although, the peak may simply be in the adjacent range-Doppler) cell. It is also important to notice that more transmissions help both identification rate as well as overall performances.

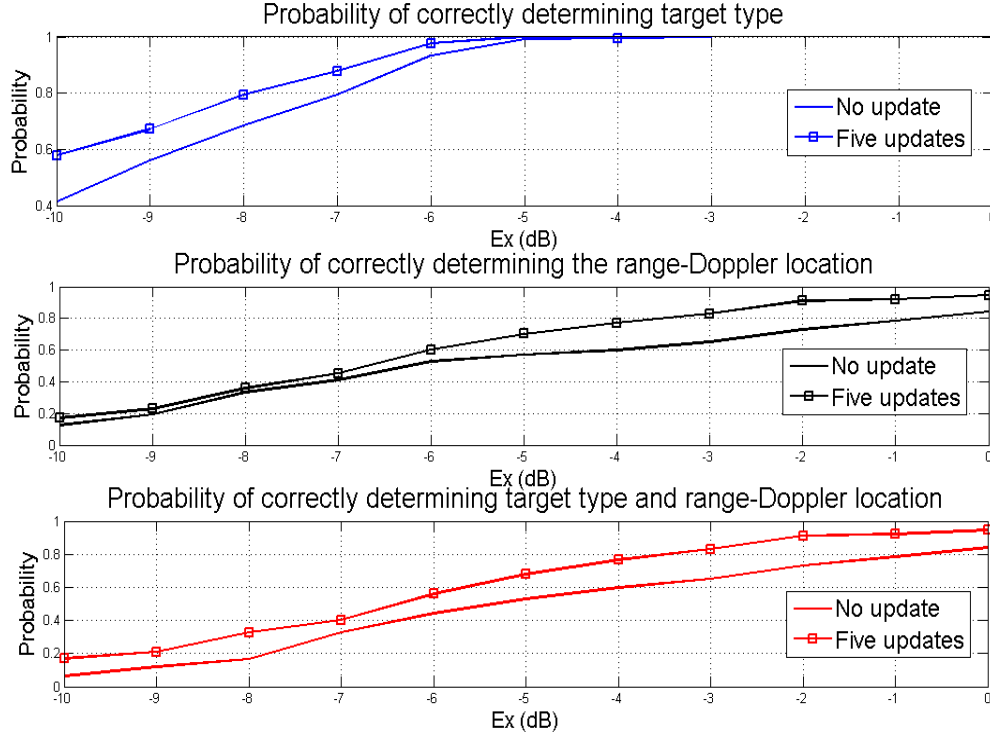


Figure 37. Probability of correctly determining target type, probability of correctly determining the range-Doppler location, and the overall performance of correctly determining target type and range-Doppler location using MF-PWE with two targets of same type.

In Fig. 38, we show the comparison of identification probability (P_i) of six updates and ten updates with various PWE schemes for the two moving extended targets (of same type scenario). It is obvious that P_i is function of both PWE method and number of transmissions (or update number). It is clear that TS-PWE has the best performance in terms of probability of correct identification especially in the low-SNR area. Since MF-PWE and TS-PWE are again the best performers, we utilize both in Fig. 39. In Fig. 39, the overall probability comparison between MF-PWE and TS-PWE are shown for three transmissions and six transmissions. Notice that for three transmissions, TS-PWE performs slightly lower than MF-PWE. However, at six transmissions, TS-PWE is better. This means that although TS-PWE is better than MF-PWE at target identification, it is not always better than MF-PWE in probability of correctly determining range-Doppler location. Higher transmission number is needed for that to happen.

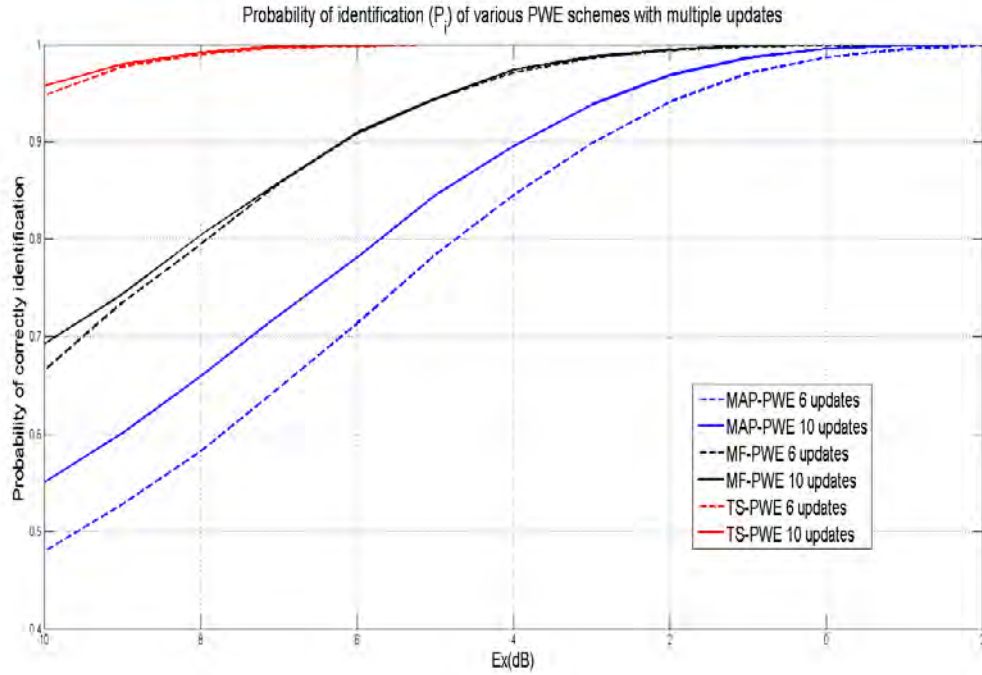


Figure 38. Identification probability comparison of six updates and ten updates of various PWE schemes assuming unity noise energy for two targets of same type scenario.

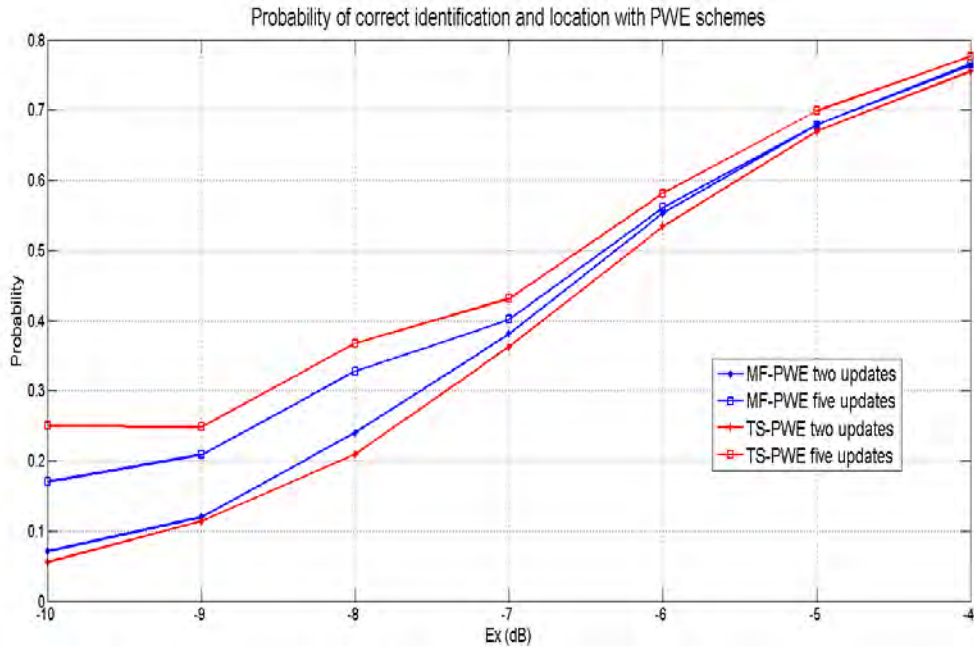


Figure 39. Probability comparison of correctly determining targets type and range-Doppler location of no update, one update, two updates, and five updates vs MF-PWE and TS-PWE schemes assuming unity noise energy with two targets of same type.

In summary, we slightly modified the CR platform to adapt the assumption of two target of same type and form a platform that can correctly identify the target and correctly indicate the range-Doppler location or cell for moving extended targets. We used the three PWE-based waveforms all of which are effective in terms of three probabilities mentioned above. TS-PWE is the most effective in terms of target recognition specifically in low SNR.

B. UNKNOWN NUMBER OF TARGETS (OF THE SAME TYPE)

In this section, we do not assume the number of targets present but since this is a target recognition problem we will generate at least one target present in our MC experiments. If there are multiple targets, we assume they are of the same type in this section. Other complicated scenarios are tackled in later sections. We will utilize MF-PWE and TS-PWE schemes. Here, we modify the receiver to incorporate thresholds dictated by a given false alarm since a true detection problem is added into the mix, i.e., the number of targets present is not known (but we at least assume one). As before, the hypothesis with the largest updated waveform weight is deemed to be the true target hypothesis. The sequences containing highest magnitudes in the chosen RDM may be retrieved for target range and Doppler location. The question here is to determine how many targets there are in latest updated RDM and what is the proper threshold to be used in locating targets' range and Doppler.

We assume targets are of length N (in this work, $N = 31$) and the length of test sequence \mathbf{y} containing peak value in RDM is $4N - 3$. In order to form each range Doppler map, R pulses are transmitted (in this work, $R = 31$). The \mathbf{H}_i is the $2N$ -by- N convolution matrix of target type i and \mathbf{w} is the complex-valued AWGN vector. Each time the radar transmits a waveform \mathbf{x} , a noise-corrupted version of the reflected target echo is received. Since we have four possible (i.e., different) targets, we use the four different matched filters as usual for MF-PWE. The $f_{ji}(\mathbf{y})$ which is the likelihood of j^{th} hypothesis given i^{th} target is of this form

$$f_{ji}(\mathbf{y}) = \beta \exp[2 \operatorname{Re}(\mathbf{s}_j^H \mathbf{y})] \quad (76)$$

where we can substitute $\mathbf{y} = \mathbf{H}_i \mathbf{x} + \mathbf{w}$ and $\mathbf{s}_j = \mathbf{H}_j \mathbf{x}$ into (76).

Before we can determine range-Doppler location, we have to consider the problem of detection for the entire range-Doppler map since we do not know the number of targets. The detection hypotheses are

$$\begin{aligned} H_0 : \mathbf{y} &= \mathbf{w} \\ H_1 : \mathbf{y} &= \mathbf{H}_i \mathbf{x} + \mathbf{w}. \end{aligned} \quad (77)$$

It can be shown that the natural log likelihood for the null hypotheses given i^{th} target is of normal distribution of the form

$$\ln[f_{0|i}(\mathbf{y})] = \ln \beta + 2 \operatorname{Re}(\mathbf{s}_i^H \mathbf{w}), \quad (78)$$

and the hypotheses H_1 is

$$\ln[f_{1|i}(\mathbf{y})] = \ln \beta + 2 \operatorname{Re}(\mathbf{x}^H \mathbf{H}_i^H \mathbf{H}_i \mathbf{x} + \mathbf{x}^H \mathbf{H}_i^H \mathbf{w}). \quad (79)$$

It can be shown that the likelihood ratio threshold r for given probability of false alarm P_{FA} and AWGN of sample variance σ_w^2 is of the form

$$r = \sqrt{2E_s \sigma_w^2} Q^{-1}(P_{FA}) + \ln \beta. \quad (80)$$

Thus, the probability of a target being in a specific range and Doppler location for target type i is

$$\begin{aligned} P_D &= Q\{Q^{-1}(P_{FA}) + \sqrt{\frac{2E_s}{\sigma_w^2}}\} \\ &= Q\{Q^{-1}(P_{FA}) + \sqrt{\frac{2L \mathbf{x}^H \mathbf{H}_i^H \mathbf{H}_i \mathbf{x}}{\sigma_w^2}}\} \\ &= Q\{Q^{-1}(P_{FA}) + \sqrt{\frac{2L(\sum_{j=1}^M w_j \mathbf{q}_j)^H \mathbf{R}_i (\sum_{j=1}^M w_j \mathbf{q}_j)}{\sigma_w^2}}\}, \end{aligned} \quad (81)$$

where the transmission number L is incorporated and \mathbf{R}_i is the autocorrelation matrix of i^{th} target response.

It is clear from a previous chapter that E_s is not unique. The value of P_D is affected by transmit signal energy and weights for each eigenvector, target response energy, and maximum eigenvalue. If the PWE update process converges to the true target type and mostly distributes the weight to target type i (true target), the detection probability for each range-Doppler cell given correct target type identification is shown in (81). However, if the procedure makes the wrong target type identification (which means most energy is not in the i^{th} target type), the probability of locating the correct range-Doppler cell will tend to be very low as shown in Fig. 40 where target 1 is the correct target type. Wrong identification also leads to poor probability of locating range-Doppler location.

It can be shown that when correct target type identification is made and all transmit energy is distributed to correct target type, the equation (81) can be modified as

$$\begin{aligned} P_D &= Q\{Q^{-1}(P_{FA}) + \sqrt{\frac{2L(\mathbf{q}_i^H \mathbf{R}_i \mathbf{q}_i)}{\sigma_w^2}}\} \\ &= Q\{Q^{-1}(P_{FA}) + \sqrt{\frac{2\lambda_{\max} L E_x E_h}{\sigma_w^2}}\}, \end{aligned}$$

where E_h is the energy of target response and is assumed to be unit energy in this section.

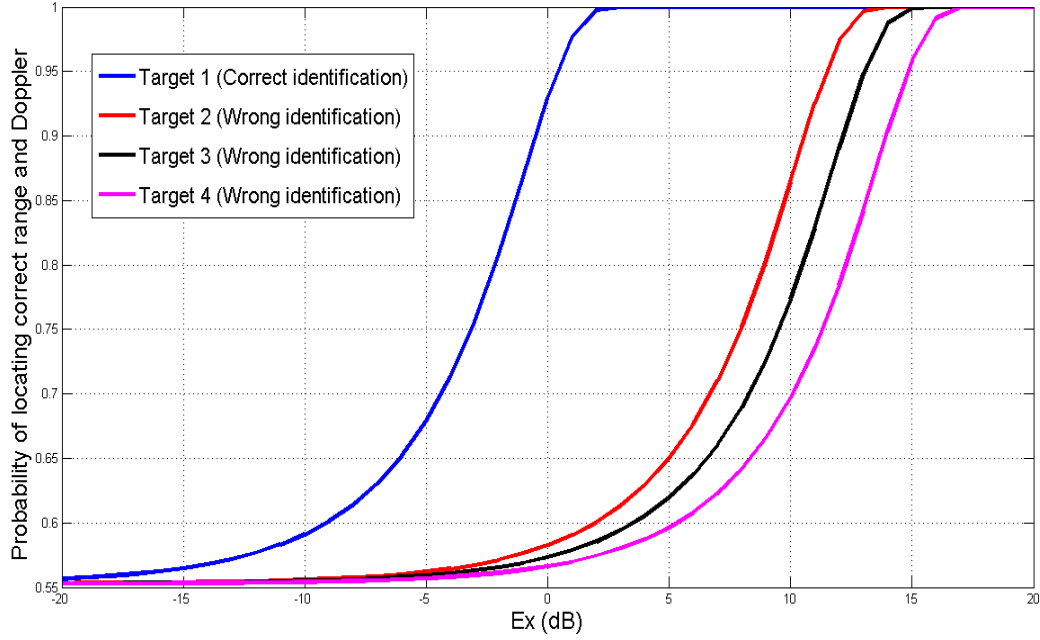


Figure 40. Probability of locating correct range and Doppler given target type identification and probability of false alarm ($P_{FA} = 0.1$) assuming unity noise energy where type 1 is the correct hypothesis.

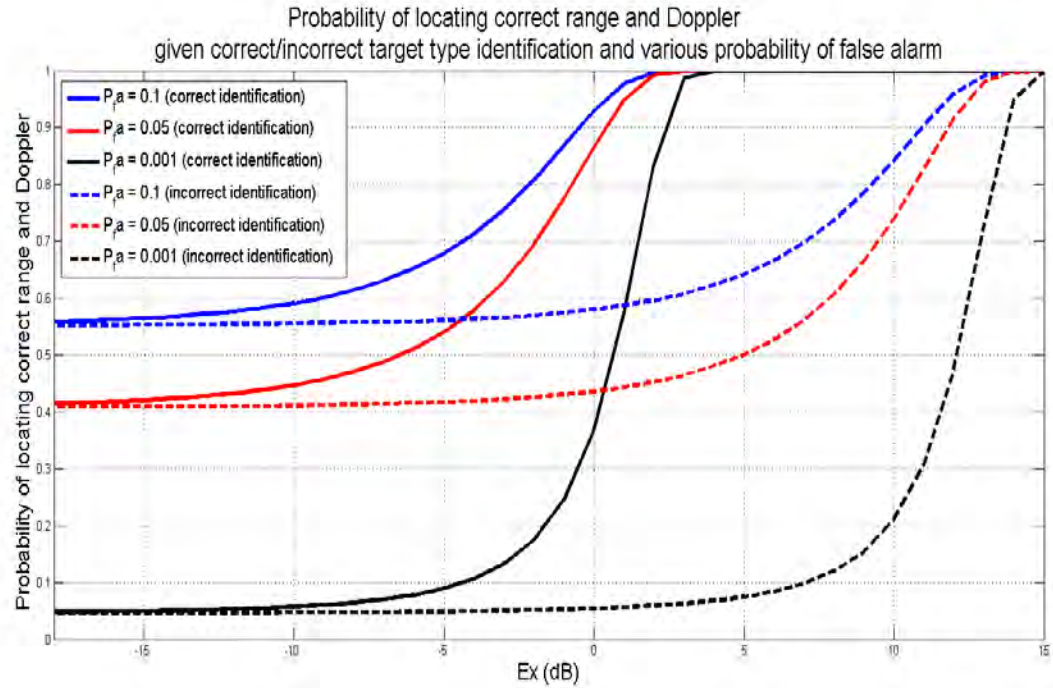


Figure 41. Probability of locating correct range and Doppler given correct/incorrect target type identification and various probability of false alarm assuming unity noise energy.

Also, in Fig. 41, it shows clearly that the probability of correctly locating range and Doppler is intimately tied to the probability of target type identification. The plots in Fig. 41 re-enforces the fact that once a wrong identification is made then the probability of correctly locating the range-Doppler cell of a target becomes much lower.

Again we set up Monte Carlo experiments where we randomly generate the number of targets and the range-Doppler locations of those targets. In this particular experiment we generate one, two, or three targets (of the same type) while assigning range-Doppler locations (randomly) in each experiment. In our joint recognition-detection procedure, recall that we identify the targets by choosing the RDM. Again since we do not know the number of targets, we have to perform detection via threshold in the entire RDM. The threshold is based on the PFA given a target type from (80). Once targets are “detected,” then we try to determine the targets’ range-Doppler locations. Since this is a detection problem, the threshold used dictates the actual P_d . Using MF-PWE, we calculate the “strict” overall probability P_g (which is correct identification, correct number of targets and correct range-Doppler locations all at the same time) as a function of transmit energy. Notice that P_g is tied to PFA (since P_d is tied to PFA). It is clear that in Fig. 42 that the threshold (calculated from probability of false alarm) and the number of updates affect overall probability.

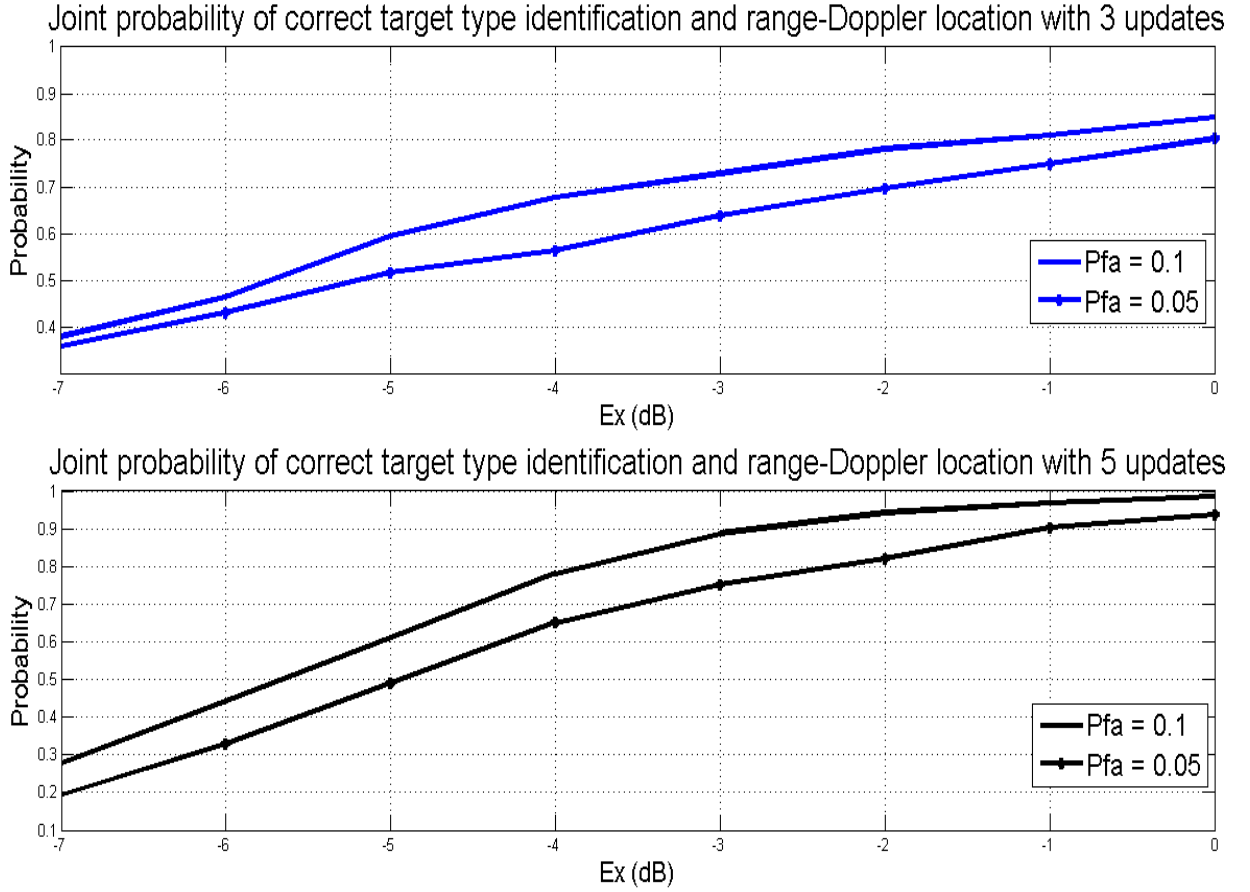


Figure 42. Joint probability of locating correct ranges, Doppler and target types vs various MF-PWE updates numbers given probability of false alarm assuming unity noise energy.

C. TWO TARGETS OF DIFFERENT TYPES (SCENARIO)

In this section, we make the problem a little more interesting. Here we allow for different target types to be in the scene. For now, let us limit the number of targets to two (and then we'll consider more in a later section). Assuming the number of targets (here two) removes the detection component of the signal processing since we already know the number of targets. This is akin to the "two targets of the same type scenario." However, in this problem, we have two different targets.

We may consider the problem that of a multiple hypothesis testing (MHT) problem. Unfortunately, in practice when there are more possible targets to consider and when there are more scenarios to consider (e.g., ten targets total, two targets are type 1, 2

targets are type 2, one target is type 3, etc.), then the number of hypotheses increase dramatically due to the combinatorial implications to the number of hypotheses. If we are to field a practical cognitive radar system, then its computing resource has to be reasonable. As such, we will focus on how to update the waveform weights via the likelihoods corresponding to the original four hypotheses in the target recognition problem. This reasonably makes sense. For example, if there are two different target types (say type 1 and type 3) in four, it would make sense that after a few transmissions that the w_1 and w_3 approach 0.5 such that the overall waveform favors those two types.

We illustrate the procedure in Fig. 43. Amazingly, there's very little difference between this procedure to that of "two targets of the same type scenario." Here, effectively the only difference is that we choose two RDMs in the end. Also, the waveform weights will be distributed to the two target types (about 0.5 each when homing in on the two targets).

We conduct an experiment where two targets are present (type 1 and type 4) using the procedure in Fig. 43. We show the 4 RDMs after the first transmission (no waveform update) in Fig. 44. Notice that it is difficult to tell where the targets are. Now we show what happens to the RDM after seven transmissions in Fig. 45. Notice that the two peaks in the two RDMs corresponding to targets type 1 and type 4. Clearly, the procedure can correctly identify two targets and correctly determine range-Doppler locations.

Flow diagram/procedural steps for the two different targets

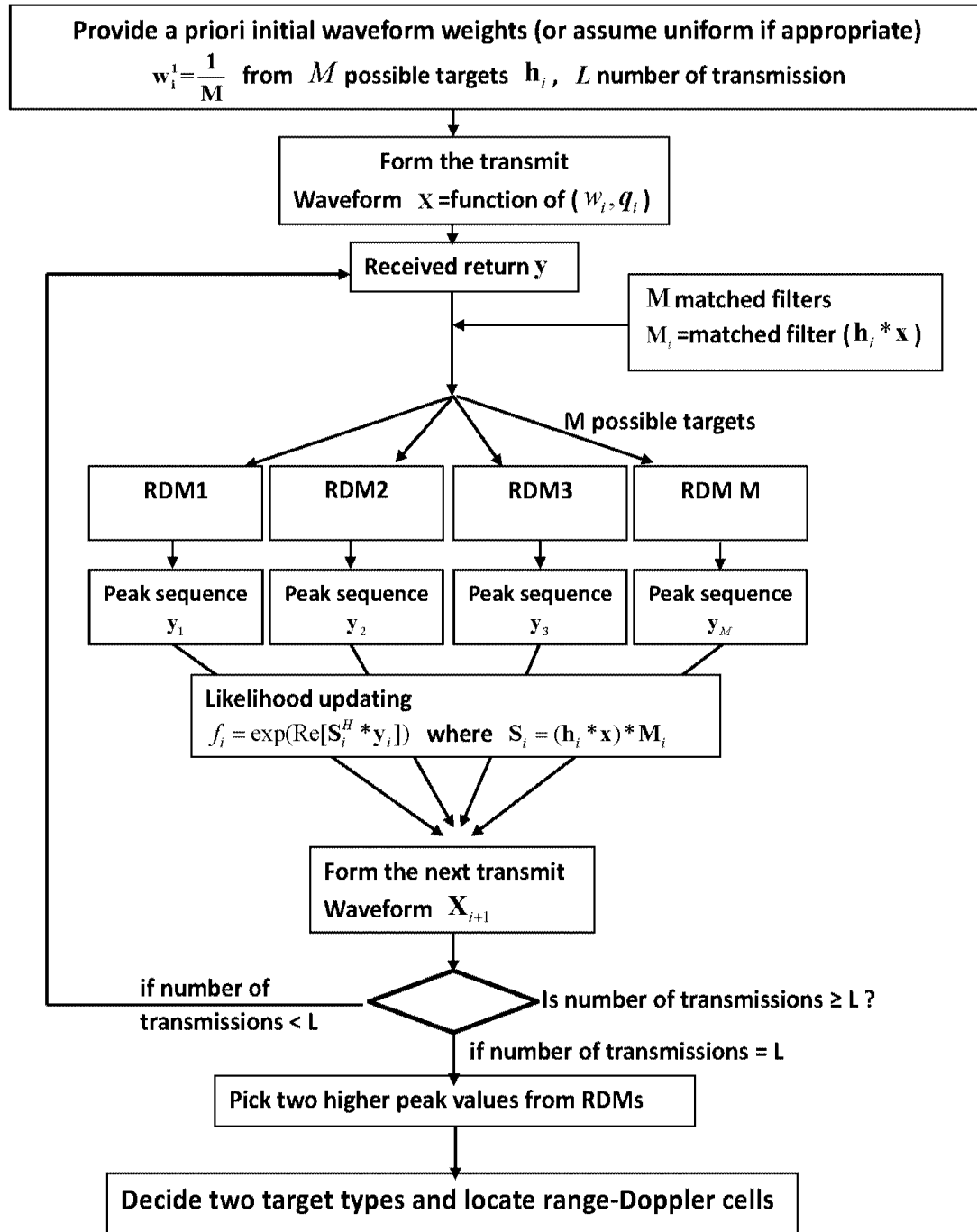


Figure 43. Flow diagram/procedural steps for two different target types (scenario).

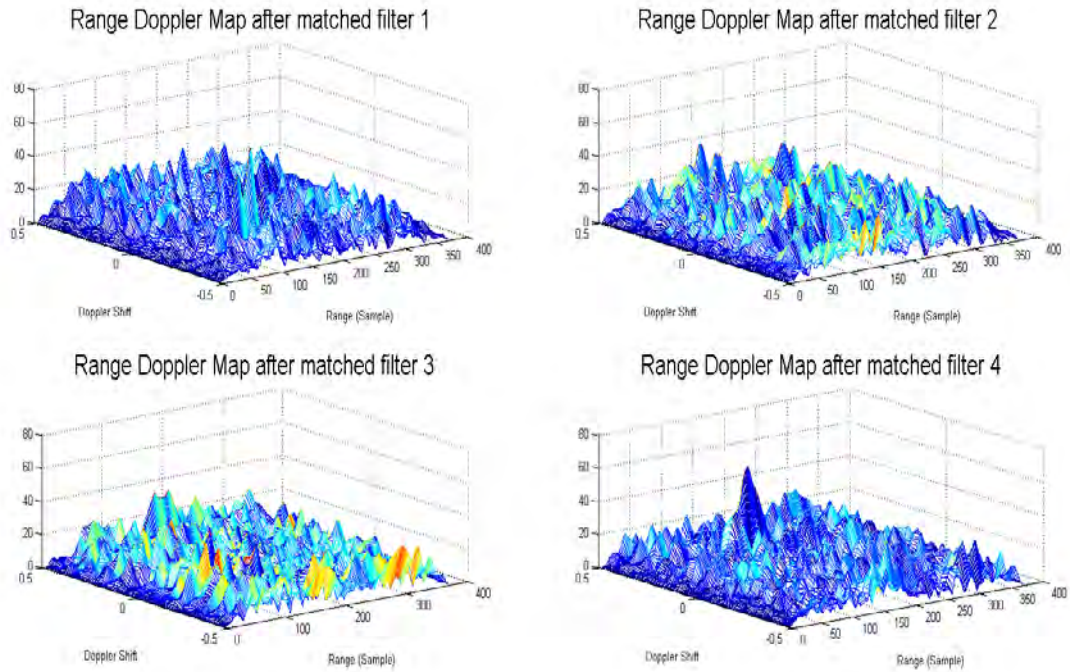


Figure 44. No update: RDMs of two targets from different types after M matched filters ($M = 4$).

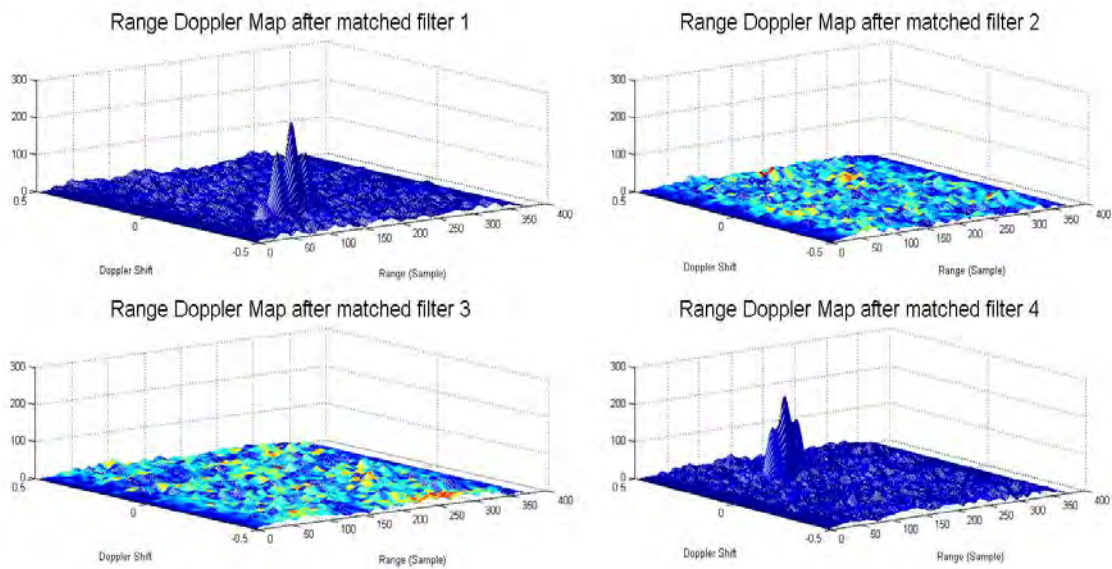


Figure 45. Six updates: RDMs of two targets from different types after M matched filters ($M = 4$).

Via Monte Carlo experiments, we illustrate the overall (or joint) probability of correctly identifying (both target present) and their range-Doppler locations in Fig. 46 with the use of MF-PWE and TS-PWE adaptive waveforms as a function of transmit energy while varying the number of transmissions (or updates). If we compare Fig. 39 (same target type) and Fig. 46 (different target types), it is clear that performances are lower for Fig. 46. This is because the waveform weights are distributed between two targets (for different types) while the weight gets distributed mostly to one target (for same target type), which seems intuitive.

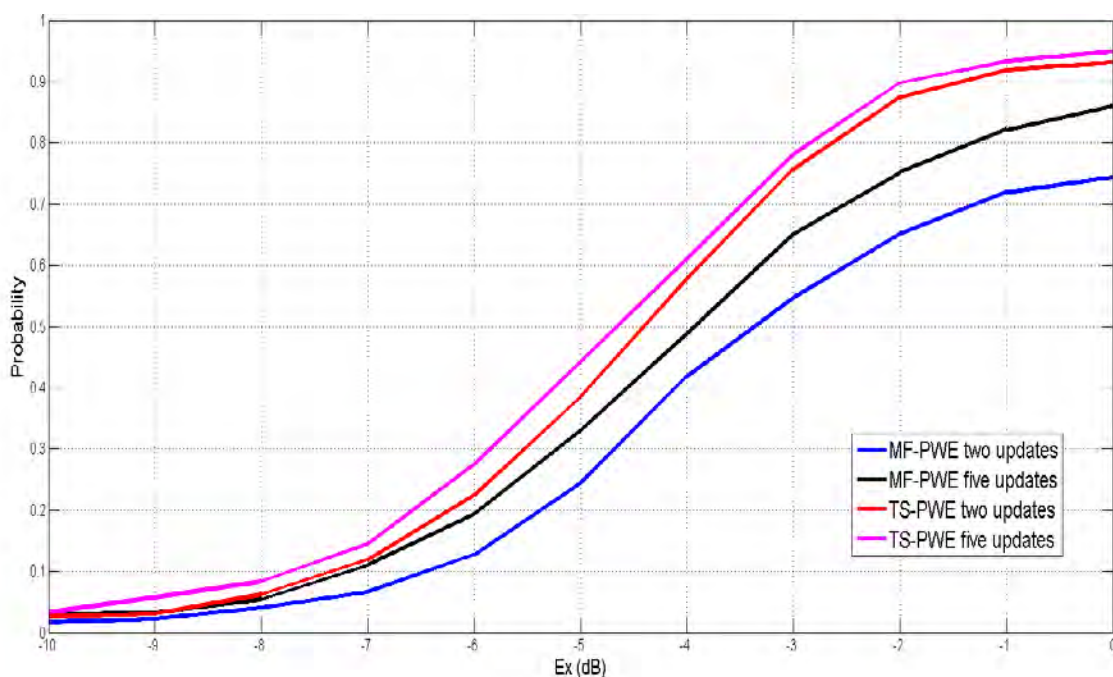


Figure 46. Overall probability of identification and location for two targets of different types assuming unity noise energy.

D. UNKNOWN NUMBER OF TARGETS AND DIFFERENT TYPES OF TARGETS

In this section, we assume that the number of targets is not known or there could be multiple targets in the scenario. Moreover, there could be multiple target types. However, we assume that number of target types present is less than the possible target types. This assumption is from the intuition gained from the previous section. If there are

two out of four target types then the waveform weights for the two targets will eventually reach ~ 0.5 . If there are three out of four, then the weights will eventually reach ~ 0.33 . So for four out of four, then it will simply revert to 0.25 as intuition would dictate. Our goal is to utilize the insights gained from the three scenarios above to form a comprehensive scheme to simultaneously figure out the number of targets, identify target types, and determine the range-Doppler cells of these targets.

Let us start from a general scenario where there are M possible target types (regardless of the number of targets present). If there is one target type, then the large or “high” waveform weight distribution goes to the correct target hypothesis (assuming enough SNR and enough transmissions) which approaches 1 as the platform homes in on the correct target type while the other (“low”) weights approach zero. For two target types, the “high” weights would approach 0.5 (assuming enough SNR and enough transmissions) and so on as so forth. As the number M of the possible types increases, the weight differences between the group of “high” weights and the group of “low” weight decrease. In other words, it may be harder to correctly identify how many types of present targets there are as the number of present target types increases. It can be shown that the weight distribution for MF-PWE for M possible target types where j indicates targets that are not present and i indicates targets that are present is the following:

$$\begin{aligned}
 W_k &= \frac{E[f_{k|i}(x)]}{\sum_{\forall i} E[f_{i|i}(x)] + \sum_{\forall j} E[f_{j|i}(x)]} \\
 &= \frac{\exp[\frac{2E_x}{E_{\bar{x}}} (\sum_{j=1}^M \sqrt{w_j} \mathbf{q}_j)^H \mathbf{R}_k (\sum_{j=1}^M \sqrt{w_j} \mathbf{q}_j)]}{\sum_{\forall i} \exp[\frac{2E_x}{E_{\bar{x}}} (\sum_{r=1}^M \sqrt{w_r} \mathbf{q}_r)^H \mathbf{R}_i (\sum_{r=1}^M \sqrt{w_r} \mathbf{q}_r)] + \sum_{\forall j} \exp[\frac{2E_x}{E_{\bar{x}}} (\sum_{r=1}^M \sqrt{w_r} \mathbf{q}_r)^H \mathbf{H}_j^H \mathbf{H}_i (\sum_{r=1}^M \sqrt{w_r} \mathbf{q}_r)]}, \tag{82}
 \end{aligned}$$

where $k=1,2,\dots,i$ is the index for present target type. In (82), recall that we assume $\sigma=1$ for simplicity.

The first term in the denominator is

$$\sum_{\forall i} E[f_{i|i}(x)] = \sum_{\forall i} \beta \exp\left[\frac{2E_s}{E_1} \left(\sum_{r=1}^M \sqrt{w_r} \mathbf{q}_r\right)^H \mathbf{R}_i \left(\sum_{r=1}^M \sqrt{w_r} \mathbf{q}_r\right)\right], \quad (83)$$

which is the summation of all likelihoods of present targets. And the second term is the summation of all likelihoods of targets not present and is given by

$$\sum_{\forall j} E[f_{j|i}(x)] = \sum_{\forall i} \beta \exp\left[\frac{2E_s}{E_1} \left(\sum_{r=1}^M \sqrt{w_r} \mathbf{q}_r\right)^H \mathbf{H}_j^H \mathbf{H}_i \left(\sum_{r=1}^M \sqrt{w_r} \mathbf{q}_r\right)\right]. \quad (84)$$

The TS-PWE weight distribution of M possible types is more difficult to analyze because it involves the modified likelihood functions.

In this final section, we also include the case where there may not be a target. In section B, although we assumed the number of targets to be unknown, we did assume in our experiments that at least one target is present. In other words, the set of algorithms in section B has to be modified to accommodate the general case when there is no target present. So here our strategy is to first figure out if there is a target or not in the scenario (after a number of transmissions/updates say L). If there is, then we figure what target type with another set of transmission (same as before i.e., L), and then another until our algorithm says there is no more target (type) present. To this end, the target identification procedure is modified by adding a user-defined threshold ψ (a percentage) and comparing that to a formulated measured $\bar{\psi}$ from the latest weight distribution. The threshold ψ as in any threshold maybe adjusted to improve decision-making of the algorithm. The smaller the threshold ψ is defined, the more sensitive or the more probable it is to identify and detect present targets.

If there are M possible targets, then the “high” weights that will be approached by our likelihood update procedure is $100/M$. The measured $\bar{\psi}$ is then

$$\bar{\psi} = E[w_u] - E[w_v], \quad (85)$$

where w_u are the weights that are above the $(100/M)$ and w_v are lower. If $\bar{\psi}$ is less than the desired ψ , then the threshold is not crossed and thus a target type is not detected. If $\bar{\psi}$ is greater than designated ψ , then we look for the target type that has the

highest weight and deem that to be a present target type. Since it is deemed present, the eigenwaveform corresponding to that target is now removed from the next L number of transmissions. Now we normalize the remaining weights as dictated by (57, 61) and try to ascertain if there are remaining targets. In other words, we terminate the transmissions when $\bar{\psi}$ is not greater than our threshold ψ .

The full procedure for an experiment is summarized in Fig. 48 and enumerated here.

1. Assuming M possible extended targets, generate the normalized eigenwaveform for each target. Decide which PWE waveform is used and set the user-defined threshold ψ . Scale each eigenwaveform with the square-root of the initial weight assigned to each hypothesis and then form the first PWE-based waveform.

2. After the first return, calculate the likelihood according to the choice of PWE scheme. For MAP-PWE, use (59) and (69) is for MF-PWE and TS-PWE. Continue transmissions until the desired number of transmissions L (or updates which is $L-1$). Note here, the TS-PWE requires at least 2 transmissions to implement.

3. Update the weight distribution (75) and calculate the measured $\bar{\psi}$ by (85).

4. Decide if there is a target. Recall that target present is decided if the measured $\bar{\psi}$ is greater than designated ψ . In our experiment, ψ is set 10 percent. If $\bar{\psi}$ is less than designated value, go to step 7.

5. Determine the number of targets from the latest RDM of the decided type. This is performed by using the traditional threshold to the entire RDM. The threshold is calculated from (80) and is a function of probability of false alarm.

6. Go back to step 1 and eliminate the accepted target type. That is, $\bar{M} = M - 1$. Also, we remove the likelihood for this target type in calculating the new waveform weights as dictated by (56, 57).

7. If $\bar{\psi}$ is less than ψ , decide there is no more target present and end the algorithm.

The overall (or joint) performance of correctly identifying the number of targets, target types, and locating range-Doppler cell for those targets is shown in Fig. 47. In this work, we use $M = 4$, $\psi = 10$ and $P_{FA} = 0.1$ to compare with various waveforms. Since our procedure identifies each target every L number of transmission (or $L-1$ updates), the plots are parameterized by number of updates per target type. It is obvious that both the MF-PWE and TS-PWE perform much better than wideband waveform as may be expected. The algorithm presented here (used in a CR platform) clearly can be used for the general problem of figuring out the number of target present, target type identification, and correctly locating range-Doppler cells of those targets. The flow diagram is summarized in Fig. 48.

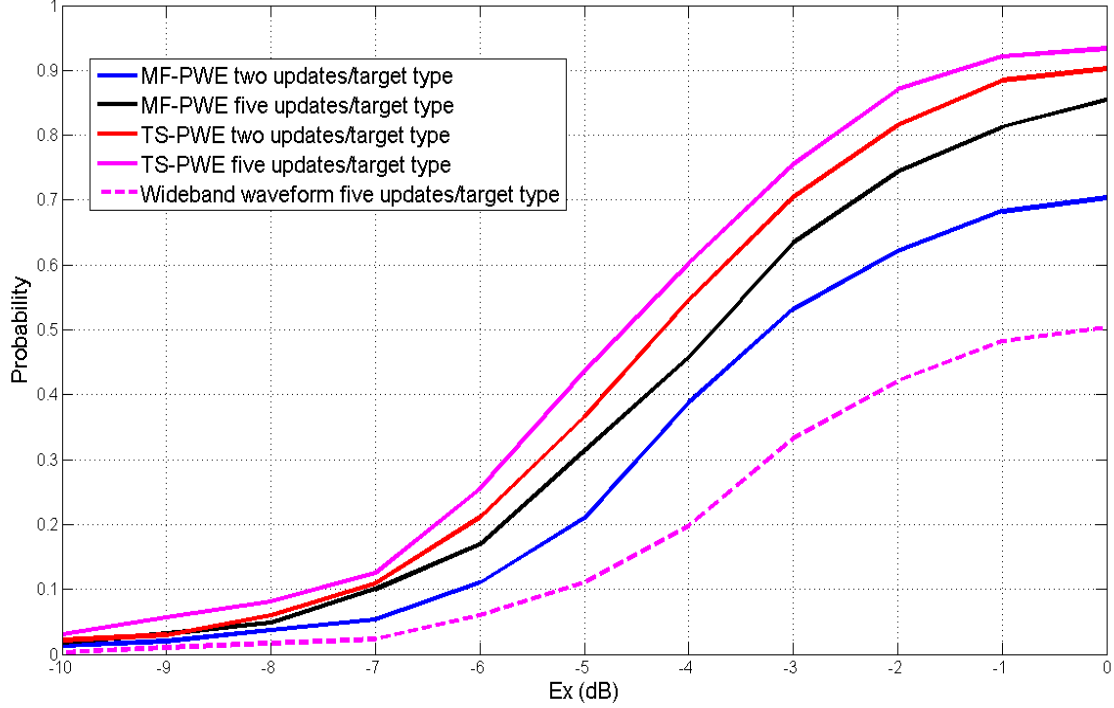


Figure 47. Overall probability of identification and location for multiple targets of unknown types assuming unity noise energy ($\psi = 10$ percent and $P_{FA} = 0.1$).

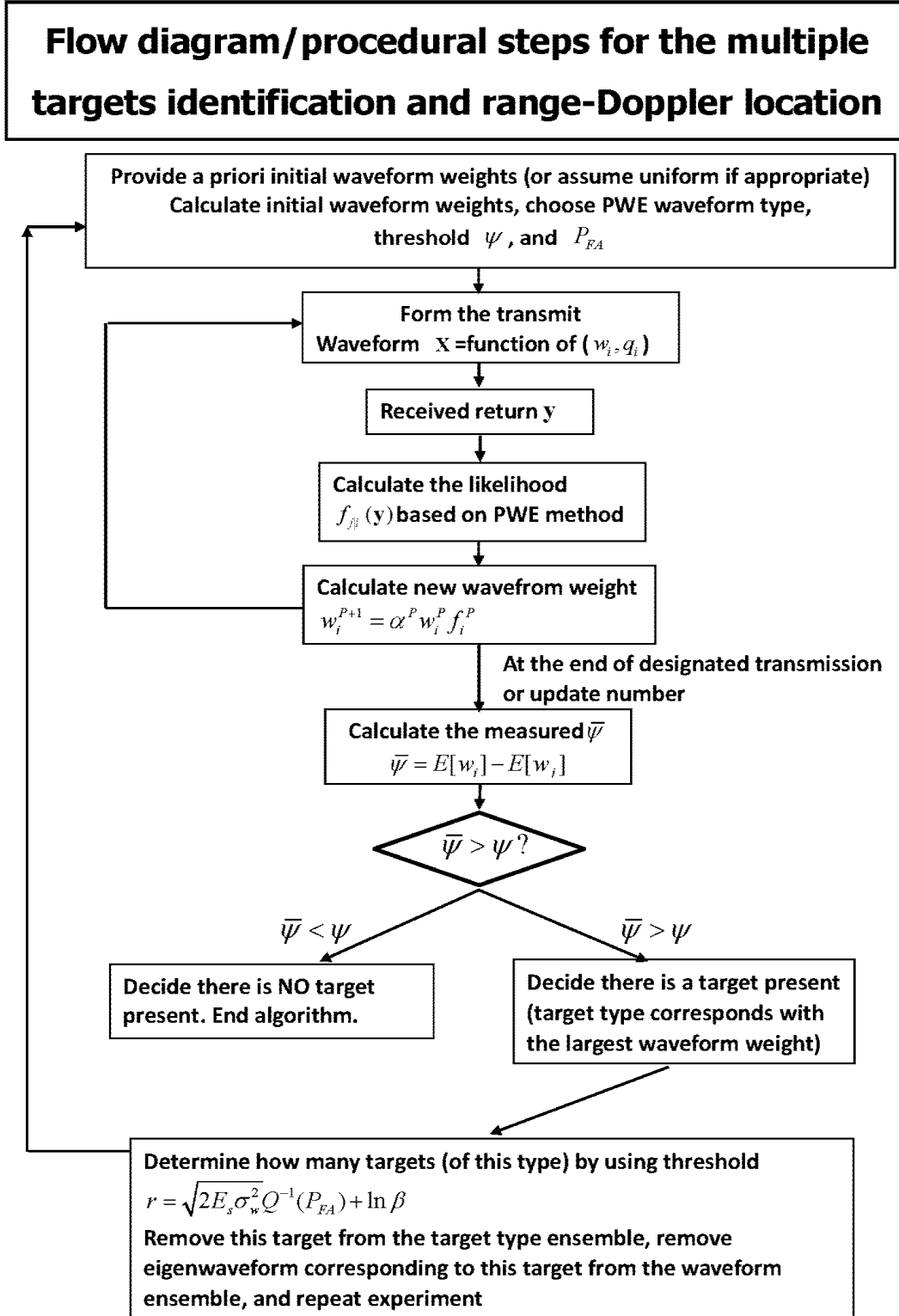


Figure 48. Flow diagram/procedural steps of multiple targets identification and range-Doppler location algorithm.

IX. CONCLUSION

In this work, we set out to fulfill three main related objectives. The first is to investigate the application of eigenwaveform to ambiguity function with the intent of integrating PWE-based waveforms with range-Doppler techniques. The second objective is to extend PWE-based waveforms and produce other waveforms based on PWE for identification of extended targets. And finally, the third objective is to design an integrated scheme for the combined problem of range-Doppler location/detection with extended target type identification with the use of a closed-loop radar system employing adaptive waveforms.

We successfully investigated eigenwaveform-based ambiguity functions with the use of three types of targets (oscillatory, non-oscillatory, and one based of a Boeing aircraft). We found that the AF properties (peak and volume) for eigenwaveforms to be much larger than that of traditional waveforms for point targets. Ambiguity function is the basis of range-Doppler map technique. Various range-Doppler trade-offs were made with the use of pulsed eigenwaveforms.

We made improvements to the MAP-PWE by proposing two new PWE-based waveforms: MF-PWE and TS-PWE. Both waveforms performed well in terms of classification over MAP-PWE and classical wideband waveform.

Ultimately, we used the PWE-based waveforms and range-Doppler techniques to form an integrated target identification and range-Doppler target location for moving extended targets. Our integrated scheme with the use of PWE-based waveforms worked well against the traditional wideband waveform in terms of joint probability of detecting targets, identifying target types, and determining range-Doppler locations for those targets.

THIS PAGE INTENTIONALLY LEFT BLANK

APPENDIX

In this appendix, we discuss how we implemented our own ambiguity function (in MATLAB) and how we verified our results.

Let $x[i]$ be a complex-valued discrete-time signal that we would like to analyze with the ambiguity function. For compact presentation, \mathbf{x} is the vector notation of $x[i]$. N is the length of vector \mathbf{x} which means $x[i]$ contains values only when $i = 0, 1, 2, \dots, (N-1)$. We will interchange these notations in the equation.

The definition of discrete ambiguity function is given by

$$|\chi[\tau_n; f_{dn}]|^2 = \left| \sum_{i=0}^{N-1} x[i] \times x^*[i - \tau_n] \times W_N^{f_{dn} \times i} \right|^2 \quad (1)$$

where τ_n is the delay index and f_{dn} is the Doppler spread. Note here $f_{dn} = 0, 1, \dots, N-1$ and

$$W_N^{f_{dn}} = e^{j2\pi \frac{f_{dn}}{N}}.$$

In general the length of f_{dn} may be desired to be different from N . For now, we keep them the same and will expand it later.

Now, we keep the Doppler spread index f_{dn} fixed in (1) and vary the delay index for comparison. For compact presentation, only the χ function is listed out. The equations for positive τ_n are

$$\begin{aligned}
\chi[0; f_{dn}] &= \sum_{i=0}^{N-1} x(i) x^*(i) e^{j2\pi f_{dn} \times i} \\
\chi[1; f_{dn}] &= \sum_{i=1}^{N-1} x(i) x^*(i-1) e^{j2\pi f_{dn} \times i} \\
\chi[2; f_{dn}] &= \sum_{i=2}^{N-1} x(i) x^*(i-2) e^{j2\pi f_{dn} \times i} \\
\chi[3; f_{dn}] &= \sum_{i=2}^{N-1} x(i) x^*(i-1) e^{j2\pi f_{dn} \times i} \\
&\dots \\
\chi[N-1; f_{dn}] &= \sum_{i=N-1}^{N-1} x(i) x^*(i-N+1) e^{j2\pi f_{dn} \times i}.
\end{aligned} \tag{2}$$

And the equations for negative τ_n are

$$\begin{aligned}
\chi[-1; f_{dn}] &= \sum_{i=0}^{N-2} x(i) x^*(i+1) e^{j2\pi f_{dn} \times i} \\
\chi[-2; f_{dn}] &= \sum_{i=0}^{N-3} x(i) x^*(i+2) e^{j2\pi f_{dn} \times i} \\
\chi[-3; f_{dn}] &= \sum_{i=0}^{N-4} x(i) x^*(i+3) e^{j2\pi f_{dn} \times i} \\
&\dots \\
\chi[-(N-1); f_{dn}] &= \sum_{i=0}^0 x(i) x^*(i+N-1) e^{j2\pi f_{dn} \times i}.
\end{aligned} \tag{3}$$

Interestingly, there is a systematic rule for the χ function for fixed Doppler spread index f_{dn} . That is

$$\begin{bmatrix} \chi[-(N-1); f_{dn}] \\ \dots \\ \chi[-2; f_{dn}] \\ \chi[-1; f_{dn}] \\ \chi[0; f_{dn}] \\ \chi[1; f_{dn}] \\ \chi[2; f_{dn}] \\ \dots \\ \chi[(N-1); f_{dn}] \end{bmatrix}_{(2N-1) \times 1} = [\mathbf{K}]_{(2N-1) \times N} [\mathbf{f}]_{N \times 1} \tag{4}$$

where the \mathbf{K} matrix is defined as

$$[\mathbf{K}]_{(2N-1) \times N} = \begin{bmatrix} x^*(N-1) & 0 & 0 & 0 & 0 & 0 \\ \dots & x^*(N-1) & 0 & 0 & 0 & 0 \\ x^*(2) & \dots & \dots & x^*(N-1) & 0 & 0 \\ x^*(1) & x^*(2) & \dots & \dots & x^*(N-1) & 0 \\ x^*(0) & x^*(1) & \dots & \dots & x^*(N-2) & x^*(N-1) \\ 0 & x^*(0) & \dots & \dots & \dots & \dots \\ 0 & 0 & \dots & x^*(0) & x^*(1) & x^*(2) \\ 0 & 0 & 0 & \dots & x^*(0) & x^*(1) \\ 0 & 0 & 0 & \dots & 0 & x^*(0) \end{bmatrix} \quad (5)$$

which is taking the reversed and conjugated \mathbf{x} and is lined up in a special format similar to the convolution matrix. And the \mathbf{f} matrix is defined as

$$[\mathbf{f}]_{N \times 1} = \begin{bmatrix} x(0) \times e^{j2\pi f_{dn} \times 0} \\ x(1) \times e^{j2\pi f_{dn} \times 1} \\ x(2) \times e^{j2\pi f_{dn} \times 2} \\ x(3) \times e^{j2\pi f_{dn} \times 3} \\ \dots \\ x(N-1) \times e^{j2\pi f_{dn} \times (N-1)} \end{bmatrix}_{N \times 1} \quad (6)$$

This is mathematical vector for fixed Doppler spread f_{dn} .

For general ambiguity function in matrix form (which means all discrete Doppler spreads are considered), it is simply the expansion of (4) as in following:

$$\begin{bmatrix}
\chi[-(N-1); f_{d0}] & \chi[-(N-1); f_{d1}] & \dots & \chi[-(N-1); f_{d(M-1)}] \\
\dots & \dots & \dots & \dots \\
\chi[-2; f_{d0}] & \chi[-2; f_{d1}] & \dots & \chi[-2; f_{d(M-1)}] \\
\chi[-1; f_{d0}] & \chi[-1; f_{d1}] & \dots & \chi[-1; f_{d(M-1)}] \\
\chi[0; f_{d0}] & \chi[0; f_{d1}] & \dots & \chi[0; f_{d(M-1)}] \\
\chi[1; f_{d0}] & \chi[1; f_{d1}] & \dots & \chi[1; f_{d(M-1)}] \\
\chi[2; f_{d0}] & \chi[2; f_{d1}] & \dots & \chi[2; f_{d(M-1)}] \\
\dots & \dots & \dots & \dots \\
\chi[N-1; f_{d0}] & \chi[N-1; f_{d1}] & \dots & \chi[N-1; f_{d(M-1)}]
\end{bmatrix}_{(2N-1) \times M} = [\mathbf{K}]_{(2N-1) \times N} [\mathbf{F}]_{N \times M} \quad (7)$$

where we expand the one fixed Doppler spread to all running indices by modifying \mathbf{f} matrix to \mathbf{F} matrix to include all the Doppler spread indices. The \mathbf{F} matrix is given by

$$[\mathbf{F}]_{N \times M} = \begin{bmatrix}
x(0) \times e^{j2\pi f_{d0} \times 0} & x(0) \times e^{j2\pi f_{d1} \times 0} & \dots & \dots & x(0) \times e^{j2\pi f_{d(N-1)} \times 0} \\
x(1) \times e^{j2\pi f_{d0} \times 1} & x(1) \times e^{j2\pi f_{d1} \times 1} & \dots & \dots & x(1) \times e^{j2\pi f_{d(N-1)} \times 1} \\
x(2) \times e^{j2\pi f_{d0} \times 2} & x(2) \times e^{j2\pi f_{d1} \times 2} & \dots & \dots & x(2) \times e^{j2\pi f_{d(N-1)} \times 2} \\
x(3) \times e^{j2\pi f_{d0} \times 3} & x(3) \times e^{j2\pi f_{d1} \times 3} & \dots & \dots & x(3) \times e^{j2\pi f_{d(N-1)} \times 3} \\
\dots & \dots & \dots & \dots & \dots \\
\dots & \dots & \dots & \dots & \dots \\
\dots & \dots & \dots & \dots & \dots \\
\dots & \dots & \dots & \dots & \dots \\
x(N-1) \times e^{j2\pi f_{d0} \times (N-1)} & x(N-1) \times e^{j2\pi f_{d1} \times (N-1)} & \dots & \dots & x(N-1) \times e^{j2\pi f_{d(N-1)} \times (N-1)}
\end{bmatrix}_{N \times M} \quad (8)$$

Therefore, the χ matrix can be calculated from the matrix operation of

$$\chi[\tau_n; f_{dn}] = [\mathbf{K}]_{(2N-1) \times N} \times [\mathbf{F}]_{N \times M} \quad (9)$$

and the ambiguity function is $|\chi[\tau_n; f_{dn}]|^2$.

It is necessary to add a constraint for $M \geq N$ to maintain the integrity of ambiguity matrix. The physical interpretation is the number of Doppler components needs to be at least as much as the length of \mathbf{x} .

The accuracy of operation is easy to check from definitions of zero-delay cut and zero-Doppler cut. By definition, the zero-delay cut is exactly the inverse Fourier transform of $x[i]^2$ and the zero-Doppler cut is the autocorrelation function of $x[i]$. It can be shown from the figure below where the zero-delay cut and zero-Doppler cut are exactly the same as the autocorrelation and IFFT results using Matlab's own corr and fft functions.

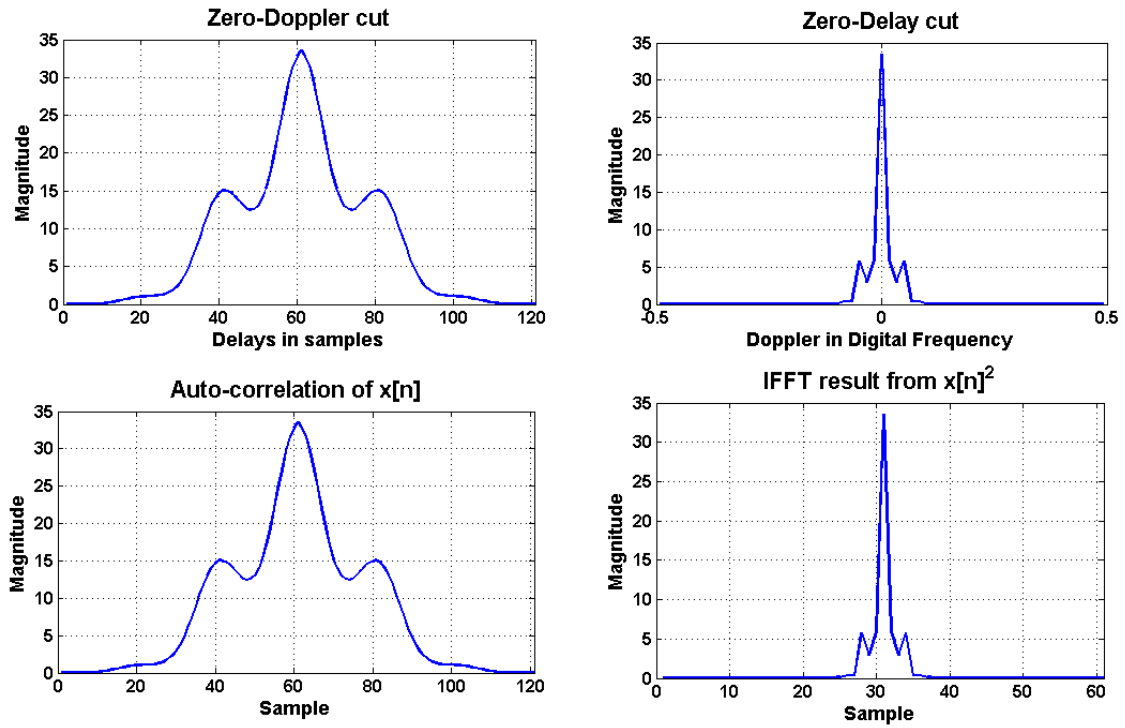


Figure 1: Comparison of ambiguity function cuts to theoretical function.

THIS PAGE INTENTIONALLY LEFT BLANK

LIST OF REFERENCES

- [1] R. A. Romero, J. Bae, and N. A. Goodman, "Theory and application of SNR and mutual information matched illumination waveforms," *IEEE Trans. Aerospace and Electronic System.*, vol. 47, no. 2, pp. 912–927, Apr. 2011.
- [2] R. A. Romero, and N. A. Goodman, "Improved waveform design for target recognition with multiple transmissions," *IEEE Conference on Waveform Diversity and Design.*, Kissimmee, FL, pp. 26–30, Feb. 2009.
- [3] S. M. Kay, *Fundamentals of Statistical Signal Processing volume II*. Upper Saddle River, NJ: Prentice Hall PTR, 1993.
- [4] N. Levanon and E. Mozeson, *Radar Signals*. Hoboken, NJ: John Wiley and Sons, 2004.
- [5] B. R. Mahafza, *Radar Signal Analysis and Processing using MATLAB*. Boca Raton, FL: CRC Press, 2009.
- [6] M. R. Bell, "Information theory and radar waveform design," *IEEE Trans. Information Theory.*, vol. 39, no. 5, pp. 1578–1597, Sep. 1993.
- [7] J. Y. Nieh, and R. A. Romero, "Ambiguity function and detection probability considerations for matched waveform design," *IEEE Conference on Acoustics, Speech and Signal Processing.*, Vancouver, BC, pp. 4280–4284, May 2013.
- [8] R. A. Romero, and N. A. Goodman, "Information-theoretic matched waveform in signal dependent interference," *IEEE Radar Conference.*, Rome, Italy, pp. 1–6, May 2008.
- [9] Y. Wei, H. Meng, and X. Wang, "Adaptive single-tone waveform design for target recognition in cognitive radar," *IET International Radar Conference.*, pp. 1–4, Apr. 2009.
- [10] S. Haykin, "Cognitive radar: a way of the future," *IEEE Signal Processing Mag.*, vol. 23, no. 1, pp. 30–40, Jan. 2006.
- [11] S. Haykin, *Adaptive Filter Theory*. Upper Saddle River, NJ: Prentice Hall, 1996.
- [12] N. Levanon, *Radar Principles*. NJ: John Wiley and Sons, 1988.
- [13] B. R. Mahafza, *Introduction to Radar Analysis*. Boca Raton, FL: CRC Press, 1998.
- [14] S. M. Kay, *Fundamentals of Statistical Signal Processing volume I*. Upper Saddle River, NJ: Prentice Hall PTR, 1993.

- [15] D. Tahmoush, and J. Silvius, "Time-integrated range-Doppler maps for visualizing and classifying radar data," *IEEE Radar Conference.*, Kansas City, MO, pp. 372–374, May 2011.
- [16] M. Soltanalian, and P. Stoica, "Computational design of sequences with good correlation properties," *IEEE Trans. Signal Process.*, vol. 60, no. 5, pp. 2180–2193, May 2012.
- [17] J. R. Guerri, "Cognitive radar: A knowledge-aided fully adaptive approach," *IEEE Radar Conference.*, Washington, DC, pp. 1365–1370, May 2010.
- [18] R. A. Romero, "Detection performance of matched transmit waveform for moving extended targets," *Asilomar Conference on Signals, Systems, and Computers.*, Pacific Grove, CA, pp. 1956–1960, Nov. 2013.
- [19] C. E. Baum, "Signature-based target identification and pattern recognition," *IEEE Antennas and Propagation Mag.*, vol. 36, issue. 3, pp. 44– 51, Jun. 1994.
- [20] R. Schumacher, and J. Schiller, "Non-cooperative target identification of battlefield targets - classification results based on SAR images," *IEEE Radar Conference.*, pp. 167–172, May 2005.
- [21] W. C. Chen, and N. V. Z. Shuley, "Robust target identification in white Gaussian noise using canonical correlation analysis," *IEEE Trans. Antennas and Propagation.*, vol. 60, issue. 7, pp. 3533–3537, Jul. 2012.
- [22] W. C. Chen, and N. V. Z. Shuley, "Robust target identification using a modified generalized likelihood ratio test," *IEEE Trans. Antennas and Propagation.*, vol. 62, issue. 1, pp. 264–273, Jan. 2014.
- [23] W. Wang, T. Adalt, and D. Emge, "Target detection and identification using canonical correlation analysis and subspace partitioning," *IEEE Conference on Acoustics, Speech and Signal Processing.*, Las Vegas, NV, pp. 2117–2120, Apr. 2008.
- [24] B. Kahler, and E. Blasch, "Predicted radar/optical feature fusion gains for target identification," *IEEE Aerospace and Electronics Conference (NAECON).*, pp.405-412, Jul. 2010.
- [25] T. B. Butler, and N. A. Goodman, "Multistatic target classification with adaptive waveforms," *IEEE Radar Conference.*, Rome, Italy, pp.1-6, May 2008.
- [26] N. A. Goodman, P. R. Venkata, and M. A. Neifeld, "Adaptive waveform design and sequential hypothesis testing for target recognition with active sensors," *IEEE Journal of Selected Topics in Signal Processing.*, vol.1, issue.1, pp 105–113, Jun. 2007.

- [27] A. H. Nuttall, "Some windows with very good sidelobe behavior," *IEEE. Trans. Acoustics, Speed, and Signal Processing.*, vol. 29, no.1, pp 84–91, Feb. 1981.
- [28] B. Getz, and N. Levanon, "Weight effects on the periodic ambiguity function," *IEEE Trans. Aerospace and Electronic Systems.*, vol. 31, issue.1, 182–193, Jan. 1995.
- [29] J. J. Benedetto, and J. J. Donatelli, "Ambiguity function and frame-theoretic properties of periodic zero-autocorrelation waveforms," *IEEE Journal of Selected Topics in Signal Processing.*, vol. 1, issue. 1, pp. 6–20, Jun. 2007.
- [30] L. Auslander, and R. Tolimieri, "Characterizing the radar ambiguity functions," *IEEE Trans. Information Theory.*, vol. 30, issue. 6, pp. 832–836, Nov. 1984.
- [31] A. Freedman, and N. Levanon, "Properties of the periodic ambiguity function," *IEEE. Trans. Aerospace and Electronic Systems.*, vol. 30, issue. 3, pp. 938–941, Jul. 1994.
- [32] C. W. Therrian, *Discrete Random Signals and Statistical Signal Processing*. Monterey, CA: Prentice-Hall 1987.
- [33] R. V. Heiden, F. C. A. Groen and L. J. Ewijk, "Aircraft recognition with radar range profiles using a synthetic database," In *RTO SET Symposium on High Resolution Radar Techniques*, 1999.

THIS PAGE INTENTIONALLY LEFT BLANK

INITIAL DISTRIBUTION LIST

1. Defense Technical Information Center
Ft. Belvoir, Virginia
2. Dudley Knox Library
Naval Postgraduate School
Monterey, California